

# Probing unitary Fermi gases locally with Bragg spectroscopy

by

**Marcus Lingham**

*A thesis submitted for the degree of  
Doctor of Philosophy*



*Centre for Quantum and Optical Science  
Faculty of Science, Engineering and Technology  
Swinburne University of Technology  
Melbourne, Australia*

April 14, 2016



# Abstract

This thesis presents measurements of local properties of unitary Fermi gases above and below the critical temperature of the superfluid phase transition using Bragg spectroscopy. Dilute gases of  ${}^6\text{Li}$  atoms are cooled to temperatures on the order of 10s of nanoKelvins using standard laser cooling, trapping, and evaporative cooling techniques. The gas is confined within an optical dipole trap in a strong magnetic field and the atoms are prepared in a 50-50 mixture of their two lowest hyperfine states. The trapping potential provided by the optical dipole trap is highly harmonic so the atomic density varies spatially within the trap. Control of the interactions between atoms in the two states is enabled by a strong magnetic field via the  $s$ -wave Feshbach resonance. When the  $s$ -wave scattering length becomes infinite, the gas is at unitarity and its properties are said to become universal. These gases are probed using Bragg spectroscopy at high momentum where the density-density response is sensitive to single particle excitations. This allows one to obtain information about the initial state of the gas by measuring how the density responds to a perturbation.

The first measurement described in this work involves Bragg scattering from the atom cloud when energy and momentum are conserved for the scattering of a pair of atoms [1]. At unitarity, the local relative temperature, which is the ratio of the absolute temperature of the gas over the Fermi temperature, sets the point at which pair-condensation occurs. Therefore, the Bragg response can be quantified locally along one axis of the trap. The local density approximation is then applied to calculate the local homogeneous density-density response. This measurement is performed for several different clouds of varying absolute temperatures to find that the homogeneous response consistently shows a sharp increase at local temperatures below  $\sim 0.18$  of the Fermi temperature. This corresponds to an increase in the number of pairs in the gas with

---

zero centre-of-mass momentum which provides a signature of pair-condensation.

The second main result in this thesis is a measurement of the trap-averaged contact versus temperature at unitarity. Tan's universal contact parameter describes the short-range limit of the two-body correlation function, yet it also appears in the thermodynamic properties of the bulk system through the set of Tan's universal relations. The density-density response is measured against Bragg frequency to produce a Bragg spectrum, from which one can obtain the dynamic structure factor, a parameter that details a systems response to a probe of momentum  $\hbar\mathbf{k}$  and energy  $\hbar\omega$ . Integrating the dynamic structure factor over the Bragg frequency yields the static structure factor, which gives the Fourier transform of the two-body correlation function. The structure factor Tan relation is then applied to find the contact parameter and hence its temperature dependence. This technique yields the contact to a high degree of accuracy with statistical error on the order of 3%. These measurements can be used to benchmark theoretical calculations of this parameter which vary by around 10%.

# Acknowledgements

Well it has been a pretty long stint at Swinburne university and I have met a lot of people on the way. As a result there are a few that I would like to thank for helping me get this far.

First off I would like to thank my principle supervisor, Chris Vale, for his unwavering support and excellent guidance throughout my PhD. He always showed a great amount of enthusiasm for the work we were carrying out and provided lots of assistance when I needed help. He always demonstrated a high level of clarity and patience, and was also very compassionate for which I am grateful. I would also like to thank my other supervisor, Peter Hannaford. Peter has such a breadth of experience and I have enjoyed listening to historical accounts of new discoveries in physics as they happened. He also provided very good feedback for anything I wrote.

I am grateful to Paul Dyke who provided me with a great example what it means to be a researcher when I first arrived at the lithium lab in my honours year in 2010. A few years down the track when he came back from America, he helped me out a great deal by improving some aspects of the experiment, as well as assisting with data collection. When I first started my PhD, I learned a lot about running and maintaining the experiment down to the small intricacies, and for that I owe credit to Sascha Hoinka. Sascha proceeded to put me in the deep end by making me run the laboratory and collect the data for him, which was vital experience that set me up for the rest of my PhD. Both Sascha and Paul also showed a tremendous amount of patience when listening to my jokes. Further thanks goes to Kristian Fenech and Tyson Pepler for being a huge help with data collection. Kristian also took care of the camera software and LabView upgrades which put us in good stead while Tyson provided me with great wisdom on how to dull the feeling of spiciness after eating a chilli.

---

Whenever I needed help with designing and manufacturing a new part for the experiment, our technician Mark Kivinen was always keen to help us out so I am appreciative of that. Also thanks goes to Tatiana Tchernova for putting up with the fact that I am an absolute dodo when it comes to administrative tasks and for always being extremely reliable when I needed her assistance.

To the rest of the folks at CQOS (formally CAOUS), I would like to thank you all for being friendly, supportive, and up for discussion, whether it's physics related or not, as well as allowing me to borrow lab equipment when needed. A special shout out goes to Will Brown for being Bill.

Outside of the lab, I would like to thank all of the boys down at the Swinburne Razorbacks football club. I have not missed a season of footy since I started at the age of 8 so I am lucky to have such a welcoming club nearby that I can go to have a kick and a laugh while keeping fit and grounded. To my mates outside of work; Todd, Gillies, Muzzy, Rohan, Dan, Jules, Yvette, Kendog, and others, I thank them for all of their support that they provided me in their own ways.

To finish off, I would like to thank everyone from my extended family, including aunts, uncles and cousins, who I am always happy to see, especially to my oma, Hildegard, and my grandma, Evelyn. A special thanks goes to my partner Emilie who provided me with much love, comfort, and belief in myself when I needed it. She was always on the lookout for things she could do to make my life easier and I am indebted to her for that. Thanks also goes to Emilie's family, and my two younger brothers, Sam and Gareth, as well as Rosie for all of their support. Lastly, sometimes it is nice to get out of the big smoke and head back to the sticks, and I am extremely lucky to have such a place I can go to with the farm at Rupanyup South. I would like to thank my parents, Rod and Christa, for always welcoming me back home to the farm and supporting me throughout my journey. They have backed me all the way through and I would not be where I am without them.

# Declaration

I, Marcus Lingham, declare that this thesis entitled:

*“Probing unitary Fermi gases locally with Bragg spectroscopy”*

contains no material which has been accepted for the award to the candidate of any other degree or diploma, except where due reference is made in the text of the examinable outcome;

to the best of my knowledge, contains no material previously published or written by another person except where due reference is made in the text of the examinable outcome; and

where work is based on joint research or publications, discloses the relative contributions of the respective workers or authors.

Marcus Lingham

Centre for Quantum and Optical Science (CQOS)

Faculty of Science, Engineering and Technology

Swinburne University of Technology

Melbourne, Australia

April 14, 2016

# Contents

<b>1</b>	<b>Introduction</b>	<b>12</b>
1.1	Literature Review . . . . .	12
1.2	Aims of this thesis . . . . .	21
1.3	Thesis outline . . . . .	22
<b>2</b>	<b>Overview of strongly interacting Fermi gases</b>	<b>24</b>
2.1	Introduction . . . . .	24
2.2	Ideal Fermi gases . . . . .	25
2.3	Scattering theory . . . . .	26
2.4	Feshbach resonances . . . . .	30
2.5	To the many-body picture . . . . .	33
2.5.1	Weakly interacting BEC limit . . . . .	34
2.5.2	Weakly interacting BCS limit . . . . .	35
2.5.3	Unitarity and the strongly interacting regime . . . . .	37
2.6	Universality and Tan's contact parameter . . . . .	39
2.7	Excitations in the BCS-BEC crossover . . . . .	41
2.8	Summary . . . . .	43

---

<b>3</b>	<b>Experimental setup and image calibration</b>	<b>44</b>
3.1	Introduction . . . . .	44
3.2	Initial cooling stages . . . . .	45
3.3	The final trap . . . . .	51
3.4	Absorption imaging . . . . .	53
3.5	Determining the homogeneous density . . . . .	57
3.6	Thermometry . . . . .	61
3.7	Atom number calibration . . . . .	63
3.8	Summary . . . . .	72
<b>4</b>	<b>Bragg spectroscopy and linear response</b>	<b>73</b>
4.1	Introduction . . . . .	73
4.2	Bragg spectroscopy . . . . .	73
4.2.1	Experimental setup . . . . .	74
4.2.2	Obtaining a Bragg spectrum . . . . .	79
4.2.3	Bragg scattering pairs . . . . .	81
4.3	Linear Response Theory . . . . .	84
4.3.1	Dynamical susceptibility and structure factors . . . . .	87
4.3.2	$f$ -sum rule . . . . .	91
4.4	Summary . . . . .	92
<b>5</b>	<b>Local measurement of pair-condensation</b>	<b>94</b>
5.1	Introduction . . . . .	94
5.2	A closer inspection of Bragg scattered images . . . . .	95
5.3	Extracting local information . . . . .	99
5.4	Measuring the homogeneous density-density response . . . . .	100
5.5	Response at the pairing resonance . . . . .	101
5.6	Homogeneous response and its temperature dependence . . . . .	104
5.7	Summary . . . . .	107

---

<b>6</b>	<b>Temperature dependence of the trap-averaged contact</b>	<b>109</b>
6.1	Introduction . . . . .	109
6.2	Method . . . . .	110
6.3	Measured structure factors . . . . .	114
6.4	Trap-averaged contact . . . . .	117
6.5	Homogeneous contact . . . . .	119
6.6	Summary . . . . .	122
<b>7</b>	<b>Conclusion and Outlook</b>	<b>124</b>
7.1	Conclusion . . . . .	124
7.2	Outlook . . . . .	125

# List of Figures

2.1	Definition of the $s$ -wave scattering length . . . . .	29
2.2	An illustration of two scattering channels . . . . .	31
2.3	${}^6\text{Li}$ scattering lengths . . . . .	32
2.4	BCS-BEC crossover phase diagram . . . . .	34
2.5	Dispersion relations in the BCS-BEC crossover . . . . .	42
3.1	Oven and Zeeman slower . . . . .	45
3.2	Magneto-Optical trap illustration . . . . .	47
3.3	Energy level diagram for the MOT cooling transition in ${}^6\text{Li}$ . . . . .	48
3.4	Optical dipole trap/evaporation laser illustration . . . . .	49
3.5	Setup for the secondary optical dipole trap from the top . . . . .	52
3.6	Setup for the secondary optical dipole trap from the side . . . . .	52
3.7	Trap frequency measurement in $x$ . . . . .	53
3.8	Trap frequency measurement in $y$ . . . . .	54
3.9	Trap frequency measurement in $z$ . . . . .	54
3.10	Extracting the homogeneous density from the 1D column density . . . . .	57
3.11	Inverse Abel transform on an optical density image . . . . .	60
3.12	Pressure equation of state from BDMC simulation . . . . .	63
3.13	Our data fitted to the pressure equation of state . . . . .	64

---

3.14	Atom number versus time of flight . . . . .	66
3.15	Peak optical density versus time of flight . . . . .	67
3.16	Scaled atom number versus time of flight . . . . .	68
3.17	Scaled atom number versus peak optical density . . . . .	69
3.18	Imaging intensity versus scaled atom number . . . . .	70
3.19	1D column density and fit . . . . .	71
4.1	The effect of Bragg scattering on an atom cloud . . . . .	76
4.2	Energy level diagram showing the transitions used for Bragg spectroscopy	77
4.3	An illustration of the Bragg scattering lattice . . . . .	78
4.4	Optical setup for a Bragg beam . . . . .	79
4.5	Bragg spectra of cold clouds below $T_C$ . . . . .	82
5.1	Absorption images of atoms that have been Bragg scattered . . . . .	96
5.2	Sliced image . . . . .	97
5.3	Raw sliced spectra . . . . .	98
5.4	Homogeneous spectra . . . . .	100
5.5	Raw response and one-dimensional column density versus $z$ . . . . .	102
5.6	Homogeneous response versus $z$ . . . . .	103
5.7	Homogeneous response versus local temperature for individual clouds .	105
5.8	Homogeneous response versus local temperature and local wavevector .	106
5.9	Two-dimensional plot of homogeneous response versus local temperature	107
6.1	Response versus intensity product for linearity check . . . . .	112
6.2	Dynamic structure factors . . . . .	116
6.3	Trap-averaged contact versus bulk temperature . . . . .	119
6.4	Preliminary data for homogeneous contact versus local temperature . .	120

# List of Tables

6.1	Bragg frequencies taken in a experiment and their intensity products	. 113
-----	--	-------

# Chapter 1

## Introduction

This chapter introduces the main contentions of this thesis, which are set up by a review of the previous work in the field of strongly interacting ultracold Fermi gases. Emphasis in this literature review is placed upon prior work in this field from all over the world that have shed insights into local measurements, pair-condensation and pair correlations in these systems. After the literature review there is a small section outlining the aims of this thesis followed by a brief outline of the remaining chapters.

### 1.1 Literature Review

Since the creation of the first atomic Bose-Einstein condensate (BEC) in 1995 [2, 3], the field of ultracold atoms has generated enormous interest. This achievement used optical and magnetic fields to trap and cool a cloud of bosonic alkali atoms down to nanoKelvin temperatures. The thermal de Broglie wavelength becomes larger as atoms lose energy and once the temperature of the atom cloud drops below the critical temperature,  $T_C$ , a rapidly increasing portion of the atoms occupy the lowest energy quantum level. At this point the de Broglie wavelength is larger than the interparticle separation, and long range coherence emerges in the system. With enough atoms in the ground state, this new state of matter was observed macroscopically in a harmonically trapped gas, characterised by a sudden spike appearing in the number of atoms at the centre of the momentum distribution ( $p = 0$ ) [2, 3].

From here, attention also turned to creating ultracold systems using a gas of fermionic atoms. Fermions have a 1/2-integer intrinsic angular momentum, unlike bosons which are integer spin particles. The fermionic wavefunction is antisymmetric which gives rise to the Pauli exclusion principle. This means that in contrast to bosons, no two indistinguishable fermions can occupy the same quantum state. All atoms are made up of fermionic constituents- protons, neutrons and electrons, making fermions the building blocks for all visible matter.

At high temperature, a thermal gas of fermions behaves similarly to a thermal gas of bosons, both following a Maxwell-Boltzmann distribution. It is only when a gas is cooled down to ultracold temperatures that quantum statistics start to play a major role. Due to the Pauli exclusion principle, there cannot be macroscopic occupation of the ground state for fermions, as seen with bosons. Instead, at zero temperature, fermions will sink down to the lowest unoccupied state. This leads to a stacking of occupied states up to the highest energy known as the Fermi energy,  $E_F$ , which is therefore dependent on the number of atoms in the system. The distribution of fermions among the available quantum states is described by Fermi-Dirac statistics. Fermi degeneracy was first achieved in 1999 [4] and the observation of Fermi pressure came in 2001 [5].

Interactions are negligible in a single-component ultracold Fermi gas system as all non  $s$ -wave collisions are suppressed at ultracold temperatures. This is because for  $l > 0$ , the scattering cross-section goes to a negligible value at low energy due to the centrifugal barrier in the scattering potential.

However, the addition of a second species into the system gives rise to some more interesting physics. This is because non-identical particles can interact with each other through  $s$ -wave collisions. We have the ability to tune the interactions between atoms of opposite spins, simply by varying the strength of an external magnetic field using a Feshbach resonance. When a bound molecular state couples to two free colliding atoms, a Feshbach resonance occurs [6]. These were first observed in Bose gases [7, 8]. However, creating a stable resonant Bose gas was not possible due the high number of inelastic collisions present in the strongly interacting system [9]. In Fermi gases though, inelastic collisions are suppressed by the Pauli exclusion [10–12].

In Fermi gases, Feshbach resonances lead to several interesting phenomena. Sweeping the strength of an external magnetic field through a Feshbach resonance significantly

alters the  $s$ -wave interactions and hence the pairing mechanisms between fermions of different spin states, to the point where the system experiences a crossover.

Below the Feshbach resonance, the energy of the molecular state is lower than the incident energy of two colliding atoms, leading to a positive  $s$ -wave scattering length. Two fermions can be bound energetically to form a dimer molecule, which now behaves as a boson and with many of these present the system can form a BEC, hence this is called the BEC regime.

Far above the Feshbach resonance, we have the Bardeen-Cooper-Schrieffer (BCS) regime. The  $s$ -wave scattering length is small and negative due to the energy of the molecular bound state being greater than the incident energy. This regime can see the formation of Cooper pairs [13]. Unlike bound molecules, these are not spatially correlated, but are instead correlated in momentum space. Cooper pairs exist on the outer edges of a Fermi sea, where lower energy states are inaccessible as a consequence of Pauli blocking. Therefore the pairing here is a many-body effect.

When an external magnetic field is swept from one side of a Feshbach resonance to the other, there is a smooth crossover that links these two different regimes mentioned above [14]. This is the BCS-BEC crossover. In the middle of the crossover, another regime exists which is challenging to understand from a theoretical point of view due to the lack of small parameters to describe the interactions. At this point, the  $s$ -wave scattering length has diverged to a length scale that is much larger than the interparticle spacing, and eventually becomes irrelevant to the scattering cross-section of the particles, making the physics universal [15]. The scattering cross-section now depends only on the thermal de Broglie wavelength. This is known as the unitarity regime and the main contention of this thesis will be to study Fermi gases at this point in the crossover. The pairs in this regime are neither strictly molecules or Cooper pairs, but exhibit a mixture of the properties from both regimes. Here, the pair size is on the same order as the interparticle spacing and despite the strong interactions the system is quite stable due to suppressed inelastic collisions.

In essence, the benefit of using a Feshbach resonance is that we can tune the interactions in a two-component Fermi gas with a strong, external magnetic field and gain access to several different varieties of physics. A molecular BEC was first observed in

2003 [16, 17] but it was through the use of a Feshbach resonance that the first fermionic condensate was formed in 2004 [18].

Since then, several laboratories around the world have been able to produce strongly interacting Fermi condensates and have used a variety of methods to probe their properties. Superfluidity was shown to exist along the crossover, as well as either side, through the observation of vortices [19]. When a superfluid is rotated, vortices appear throughout the system as opposed to a rigid body rotation that is seen in normal fluids.

Significant attention went into observing signs of pairing as the temperature of the Fermi gas decreases. A signature for pairing was shown in a strongly interacting Fermi gas using radio-frequency (RF) spectroscopy [20]. This method involved exciting one of the initial states into an unoccupied final state using an RF pulse. By varying the frequency of the RF pulse, a spectrum was obtained where the loss of atoms from the initial state was plotted against RF frequency. At high temperatures ( $T \approx 6T_F$ , where  $T_F$  is the Fermi temperature), a single narrow peak was observed that represented free atoms. However, at lower temperatures, a secondary peak appeared that was offset from the free atom peak. This peak represented the dissociation of bound pairs in the system and, as expected, it became less prominent as the Feshbach field was swept from the BEC side to the BCS side. However, this measurement did not take into account the inhomogeneity of the trapped cloud, nor did it take into account the final state interactions after the RF pulse. The line broadening effect due to averaging over an inhomogeneous density was reduced in later experiments by taking measurements on a spin imbalanced mixture [21], and further improved by finding the true atomic density using the inverse Abel transform [22]. More accurate measurements to determine the size of the pairs was later achieved by taking care of the final state interactions by dissociating pairs from a strongly interacting combination to a weakly interacting mixture [23].

Another method used to probe pair correlations is two-photon Bragg spectroscopy. This entails firing two off-resonant phase locked laser beams at the gas which intersect at an angle  $2\theta$ . The frequency of one beam is varied with respect to the other, and the frequency difference between the two beams is  $\omega$ . Absorption of a photon from one beam and then stimulated emission into the other beam causes momentum to be transferred to the atoms in the direction of the “moving standing wave” produced by

the two Bragg laser beams. Measuring the response of the cloud as a function of  $\omega$  yields a spectrum that can provide the dynamic structure factor  $S(k, \omega)$ , which describes the possibility to transfer momentum,  $\hbar k = 4\pi \sin(\theta)/\lambda$ , and energy,  $\hbar\omega$ .

Dynamic structure factor measurements first came into prominence in the context of inelastic neutron scattering studies on superfluid  $^4\text{He}$  where information about the system is measured by bombarding it with a beam of neutrons. The angle at which the neutrons deflect off the sample can be used to work out  $\hbar k$  while the Fourier transform of the number of deflected particles per unit time gives  $S(k, \omega)$ , as well as  $\hbar\omega$  if the initial energy of the neutrons was known. In the 1950's, it was realised that pair correlations in the system could be determined from the differential cross section of the  $^4\text{He}$  [24] and then in the 1960's, it was first proposed that the condensate fraction of the  $^4\text{He}$  could be measured from the dynamic structure factor [25] at high momentum (i.e.  $1/k$  is less than the interparticle spacing). Over the course of several decades after this, until the 1990's, there were several experiments that set out to measure the dynamic structure factor, including [26–28], and others given in reference [29]. At the same time significant theoretical studies were being carried out to calculate the condensate fraction from the measured  $S(k, \omega)$ , shown in [30] and others given in reference [29], but the most accurate value of the condensate fraction using inelastic neutron scattering came to be  $(10 \pm 1.25)\%$  for a temperature of  $0.35T_C$  [29, 31]. Bragg spectroscopy has some similarities to these neutron scattering experiments and it was originally used to probe the excitations of an atomic BEC [32].

It was suggested that the dynamic structure factor in a Fermi gas could show signatures of pairing along the BCS-BEC crossover [33], which was then verified experimentally at Swinburne using Bragg spectroscopy [34]. For a given two-photon Bragg scattering process, the momentum transferred to an atom is  $\hbar k$ , and from this momentum “kick” an atom of mass  $m$  that was initially stationary experiences a change in kinetic energy of  $\hbar^2 k^2/2m$ . If the energy difference between the two photons,  $\hbar\omega$ , is equal to the change in kinetic energy, the atom will then experience the momentum and energy transfer. This gives rise to the Bragg resonance condition,  $\omega_r = \hbar k^2/2m$ , where the atoms will respond resonantly if  $\omega = \omega_r$ . The mass term in the denominator of the Bragg condition becomes important because it is possible to Bragg scatter a pair of atoms in a single Bragg process, therefore stationary pairs will scatter resonantly when

$\omega = \omega_r/2$ . Therefore, a Bragg spectrum across these two resonances gives considerable insight into the nature of the pairing in the system, both as a function of the  $s$ -wave scattering length [34] and the temperature [35].

While theories of the weakly interacting regimes are quite well established, strongly interacting gases have proven to be a challenging problem. For weakly interacting gases, the  $s$ -wave scattering length which describes the interactions is a small parameter, so the superfluid system can be theoretically described using simple perturbation theory. This luxury does not exist in the strongly interacting case making it difficult to develop quantitatively accurate theoretical descriptions of universal thermodynamic behaviour.

In the early 2000s, it was hypothesised that Fermi systems at unitarity exhibit universal behaviour [36, 37]. In 2008<sup>1</sup>, Shina Tan provided a new insight into universality by deriving a set of exact relations that included a new parameter called the contact  $C$  [39–41]. The contact can be derived from microscopic quantities, for example, the amplitude of the high-momentum tail in the momentum distribution, but it contains details about the bulk thermodynamics of the entire system. After the derivation of the first few Tan relations, these have been rederived and extended using different techniques [42–55] showing that the contact can be calculated from many different system parameters.

Because of this breakthrough, focus of both theorists and experimentalists moved towards finding the value of this contact parameter at unitarity. Theoretically, the contact is quite well known for weakly interacting systems but becomes hard to calculate in the strongly interacting regime. Despite this, several different methods have been used by theorists to calculate the contact which involved the calculation of the various system parameters that can be used in Tan relations. These include the use of the many-body  $T$ -Matrix approximation in strong coupling theories including: the Nozières Schmitt-Rink [56] (NSR) model [57],  $G_0G_0$  [58], and GG [59, 60]. Other theoretical calculations of the contact used quantum Monte Carlo simulations [33, 54, 61–63]. Also, experimental data that had previously measured the number of closed-channel molecules in a strongly interacting Fermi gas [64] allowed a calculation of the contact a few years later [65]. The contact has also been calculated in [66] from experimental

---

<sup>1</sup>It is worth noting that these papers were first posted on *arxiv* in 2005 [38] before being published three years later.

data measuring the frequency of collective oscillations [67].

Experimental studies were also being carried out at this time to directly investigate the contact. At JILA, a measurement of the momentum distribution,  $n(k)$ , was achieved by sweeping across the Feshbach resonance to a very weakly interacting gas and then releasing the cloud to be imaged after a certain time of flight [68]. The contact is then the value where  $k^4 n(k)$  asymptotes at high- $k$ . In the same publication, RF spectroscopy was also used to find the contact. The high-frequency tail of RF spectra depends on  $C/\nu^{-3/2}$ , where  $\nu$  is the RF frequency, so similar means to the measurement of the momentum distribution were used to extract the value of the contact  $C$ . A third measurement of the contact in this publication used a method that combined both of the previous methods called photoemission spectroscopy (first described in [69]). After the gas experiences an RF pulse, an image of the newly occupied state is taken after a time of flight to resolve the momentum distribution of the spin-flipped atoms. Integrating over the energy axis gives a measurement of  $n(k)$  that can be treated the same way as the measurement of the momentum distribution described previously to find  $C$ . It should be noted that all of these measurements of the contact were performed on trapped clouds.

Another measurement of the contact was performed at Swinburne using Bragg spectroscopy [35]. By integrating the dynamic structure factor,  $S(k, \omega)$ , the static structure factor,  $S(k)$ , can be calculated, which is the Fourier transform of the two-body correlation function. The full dynamic structure factor has been calculated previously for strongly interacting Fermi gases using quantum Monte Carlo simulations [33, 70], as has the static structure factor [63]. Using the static structure factor, the trapped contact,  $\mathcal{I}$ , can be calculated directly [48, 71]. The most precise measurements of the trapped contact with a 3% error bar have been achieved using this method [63]. It has also been shown that the contact can be derived directly from the dynamic structure factor which displays a universal high-frequency tail that depends on  $C/\omega^{-7/2}$  [46, 50], however there are yet to be any experimental results using this Tan relation.

As well as the trap-averaged contact, some experiments have looked into finding the homogeneous contact. An equation of state measurement for varying interactions at ENS found how the total energy of the system depends on the inverse scattering length, enabling the extraction of the contact [72]. At JILA again, a new kind of measurement

was performed which looked at the temperature dependence of the homogeneous contact [73]. This also utilised RF spectroscopy but this time the cloud was prepared by optically pumping the atoms in the wings of the cloud to a dark state before taking the measurement. This ensured that only the atoms from the central part of the cloud, which was nearly homogeneous, contributed to the result of the measurement.

As experimentalists are now moving their measurements on dynamical properties of strongly interacting Fermi gases into the realm of high precision and homogeneity, it has become increasingly vital that the static properties, such as the equation of state, are also known to a high degree of accuracy. This provides a scale to measure against and enable theoretical calculations to be reliably tested.

Since the creation of unitary Fermi gases, measuring the temperature has proven to be a challenge because the equation of state is difficult to obtain as theoretical methods used for weak interactions do not hold with strong interactions. In BECs, the temperature can be obtained by fitting the non-condensed wings of the bimodal distribution to an ideal gas profile. For an ideal or very weakly interacting Fermi gas, the density profile can be fitted to a polylogarithm function. Indeed, earlier experiments did measure the temperature by sweeping the magnetic field away from the Feshbach resonance and using either of these two theories [18, 20], however this method is susceptible to systematics. But, in order to demonstrate universal behaviour, reliable thermometry for strongly interacting clouds was required.

It had been established that a virial theorem can be used to describe these systems [74]. Several experimental groups set out to find an equation of state for unitary Fermi gases. An earlier measurement at JILA involved a comparison between strongly and weakly interacting  $^{40}\text{K}$  in order to measure the potential energy versus temperature of the gas [75]. Not long after, at Duke, this method was extended to  $^6\text{Li}$  where entropy was conserved with a sweep of the magnetic field [76]. Therefore the entropy could be directly measured in the weakly interacting gas. By knowing the entropy and the potential energy of the gas, the temperature can be calculated. The results from both of these measurements agreed very well with each other despite using different atoms, confirming universality [15].

These results are only valid for a trapped gas, which is not ideal as the varying density tends to wash out any sharp features or discontinuities associated with a superfluid

phase transition. Theorists also largely used homogeneous densities for their equation of state calculations. A theoretical procedure used for calculating state parameters is the virial expansion [77], which works very well for high temperature clouds and was soon aided with addition of a third virial coefficient that could be used on clouds below the Fermi temperature,  $T_F$ , [78], and later again with a fourth virial coefficient [79].

While the conventional methods that are used to optically image these systems yield a two-dimensional projection of a three-dimensional cloud, the inverse Abel transform can be used for clouds with cylindrical symmetry (or elliptical symmetry for clouds imaged *in situ* [80]) to extract the true atomic density [81]. With the application of a local density approximation, small areas of an inverse Abel transformed image of the trapped cloud can be treated as homogeneous. Also, using the Gibbs-Duhem relation,  $dP = nd\mu$ , where  $\mu$  is the chemical potential, it was shown that a doubly-integrated density profile,  $\tilde{n}(z) = \int n(x, z)dx$ , is proportional to the pressure along the axis of the trap,  $P(0, 0, z)$  [82]. In the same publication, the homogeneous density was found to be proportional to the derivative of  $\tilde{n}(z)$ . These results were profound in terms of relating experimental data to theory. At ENS, measurements were made on  ${}^6\text{Li}$  to study the behaviour of a thermodynamic function using the aforementioned realisations. Bosonic  ${}^7\text{Li}$  was in thermal contact with the  ${}^6\text{Li}$  and used as a thermometer [83]. This method was extended to finding the equation of state for off-resonant gases [72]. Recently, a model independent method was used at MIT to construct the equation of state [80]. This involved extracting the local compressibility, which is the relative change of gas density versus chemical potential, from various density profiles and relating it back to thermodynamic quantities like temperature, specific heat, and chemical potential. The data from this provided a new insight into the superfluid phase transition. Around the same time, results from a new bold diagrammatic Monte Carlo simulation from ENS were developed and were shown to fit well with the MIT measurements for a gas in the normal phase [84]. These could all be used as a fitting function that extends beyond the 3rd order virial expansion.

In a three-dimensional Fermi gas, pair-condensation and superfluidity occur simultaneously. There have been several observations of pair-condensation in the past, the earliest as mentioned already, was confirmed at JILA [18] where the gas was prepared at certain magnetic fields around the Feshbach resonance. The atoms were then released

and an immediate rapid ramp of the Feshbach field was applied to drive the gas into the weakly interacting BEC regime. Because the pairs preserved their initial centre-of-mass momentum during the sweep, the signature for pair-condensation was observed in the momentum distribution of the expanded cloud and the molecular condensate fraction was calculated based on the bimodal distribution. This method to measure pair-condensation in a three-dimensional Fermi gas was also used in other laboratories [85–87] as well as allowing a similar observation in a quasi-2D Fermi gas [88]. While this method provided a clear signature for pair-condensation, it has several weaknesses. Despite the efforts made to keep the magnetic field ramp fast so no pair collisions can occur which would alter the momentum distribution, the binding energy still increases dramatically as the magnetic field drops below the Feshbach resonance, so there is a production of molecules during the sweep that can disrupt the measurement of pair-condensation [89]. Another hint of condensation came from observing expanded clouds at the Feshbach resonance [90]. After azimuthal averaging, the one-dimensional profile was fitted to a Thomas-Fermi profile, and several minor “kinks” could be observed in the fit residuals for colder clouds, indicating the possible existence of two separate sets of dynamics within the gas.

All of these observations of pair-condensation used expanded clouds which means that any local information like phase discontinuities is necessarily lost. This means that while there has been significant progress in terms of understanding these systems, there are several areas where quantitative knowledge is missing.

## 1.2 Aims of this thesis

The literature review in the previous section describes several key developments that are relevant to what this thesis presents. The methods outlined which were used to observe signatures of pair-condensation in the unitary Fermi gas have proven to be effective in determining if there were pairs present in the system with zero centre-of-mass momentum. These signatures were observed for harmonically trapped gases, where the density is inhomogeneous and sets the location of certain phase boundaries within the cloud. Also, the measurements were trap-averaged, meaning any information about the location of the discontinuities versus any local length scale is difficult to extract.

One of the goals of this research is to identify the local onset of pair-condensation as the relative temperature,  $T/T_F$ , reaches below the critical temperature for condensation  $T_C/T_F$ . This will take advantage of Bragg spectroscopy except in this case, the measured density-density response at the resonance for pairs must be homogeneous. The local density approximation is applied here in a way that generalises the scheme presented in [82] so that the measurement of homogeneous dynamic variables becomes possible. Measuring the homogeneous response versus local relative temperature should reveal at what point the gas starts to condense.

The other aim presented here is to measure the temperature dependence of the trap-averaged contact at unitarity. While there have been several theoretical calculations that have provided results on this matter, there is enough of a discrepancy between them to take a closer look. In [63] a breakthrough measurement of the contact for a cold gas was performed, the significance in this result being the precision. Therefore, we aim to perform similar experiments with slightly hotter clouds in order to build up a curve showing the temperature dependence of the contact parameter to a high precision. We are hoping to compare the precise experimental results to the theoretical calculations and shed some light on how the contact behaves around the critical temperature.

### 1.3 Thesis outline

Chapter 1 introduces the relevant literature and presents the problems that are to be addressed in this thesis.

Chapter 2 gives an introduction to Fermi gases, by starting from the ideal case and then introducing some relevant two-body and many-body theories that help to explain two-component Fermi gases in the BCS-BEC crossover and in the unitarity regime. This is followed by an introduction into universality and the Tan relations, before a discussion on the collective and single-particle excitations that can occur in the BCS-BEC crossover.

Chapter 3 is an experimental chapter where the details are presented of the machine used to produce the strongly interacting Fermi gases in our laboratory. This is followed

by details on the extraction of the atomic density from the integrated column density obtained from images, and then calibrations of the atom number for our imaging system.

Chapter 4 is dedicated to understanding the probe that we use on the strongly interacting Fermi gases in this thesis. The experimental realisation of Bragg spectroscopy, and the theory describing linear response and particle conservation are given to understand how we can interpret our data using this technique.

Chapter 5 presents the first main results in this thesis. A method that can be used to extract local dynamic variables is introduced and then utilised to find the homogeneous density-density response which shows the *in situ* observation of pair-condensation in a unitary Fermi gas.

Chapter 6 present results on the temperature dependence of Tan's contact parameter for a trap-averaged Fermi gas. This includes the methodology and comparisons to previous experimental measurements and theoretical calculations. It also includes preliminary measurements of the homogeneous contact.

Chapter 7 summarises the main findings of this thesis and provides an outlook for possible future experiments.

# Chapter 2

## Overview of strongly interacting Fermi gases

### 2.1 Introduction

Studying ultracold gases allows new insight into various aspects of interacting quantum systems. From an experimental point of view, these many-body systems can be measured and probed on a macroscopic basis, yet full details of the microscopic properties are known. In many cases, variables within the system can be readily tuned giving access to different physical behaviours. In ultracold two-component Fermi gases, *s*-wave interactions can be tuned to any value via a Feshbach resonance. In the laboratory, we use ultracold  ${}^6\text{Li}$  to study the strongly interacting Fermi gas where the physics becomes universal [36, 37, 91]. This chapter will present an overview of the theoretical picture for this system starting from the ideal case and then discuss how adding a second species into the mix with tunable interactions realises the BCS-BEC crossover. This leads to an introduction on the concept of universality and the Tan relations, followed by a discussion on the excitations in Fermi gases along the BCS-BEC crossover.

## 2.2 Ideal Fermi gases

When a gas is cooled to absolute zero, the particles occupy the lowest energy quantum states available. In a single-component Fermi gas, this corresponds to filling the lowest unoccupied states, as fermions obey the Pauli exclusion principle. A spin-polarised gas of indistinguishable fermions is essentially non-interacting because the lowest order ( $l = 0$ , or  $s$ -wave) collisions which dominate at low energies are forbidden as a fermionic particle must have an antisymmetric wavefunction.

As a gas is cooled towards absolute zero, the phase space density increases according to

$$D = n\lambda_{dB}^3, \quad (2.1)$$

where  $\lambda_{dB} = \sqrt{2\pi\hbar^2/mk_B T}$  is the thermal de Broglie wavelength,  $n$  is the atomic density,  $m$  is the mass of the particles,  $k_B$  is the Boltzmann constant,  $T$  is the temperature in Kelvin and  $\hbar$  is the reduced Planck's constant. Once the de Broglie wavelength reaches the same order as the interparticle separation, the gas enters the quantum degenerate regime. As  $D \rightarrow 1$ , the state occupation statistics need to be described by the Fermi-Dirac distribution, given by

$$n_{FD}(\epsilon) = \frac{1}{e^{\beta(\epsilon-\mu)} + 1}, \quad (2.2)$$

where  $n_{FD}$  is the probability of a state with energy  $\epsilon$  being occupied,  $\mu$  is the chemical potential, and  $\beta = 1/k_B T$ . In most experimental situations, we are interested in atoms confined in a harmonic potential of the form

$$V(x, y, z) = \frac{1}{2}m\omega_x^2 x^2 + \frac{1}{2}m\omega_y^2 y^2 + \frac{1}{2}m\omega_z^2 z^2, \quad (2.3)$$

where  $\omega_x$ ,  $\omega_y$ ,  $\omega_z$  are the trapping frequencies in the  $x$ ,  $y$ , and  $z$  directions respectively. In three dimensions where the energy spacing is much less than the energy of the entire system, a semiclassical approach can be used to obtain the density of states [92, 93]

$$g(\epsilon) = \frac{\epsilon^2}{2(\hbar\bar{\omega})^3}, \quad (2.4)$$

where  $\bar{\omega} = (\omega_x\omega_y\omega_z)^{1/3}$  is the geometric mean of the trapping frequencies. The total number of atoms in the system,  $N$ , is the sum of all occupied states. For small energy spacings the sum can be expressed as an integral which makes use of the density of states

$$N = \int n_{FD}(\epsilon)g(\epsilon)d\epsilon \quad (2.5)$$

and the total energy is the sum of the energy for every single particle, which can also be expressed as an integral:

$$E = \int \epsilon n_{FD}(\epsilon)g(\epsilon)d\epsilon. \quad (2.6)$$

By substituting equations 2.2 and 2.4 into equation 2.5, and setting the temperature to zero, this equation can be solved to yield the chemical potential in terms of the atom number and trap frequencies. At zero-temperature, the chemical potential is equivalent to the highest occupied energy state, which is the Fermi energy:

$$E_F = (6N)^{1/3} \hbar\bar{\omega}. \quad (2.7)$$

## 2.3 Scattering theory

Adding a second species provides access to the phenomena that we are interested in studying. In order to understand the processes that occur in these systems, this section will outline some theory relevant to two ultracold particles undergoing short range interactions. In this scenario we are interested in an elastic collision between two particles of the same mass,  $m$ , with momenta,  $\mathbf{p}_1$  and  $\mathbf{p}_2$ , and position,  $\mathbf{r}_1$  and  $\mathbf{r}_2$ , that interact over a potential  $V(\mathbf{r}_1 - \mathbf{r}_2)$ . Provided that the potential,  $V$ , is spherically symmetric, the centre-of-mass and relative motion can be solved independently to avoid working with the six degrees of freedom, and thereby making the problem simpler. While the centre-of-mass moves around as a particle with twice the mass of a single particle, it is the relative motion ( $\mathbf{r} = \mathbf{r}_1 - \mathbf{r}_2$ , and  $\mathbf{p} = (\mathbf{p}_1 - \mathbf{p}_2)/2$ ) that outlines and simplifies what we want to know about two-body scattering. Therefore, the essential physics can be understood as an elastic process where a particle with a reduced mass,  $m_1m_2/(m_1 + m_2) = m/2$  (when both particles have the same mass), encounters an

attractive spherical scattering potential,  $V(\mathbf{r})$ . Threshold features of this process can be understood by considering  $V(\mathbf{r})$  to be a finite square well with a short range  $R$ .

$$V(\mathbf{r}) = \begin{cases} -V_0, & \mathbf{r} < R \\ 0, & \mathbf{r} > R \end{cases}. \quad (2.8)$$

This problem is treated in a variety of texts including [94–97]. We begin by writing the wavefunction as

$$\psi(r) = e^{ikz} + f(\theta, \phi) \frac{e^{ikr}}{r}, \quad (2.9)$$

which is a combination of the incoming free particle that is a plane wave,  $e^{ikz}$ , traveling along direction  $z$  and the outgoing (spherical) scattered wave,  $e^{ikr}/r$ , where  $r$  is the distance from the origin, and  $f(\theta, \phi)$  is the scattering amplitude. The incoming wave can be approximated as a plane wave because at low temperature the wavepacket is much larger than the van der Waals range. The modulus squared of the scattering amplitude gives the differential cross-section which is the incident flux traveling through an infinitesimal area,  $d\sigma$ , that is scattered into an infinitesimal solid angle,  $d\Omega$ . To simplify the scattering amplitude, we start with the 3D radial Schrödinger equation. By performing a partial wave expansion on the scattered wave and eliminating the  $\phi$  dependence, the scattering amplitude provides the coefficient of the  $e^{ikr}/r$  term at large  $r$

$$f(\theta) = \sum_{l=0}^{\infty} (2l+1) f_l(k) P_l(\cos\theta), \quad (2.10)$$

where  $f_l$  are partial wave amplitudes and  $P_l$  are Legendre polynomials. The scattering cross-section can then be expressed as

$$\sigma = 4\pi \sum_{l=0}^{\infty} (2l+1) |f_l|^2. \quad (2.11)$$

As the potential is spherically symmetric, the amplitude in each partial wave is conserved and can only acquire a phase shift once scattered from the potential. These partial wave amplitudes can be expressed as a function of their phase shifts,  $\delta_l$ . A partial wave expansion on both the incoming plane wave (using Rayleigh's formula) and the overall wavefunction in equation 2.9 (where the outgoing wave has the additional

phase shift) in their asymptotic forms yields

$$f_l(k) = \frac{e^{i\delta_l}}{k} \sin\delta_l = \frac{1}{k \cot\delta_l - ik}. \quad (2.12)$$

Substituting equation 2.12 into equation 2.11, and using  $\sigma = \sum_{l=0}^{\infty} \sigma_l$ , reveals the partial cross-sections:

$$\sigma_l = \frac{4\pi}{k^2} (2l+1) \sin^2\delta_l. \quad (2.13)$$

At low temperatures, the  $l > 0$  terms are frozen out as the effective potential provides a near impenetrable centrifugal barrier for low energy particles. When  $k \rightarrow 0$  (ultracold temperatures), the wavefunction outside the well ( $r > R$ ) is approximately linear due to the long wavelength of the sin term and its gradient depends on the depth of the potential. The point along  $r$  in which the outside wavefunction crosses zero is defined as the  $s$ -wave scattering length,  $a$ , which is illustrated in figure 2.1.

This is connected to the partial phase shift by solving the continuity equations where the outside wave is  $u(r) = \text{constant}(r - a)$  and the inside wave is  $u(r) = \sin(kr + \delta_0)/k$

$$a = -\lim_{k \rightarrow 0} \frac{1}{k} \tan\delta_0, \quad (2.14)$$

where  $r = 0$ . Substituting this back into equation 2.12 and then into equation 2.10, the  $l = 0$  cross-section is

$$\sigma_0 = \frac{4\pi a^2}{1 + k^2 a^2}. \quad (2.15)$$

For weak interactions,  $|ka| \ll 1$ , the cross-section varies as  $\sigma = 4\pi a^2$ ; however when  $|ka| \gg 1$ , the cross-section is entirely dependent on the de Broglie wavelength:  $\sigma = 4\pi/k^2$ . In this limit, all of the microscopic details of a particular atom that determine the scattering length have fallen out of the problem, and this is known as the unitarity limit.

The scattering amplitude in equation 2.12 can be expressed in terms of an effective interaction range,  $r_{\text{eff}}$ , through the expansion of  $k \cot\delta_l$  (using equation 2.14) up to order  $k^2$ :

$$f_0(k) = \frac{1}{-\frac{1}{a} + r_{\text{eff}} \frac{k^2}{2} - ik}. \quad (2.16)$$

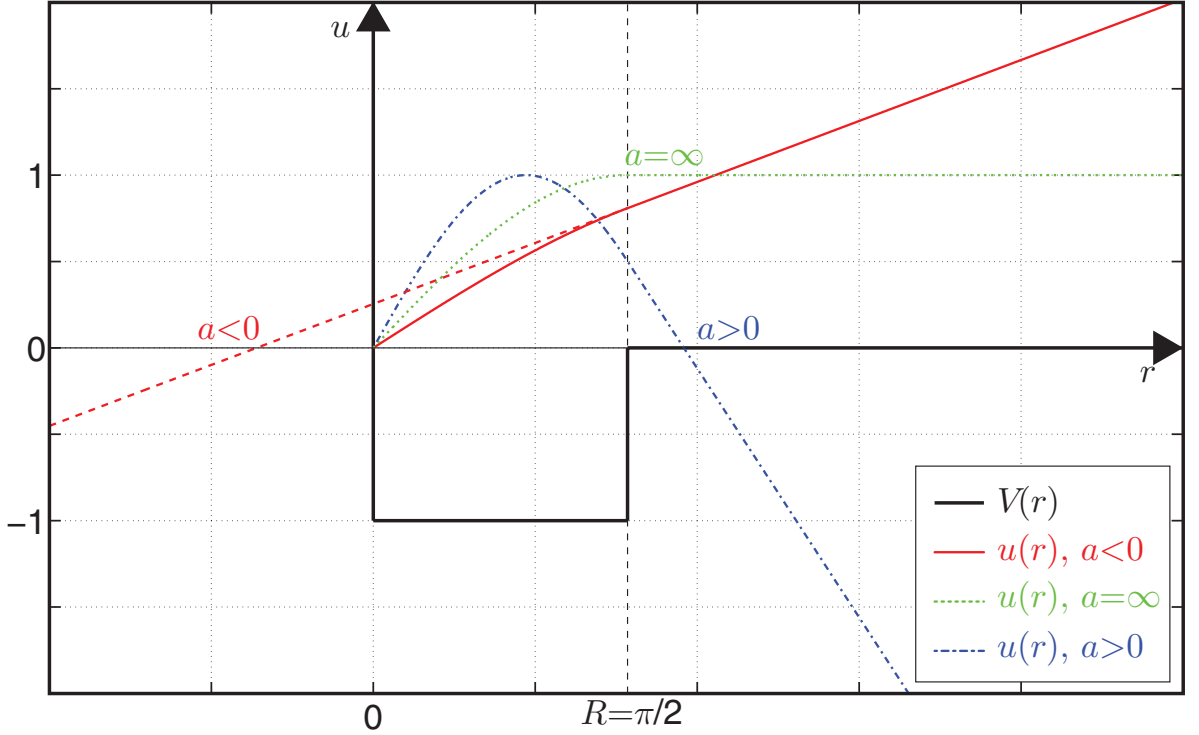


Figure 2.1: Definition of the  $s$ -wave scattering length, where the vertical axis represents  $u(r) = r\psi(r)$ , and the horizontal axis is  $r$ . The thick black solid line is the potential in the centre-of-mass frame,  $V(r)$ , and the thin black dashed line shows  $r = R$ . The blue dot-dashed line crosses zero outside of the potential, meaning that the  $s$ -wave scattering length is positive. The wavefunction represented by the solid red line does not cross zero but the scattering length can be found by backtracking along the red dashed line which crosses zero at  $r < 0$ , meaning that the  $s$ -wave scattering length is negative. In the case of an infinite scattering length, the wavefunction which is represented by the green dotted line never crosses zero. All three of these curves show the dependence of the  $s$ -wave scattering length on the acquired phase shift from the potential.

For positive scattering lengths, and wavevectors much smaller than the inverse of the effective range, solving the poles of the inverse  $s$ -wave scattering amplitude,  $f_0^{-1}(k) = 0$ , gives the molecular binding energy

$$E_b = \frac{\hbar^2}{2ma^2}, \quad (2.17)$$

where the potential well can support a bound state with a wavevector  $k = \sqrt{2mE_b}/\hbar$  as

long as the depth,  $V$ , exceeds a critical well depth,  $V_C$ , defined by the the range of the potential [90, 98, 99]. The binding energy close to the resonance is nearly independent of the details of the interaction potential and the molecules have a characteristic size of approximately  $a$ . However it should be noted that in three-dimensions, when  $a < 0$  the interatomic potential does not support a bound state.

## 2.4 Feshbach resonances

A key element in the following experiments is the ability to tune the interactions between the two species in the mixture via a magnetic Feshbach resonance (or as it is sometimes called a Fano-Feshbach resonance). First described around the 1960's in the context of nuclear interactions [6, 100, 101], a Feshbach resonance can be used to vary the  $s$ -wave scattering length that describes the collisions between two particles. In-depth discussions on Feshbach resonances from a quantum gas perspective can be found in [102, 103].

As the fermionic atoms are in their electronic ground states and we are dealing with two different hyperfine states (which we also call “spins”), the eigenstates of the total spin lead to a singlet (triplet) for anti-parallel (parallel) electron spins. For each of these states, we use their respective Born-Oppenheimer potentials to represent the different scattering channels [6] in which their behaviour at long range is approximately described by the van der Waals potential  $-C_6/r^6$ , where  $C_6$  is the van der Waals dispersion coefficient. These are illustrated in figure 2.2.

In this picture, the pair of atoms enter their scattering region from large  $r$  via the triplet potential, which is called the open channel. Outside the scattering region, the singlet potential, which is referred to as the closed channel, is energetically inaccessible as its continuum energy is larger than the free particle energy. The closed channel can only be accessed within the scattering region where its bound states can mix with the scattering state of the shallow open channel, which is enabled by the hyperfine interaction. As the two potentials have differing magnetic moments, it is possible to tune their relative energy through a resonance with an external magnetic field. The Feshbach resonance occurs when the energy of the highest lying bound state in the

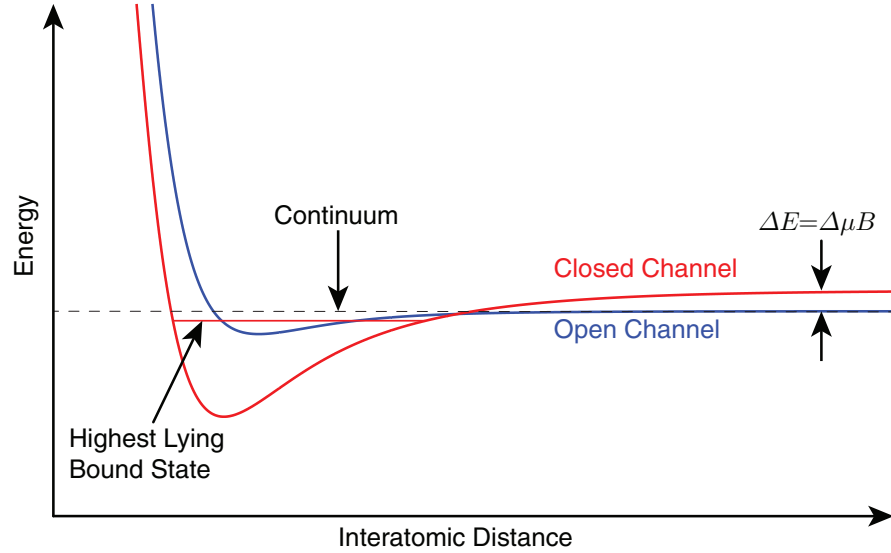


Figure 2.2: Illustration of the two different scattering channels. The Feshbach resonance is realised when the energy of a bound state in the closed channel becomes equal to the threshold energy in the open channel.

closed channel becomes degenerate with the free particle energy and it is at this point that the  $s$ -wave scattering length changes sign and diverges. When the bound state lies below the triplet continuum, the  $s$ -wave scattering length is positive and it is energetically favourable for the two particles to form a bound dimer (with some energy release). Conversely, there is no bound state when the bound energy level lies above the continuum. So essentially, with the sweep of a magnetic field, pairs of atoms can be converted to molecules with varying binding energy, or vice versa.

A magnetic Feshbach resonance for alkali atoms was first predicted in [104] and first observed in a BEC back in 1998 [7]. It was later used to realise the first fermionic condensates [18, 64, 86, 87, 105, 106]. In both of the alkali isotopes used so far in strongly interacting Fermi gas experiments,  ${}^6\text{Li}$  and  ${}^{40}\text{K}$ , there exists a broad Feshbach resonance<sup>1</sup> ([68, 107] and references within). In the case of  ${}^6\text{Li}$ , the  $s$ -wave scattering lengths have been precisely measured at Heidelberg for each combination of the three lowest hyperfine states [107]. These are plotted in figure 2.3.

The experiments described in this thesis use ultracold  ${}^6\text{Li}$  in the two lowest hyperfine

<sup>1</sup>the  ${}^6\text{Li}$  Feshbach resonance is much broader than the case for  ${}^{40}\text{K}$

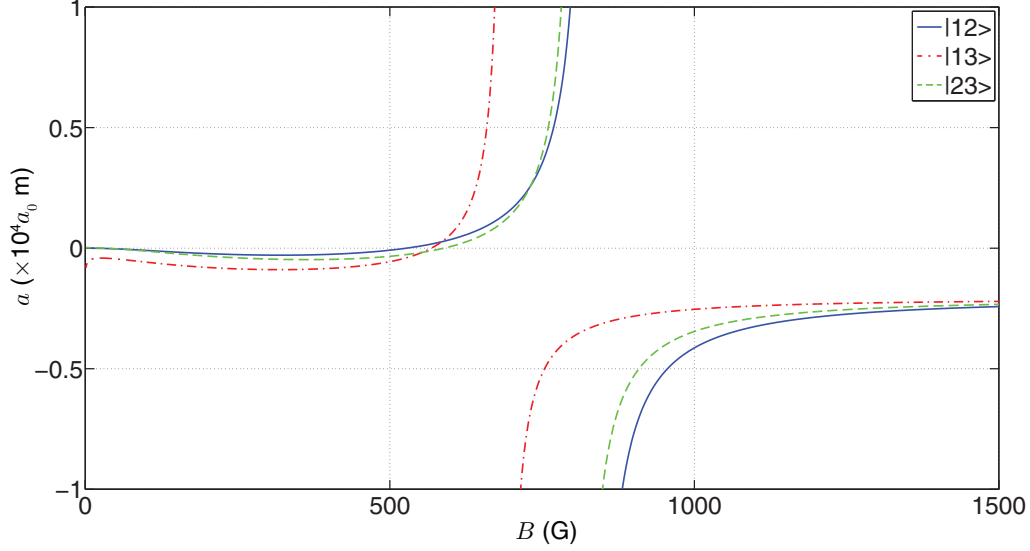


Figure 2.3:  ${}^6\text{Li}$  scattering lengths for combinations of the three lowest hyperfine states as measured in [107], where  $a_0$  is the Bohr radius. The blue solid line is the scattering length between  $|1\rangle$  and  $|2\rangle$  where the Feshbach resonance is 832.18 G, the red dot-dashed line is the scattering length between  $|1\rangle$  and  $|3\rangle$  where the Feshbach resonance is 689.68 G, and the green dashed line is the scattering length between  $|2\rangle$  and  $|3\rangle$  where the Feshbach resonance is 809.76 G.

states ( $|F = 1/2, m_F = \pm 1/2\rangle$ ) which corresponds to the blue curve in figure 2.3 where the Feshbach resonance is  $B_0 = 832.18$  G. The general form of scattering length versus magnetic field around a Feshbach resonance is [108]

$$a(B) = a_{bg} \left( 1 + \frac{\Delta B}{B - B_0} \right), \quad (2.18)$$

where  $\Delta B = -262.3$  G is the width of the resonance. It should be noted that in the presence of no coupling between the two channels, there is still scattering occurring in the triplet channel. This means it is necessary to include the background scattering length term in equation 2.18,  $a_{bg} = -1582 \times a_0 \text{m}$  [107], where  $a_0$  is the Bohr radius. The large background scattering length arises because the triplet potential is almost deep enough to support another bound state but falls just shy of it, thus giving  ${}^6\text{Li}$  its exceptionally broad Feshbach resonance, making it an ideal candidate for studying

strongly interacting Fermi systems in the laboratory.

Despite it being energetically favourable for bound molecules to form at positive scattering lengths, the binding energy still needs to be released in order for association to occur. If a third atom is located near the pair, within a distance on the order of the scattering length, a pair can form and the resulting kinetic energy is shared between the molecule and the third atom in a process known as three-body recombination [109]. In order for lower bound states within the singlet potential to become occupied, more binding energy must be transferred to the third particle in the collision which necessitates three atoms to be within the range on the order of their interatomic potential. This requires three atoms to come together within a distance of the van der Waals length, which is much less than the thermal de Broglie wavelength. In a Bose gas this is allowed, which causes large amounts of kinetic energy to be released, resulting in significant loss due to heating in gases of molecules consisting of two bosons. However in a two-component Fermi gas, two of those atoms must be in the same spin state, so Pauli exclusion inhibits this process meaning that high lying bound states become stable against inelastic decay [12]. At large scattering lengths, this results in two-component Fermi gases having extremely long lifetimes compared to ultracold Bose gases.

## 2.5 To the many-body picture

We have seen in the previous section how an external magnetic field can tune the attraction between two opposite spin fermions via the  $s$ -wave Feshbach resonance and this two-body picture is well understood. However, this is not the full story as pairing mechanisms can also arise due to many-body effects. Yet it is the system's ability to support a bound state that plays an important role in how the two-component Fermi gas behaves. Certain state variables tend to be measured as a function of the interaction parameter,  $1/k_F a$ , which is given by the scattering length,  $a$  and Fermi wavevector,  $k_F = \sqrt{2mE_F}/\hbar$ . Two separate regimes each determined by the sign of the interaction parameter are smoothly connected as  $1/k_F a$  passes through zero. This is the BCS-BEC crossover and detailed reviews on this subject can be found in [98, 103, 110, 111]. This section will briefly outline the well known limits of this crossover, where  $|a| \rightarrow 0$  and

also the region where  $|a| \rightarrow \infty$ , which is the subject of experiments carried out in this thesis work, as well as explaining the phase diagram shown in figure 2.4.

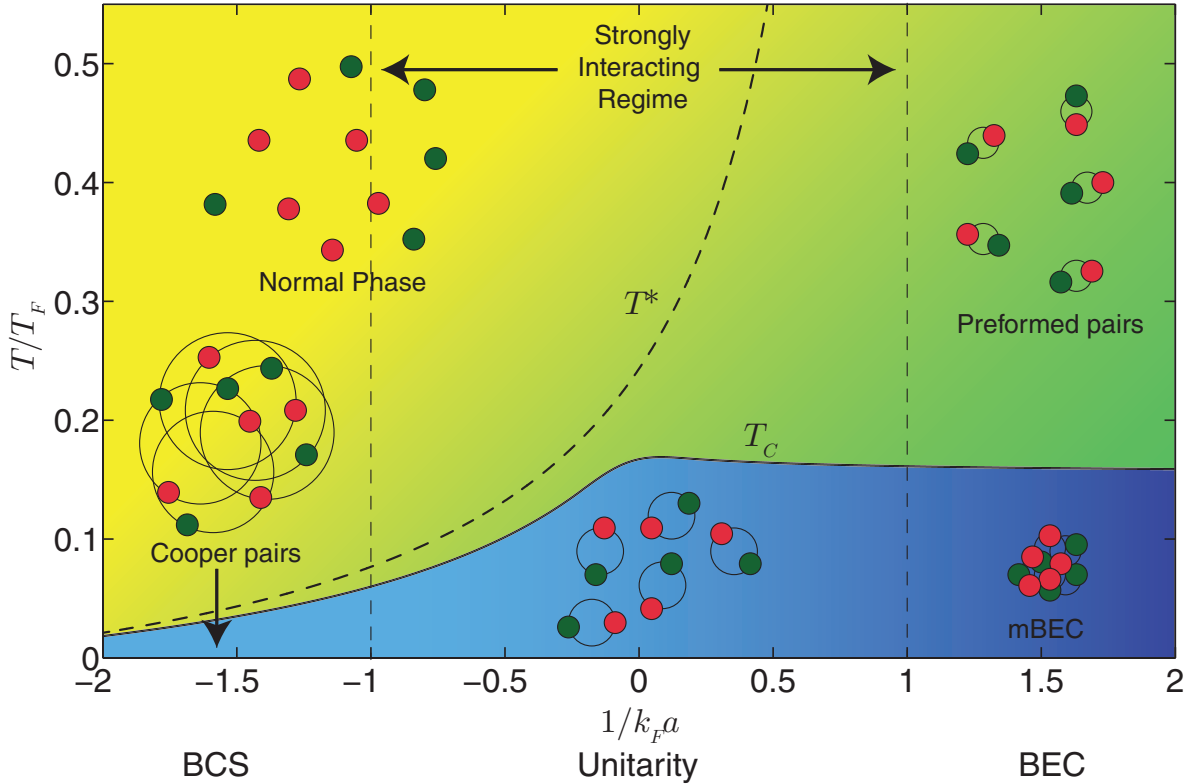


Figure 2.4: A qualitative BCS-BEC crossover phase diagram for a homogeneous two-component Fermi gas as a function of  $1/k_F a$  and  $T/T_F$ . The curve representing  $T_C$  is approximate to what was found [112], but has been shifted down to align with  $T_C$  measured experimentally for  $1/k_F a = 0$  [80].

### 2.5.1 Weakly interacting BEC limit

When the scattering length is small but greater than zero, the two opposite spin fermions can form a stable bound molecule and their spins add up to form an integer spin composite boson. This behaviour occurs when the relative temperature  $T/T_F$  reaches below a temperature,  $T^* \rightarrow E_b/k_B$  (in the BEC limit), known as the pairing temperature, where we have a gas of bosonic molecules. Because the pairs have an integer spin, these molecules are bosons, so below  $T_C$  many pairs condense into a molecular BEC (mBEC),

which can be described by the Gross-Pitaevskii equation [93]. In a three-dimensional Fermi gas, superfluidity coincides with pair-condensation. As  $a$  decreases, the binding energy increases meaning that the average size of the pairs becomes smaller. This has the consequence of a shorter lifetime for a weakly interacting mBEC due to the gas becoming more bosonic, and thus the suppression of inelastic loss due to Pauli exclusion is now less effective. In this limit at  $T = 0$  K, the condensate density,  $n_c$ , can be written using the Thomas-Fermi approximation which ignores the kinetic energy term [90]

$$n_c(\mathbf{r}) = \frac{15N}{16\pi^2 R_x R_y R_z} \left( 1 - \sum_i \frac{x_i^2}{R_i^2} \right), \quad (2.19)$$

where  $N$  is the total atom number,  $x_i$  are the Cartesian coordinate vectors and  $R_i$  are the Thomas-Fermi radii given as

$$R_i = \sqrt{\frac{2\mu_M}{m\omega_i^2}}, \quad (2.20)$$

with  $\mu_M$  being the molecular chemical potential. To achieve mBEC, the dimer-dimer collisions play a role and the scattering length between bound molecules has been calculated to be  $a_m = 0.6a$  [12]. As these condensates are generally interacting they also display superfluidity as seen in atomic BECs.

### 2.5.2 Weakly interacting BCS limit

For small and negative scattering lengths, no two-body bound state is present anymore, so it might seem intuitive that no pairs are present in the gas. At low temperatures when the lowest momentum states are filled to form a Fermi sea, scattering into these states becomes inhibited by Pauli blocking. But at the Fermi surface, particles can scatter into the unoccupied states, and particles of opposite spin can form Cooper pairs, in which the atoms in the pair have equal and opposite momentum [13]. Their existence is attributed purely to the Fermi sea because they can only scatter into the small range of states near the sharp edge of the entire surface. At the Fermi surface, the density of states is approximately constant so the scattering is more like the two-dimensional case where there is always an exponentially weakly bound state for any attractive potential.

In the BCS limit,  $T^*$  has essentially merged with  $T_C$  as pairs with finite centre of mass momentum are limited to scattering into states within a circle around the Fermi sphere for a 50-50 spin mixture. Again the pairs in this system have an integer spin so condensation occurs below  $T_C$ , which in this case is lower than in the BEC limit. The ground state wavefunction in the BCS regime is given as [14]

$$|\Psi_{BCS}\rangle = \prod_k \left( u_k + v_k c_{k\uparrow}^\dagger c_{-k\downarrow}^\dagger \right) |0\rangle, \quad (2.21)$$

where  $u_k$  and  $v_k$  are probability amplitudes that normalise  $|\Psi_{BCS}\rangle$ , and  $c_{k\uparrow}^\dagger c_{-k\downarrow}^\dagger$  is the pair creation operator. The probability amplitudes have the property,  $|u_k|^2 + |v_k|^2 = 1$ , and physically  $v_k$  represents the probability that a pair occupies momentum states,  $(k, \uparrow; -k, \downarrow)$ , whereas  $u_k$  is the probability that these momentum states are empty. Deep within the Fermi sea  $v_k \rightarrow 1$  whereas  $u_k \rightarrow 0$ , and vice versa for outside the Fermi surface. Solving this wavefunction through the application of BCS theory leads to the well known gap and number equations that can be solved simultaneously to yield the chemical potential  $\mu$  and the pairing gap  $\Delta$  in this regime. Physically,  $2\Delta$  describes the amount of energy it takes to break a Cooper pair. The gap equation is [14]

$$\Delta_k = - \sum_{k'} V_{kk'} \frac{\Delta_{k'}}{2E_{k'}}, \quad (2.22)$$

where  $V_{kk'} \propto a$  describes the attractive potential for fermions scattering from  $k'$  and  $-k'$  to  $k$  and  $-k$ , and  $E_k = \sqrt{(\epsilon_k - \mu)^2 + \Delta_k^2}$  is the excitation energy, where  $\mu$  is the chemical potential and  $\epsilon_k$  is the free particle energy. The number equation for the total number of fermions is

$$N = - \sum_k \left( 1 - \frac{\epsilon_k - \mu}{E_k} \right). \quad (2.23)$$

For weak interactions, the Thomas-Fermi radius can be described by a first order perturbative correction away from a non-interacting gas in a harmonic trap by a factor that compresses the gas with increasing scattering length

$$R_i = R_{F,i} \left( 1 - \frac{256}{315\pi^2} k_F |a| \right), \quad (2.24)$$

with  $R_{F,i}$  being the non-interacting Thomas-Fermi radii:

$$R_{F,i} = \sqrt{\frac{2E_F}{m\omega_i^2}}. \quad (2.25)$$

The density distribution is

$$n(\mathbf{r}) = \frac{4N}{\pi^2 R_{F,x} R_{F,y} R_{F,z}} \left( 1 - \sum_i \frac{x_i^2}{R_{F,i}^2} \right)^{3/2}. \quad (2.26)$$

### 2.5.3 Unitarity and the strongly interacting regime

In the region where  $-1 < 1/k_F a < 1$ , the strongest interactions between particles in a gas occur and the system can display both BEC and BCS type characteristics. When the scattering length becomes of the same scale as the interparticle separation, simple perturbation theory is no longer an option in terms of calculating system parameters. At the unitarity regime ( $1/k_F a = 0$ ), the only relevant length scale is the interparticle distance,  $n^{-1/3}$ , and the relevant energy scale is the local Fermi energy, which for any interaction strength can be expressed in terms of the density:  $\epsilon_F = \frac{\hbar^2}{2m} (3\pi^2 n(\mathbf{r}))^{2/3}$ . The homogeneous Fermi wavevector is therefore  $k_F = \sqrt{2m\epsilon_F}/\hbar$  and the homogeneous Fermi temperature is  $T_F = \epsilon_F/k_B$ .

In this strongly correlated regime, several theoretical approaches have been used to describe the system's properties. At zero-temperature, the crossover of the ground state is described by the Leggett model [113] using standard BCS mean field theory. This model was then extended to non-zero temperatures by Nozières and Schmitt-Rink to give an approximate function for  $T_C$  throughout the crossover using what is now known as the NSR model [56]. For  $1/k_F a = 0$ , the pairing gap has been measured experimentally to be  $\Delta = 0.44\epsilon_F$  [114], but the existence of pseudogap pairing, the name given to the region between  $T_C$  and  $T^*$ , is still up for debate. At  $T = 0$ , the chemical potential is scaled away from the Fermi energy by a universal parameter,  $\xi$ , such that  $\mu = \xi\epsilon_F$ .  $\xi$  is known as the Bertsch parameter and it is given by  $\xi = 1 + \beta$ , where  $\beta$  is the ratio of the interaction and the kinetic energy. Recent experimental measurements have shown  $\xi = 0.370$  [80, 107].

To find an expression for the density, the local density approximation can be applied assuming that infinitesimal volumes of the gas are homogeneous. This means the chemical potential varies according to the trapping potential,  $\mu = \mu_0 - V(\mathbf{r})$ , where  $\mu_0$  is the chemical potential in the centre and  $V$  is the trapping potential. The zero-temperature density profile for  $1/k_F a = 0$  can be defined in terms of chemical potential as

$$n(\mathbf{r}) = \frac{1}{6\pi^2} \left( \frac{2m}{\xi\hbar^2} \right)^{3/2} (\mu_0 - V(\mathbf{r}))^{3/2}, \quad (2.27)$$

which then leads to a density profile:

$$n(\mathbf{r}) = \frac{4N}{\pi^2 R_{U,x} R_{U,y} R_{U,z}} \left( 1 - \sum_i \frac{x_i^2}{R_{U,i}^2} \right)^{3/2}, \quad (2.28)$$

where  $R_{U,x,y,z} = \xi^{1/4} R_{F,x,y,z}$ .

Figure 2.4 shows a phase diagram of the BCS-BEC crossover. The properties of the gas are dependent on the interaction parameter,  $1/k_F a$ , and the relative temperature  $T/T_F$ . When  $|a| \rightarrow \infty$ , the interaction parameter becomes zero across the entire system even if it is inhomogeneous, so gas dynamics and critical phenomena rely entirely on  $T/T_F$ . Through dimensional arguments, state variables such as density can be expressed in terms of a dimensionless function,  $F$ , which is a function of the dimensionless variable  $\beta\mu$ , where this time  $\beta = 1/k_B T$  [37]. The density for a three-dimensional gas is given as

$$n(\mu, T) = \frac{1}{\lambda^3} F_n(\beta\mu), \quad (2.29)$$

where  $F_n$  is the dimensionless function that contains the density equation of state. As mentioned previously, the strongly interacting regime is a challenging problem to solve theoretically as  $a$  is no longer a small parameter. For high temperatures, the fugacity,  $Z = e^{\beta\mu}$ , can be used as the small parameter to solve  $F_n$  through a virial expansion [77, 78] which works well down to temperatures of around  $T > 1.2T_F$ . This has been used as a fitting function in the past to extrapolate experimental data to lower temperatures in order to measure the dimensionless parameters down to around  $0.1T_F$  [80]. This work also yielded the experimental observation of the superfluid transition at unitarity giving  $T_C = 0.167T_F$ . Another way of measuring  $F_n$  is from measurements of

the pressure that can be related to the density via the Gibbs-Duhem equation [72, 83]. These experiments used a Bose-Fermi mixture where the Bose gas acts as an external thermometer to measure the temperature of the Fermi gas.

## 2.6 Universality and Tan's contact parameter

In 2001, Heiselberg first predicted that measurements on lab-made strongly interacting Fermi gases in the “intermediate density region”, where  $R \lesssim k_F^{-1} \lesssim |a|$ , could be used to gain insights into other areas of physics including nuclear and neutron star matter [36]. After that in 2004, Ho suggested a universal hypothesis, stating that certain parameters like the scattering length fall out of the problem at a Feshbach resonance meaning the properties of the near resonant Fermi gas are dependent on a few universal parameters [37]. He also indicated that the universal hypothesis also applies to strongly interacting Bose systems which have since been measured [115]. In 2005 it was proposed, then verified experimentally at Duke university, that the unitary Fermi gas obeys the virial theorem analogous to an ideal gas [74]. Also in 2005, Shina Tan realised that a strongly correlated system can be described by a number of exact universal relations which are now known as the Tan relations [39–41]. Overviews of the derivations of these relations are presented in [53, 116] where an extra variable is necessarily included called the contact  $\mathcal{C}$ . A way to visualise the contact is by looking at the discrepancy between the local pair density and the macroscopic density. In an interacting system, the number of pairs within a small volume scales as  $V^{4/3}$ , where  $V$  is volume, rather than what would be expected by simply measuring the number of pairs over a large volume  $V^2$ , thus pair correlations become stronger at short range. This local pair density is proportional to the contact density,  $\mathcal{C}$ , which is a local quantity with units of  $m^{-4}$ . The trap-averaged contact,  $\mathcal{I}$  is the integral of the contact density over all three spatial dimensions:

$$\mathcal{I} = \int \mathcal{C}(\mathbf{r}) d^3\mathbf{r}. \quad (2.30)$$

Therefore we can see through these arguments that the contact represents the likelihood of two particles being close to one another in a system. In dimensionless units, the trap averaged contact is expressed as  $\mathcal{I}/Nk_F$  whereas the homogeneous dimensionless

contact density is  $\mathcal{C}/nk_F$ .

The original definition of the contact comes from looking at the momentum distribution. For large values of  $k$ , the contact is the amplitude of the tail which scales as  $k^4$ . The formal definition for this is

$$\mathcal{I} = \lim_{k \rightarrow \infty} k^4 n(k), \quad (2.31)$$

where  $n(k)$  represents the density of atoms with momentum  $k$ . Measurements of this tail were made at JILA where a cloud was released from its trapping potential and the interactions are switched off. It is then left to expand revealing  $n(k)$  of the atoms in the trap. Plotting  $k^4 n(k)$ , an asymptote occurs at large- $k$ , giving the contact [68]. Both examples of the contact given so far are manifested through microscopic quantities but the main breakthrough of these universal relations is that  $\mathcal{C}$  also contains information about the bulk thermodynamic properties of the system. The best known example for this is the adiabatic sweep theorem which states that the contact is proportional to the rate of change in total energy,  $E$ , versus the inverse scattering length

$$\left( \frac{dE}{da^{-1}} \right)_{S,N} = -\frac{\hbar^2}{4\pi m} \mathcal{I}, \quad (2.32)$$

where  $E = E_{kin} + E_{pot} + E_{int}$  ( $E_{kin}$  is the kinetic energy,  $E_{pot}$  is the potential energy,  $E_{int}$  is the interaction energy), and the entropy,  $S$ , and the atom number are fixed. This can be combined with the generalised virial theorem to give another Tan relation

$$E_{kin} + E_{int} - E_{pot} = -\frac{\hbar^2 \mathcal{I}}{4\pi k_F a}, \quad (2.33)$$

which, along with the equation 2.32, was also measured in [68]. The Tan relations outlined here are the most common examples; however they come in many different forms as shown in [51] and [55], of which the latter showed that the contact must exhibit critical behaviour across the superfluid transition. Indeed the contact is applicable in a whole variety of scenarios in atomic gases including Bose or Fermi gases, equilibrium or non-equilibrium, superfluid or normal phases, and varying spin polarisations, temperature or interactions. The results on the contact in chapter 6 of this thesis are based on measurements of the static structure factor. In order to understand this we start

by looking at the asymptotic wavefunction for weakly bound pairs, known as the Halo wavefunction [98, 102]:

$$\phi(r) = \frac{e^{-r/a}}{\sqrt{2\pi ar}}. \quad (2.34)$$

Expansion of equation 2.34 to first order for short range ( $r \rightarrow 0$ ) interactions, or contact interactions, shows that the Halo wavefunction goes as  $\phi(r) \propto 1/r - 1/a$  [53, 116]. In fact this form of the wavefunction at short range applies throughout the crossover [40]. Inserting this back into the pair correlation function,  $g_{\uparrow\downarrow}^{(2)}$ , which is the second quantised many-body wavefunction expressed for only one pair of spin anti-parallel particles  $g_{\uparrow\downarrow}^{(2)}(\mathbf{R}) = \int \langle n_{\uparrow}(\mathbf{R} - r/2) n_{\downarrow}(\mathbf{R} + r/2) \rangle d\mathbf{R}$ , the contact density comes in as a coefficient. Integrating reveals the Tan relation for the density-density correlator:

$$g_{\uparrow\downarrow}^{(2)}(r \rightarrow 0) = \frac{\mathcal{I}}{16\pi^2} \left( \frac{1}{r^2} - \frac{2}{ar} \right). \quad (2.35)$$

The spin anti-parallel static structure factor is related to the Fourier transform of the pair correlation function [33]

$$S_{\uparrow\downarrow}(k) = \frac{n}{2} \int \left[ g_{\uparrow\downarrow}^{(2)}(r) - 1 \right] e^{i\mathbf{k}\cdot\mathbf{r}} d\mathbf{r}, \quad (2.36)$$

which at high momentum can be expressed in terms of the contact [48]:

$$S_{\uparrow\downarrow}(k \gg k_F) = \left( \frac{\mathcal{I}}{Nk_F} \right) \frac{k_F}{4k} \left[ 1 - \frac{4}{\pi k_F a} \frac{k_F}{k} \right]. \quad (2.37)$$

Our group have previously measured the contact using Bragg spectroscopy along with the structure factor Tan relation for varying  $s$ -wave scattering lengths [71] and temperatures [35], as well as a precision measurement at unitarity on a cold cloud [63].

## 2.7 Excitations in the BCS-BEC crossover

Since Bragg spectroscopy is the technique used to obtain all of the results in this thesis, we will take a look at what happens when the gas is perturbed by a probe with frequency  $\omega$  and wavevector  $k$ . At low- $k$ , the lowest energy excitation has linear

dispersion indicating that it is a sound wave or phononic excitation where the gradient is equivalent to the speed of sound. This collective excitation is known as the Bogoliubov-Anderson mode. As  $k$  increases, the dispersion evolves to become quadratic, indicating we are in the single particle regime due to the length scale of the probe decreasing [117]. In this regime, we can Bragg scatter bosonic pairs or fermionic atoms due to the ability of the probe to break the pairs. These are illustrated in figure 2.5, which is taken directly from [118].

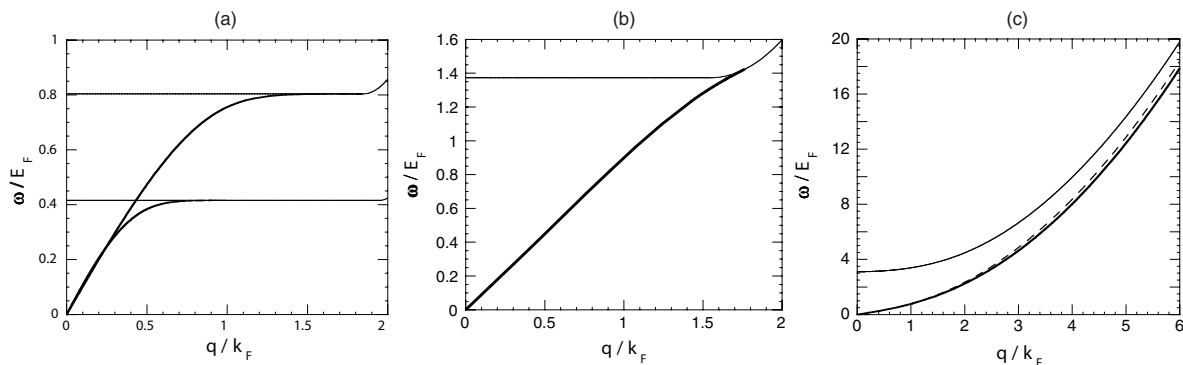


Figure 2.5: Qualitative plots from reference [118] showing the dispersion relations  $\omega/E_F$  of the collective modes as a function of  $k/k_F$  (where  $k$  is denoted with a  $q$  in these plots) for varying interaction parameters including (a)  $1/k_F a = -1$  (lower thick line) and  $1/k_F a = -0.5$  (upper thick line), (b)  $1/k_F a = 0$ , and (c)  $1/k_F a = 1$ . In each of these figures, the thin solid line represents the pair breaking threshold and the dashed line in (b) and (c) represents the collective mode obtained from the Bogoliubov formula. Reprinted figures with permission from R. Combescot, M. Y. Kagan, and S. Stringari, “Collective mode of homogeneous superfluid Fermi gases in the BEC-BCS crossover,” *Physical Review A* **74**(4), 042717 (2006). Copyright 2015 by the American Physical Society (doi: 10.1103/PhysRevA.74.042717).

Figure 2.5 shows a qualitative representation of the excitation spectrum in a Fermi gas for different interactions. The dispersion of the Bogoliubov-Anderson mode (thick lines) always starts out as linear at low- $k$  before merging with the single particle excitations at high- $k$ . However, the threshold energy for the pair breaking continuum (thin lines) can damp the collective mode, depending on the amount of energy required to break the pair. In figure 2.5(c) for a mBEC, the collective branch and the pair breaking threshold never meet as  $k$  increases because there is always a finite amount of energy required to break the pairs. As  $1/k_F a$  decreases, the collective and single particle ex-

citations will eventually merge at high values of  $k/k_F$  as shown in figure 2.5(b). At unitarity it is still possible to measure the speed of sound at low- $k$  before the mode hits the pair breaking continuum. With further decreasing of the interaction parameter to  $1/k_F a < 0$ , the energy required to break the pair, set by twice the pairing gap,  $2\Delta$ , also decreases and therefore so does the threshold energy of the continuum for a given  $k$ . So as the gas becomes weakly interacting in the BCS regime, the linear dispersion exists only for very low- $k$  before the collective mode merges with the pair breaking excitations. This is shown in figure 2.5(a) where the modes quickly become damped after they merge with the pair breaking continuum. For the purposes of our experiments, we are interested in the excitation spectrum at high momentum where we probe the single particle response and the dispersion is clearly quadratic meaning we are sensitive to the momentum of single pairs and atoms.

## 2.8 Summary

This chapter gave an overview of the theoretical background for this thesis. This included a summary on the ultracold single component Fermi gas and the scattering of two particles.

This leads to the ability to tune the  $s$ -wave scattering length between two particles of different spins via the magnetic Feshbach resonance. Some insight is given into the many-body properties of the gases through the BCS-BEC crossover and, most importantly for the context of this work, the unitarity regime.

It is then followed by an explanation of universality in the unitary regime including a discussion of Tan's universal relations as well as the contact parameter, plus an overview on how to extract the contact parameter from the high momentum static structure factor. To finish the chapter, there is a section outlining the excitation spectra of two-component Fermi gases across the BCS-BEC crossover, which connects to our Bragg spectroscopy measurements as we use a high- $k$  probe.

# Chapter 3

## Experimental setup and image calibration

### 3.1 Introduction

In order to understand the states of matter described in the previous chapter, and the results of this thesis, a sophisticated experimental apparatus is necessary to cool the  ${}^6\text{Li}$  from above room temperature down to temperatures on the order of 10s of nanoKelvin. The backbone of the Fermi gas machine in our laboratory at Swinburne was built in the mid 2000s and has been in operation since 2008 [119]. Since then, various modifications and improvements have been made to improve the efficiency of the machine and these are described sequentially in the following theses from our group [120–123]. As is a formality in these other theses, this chapter will give a brief overview of the basics of the experimental apparatus including the oven, Zeeman slower and magneto-optical trap (MOT) and how we achieve superfluidity before going into a deeper discussion on the important aspects that are relevant to the results presented in this thesis. This covers the details of the new highly harmonic red-detuned trap used in these experiments, absorption imaging, measuring the homogeneous density, thermometry, and an accurate image calibration.

## 3.2 Initial cooling stages

A good review on the properties of  ${}^6\text{Li}$  can be found in [124] which mentions that lithium at  $T < 453$  K is generally in its solid form and that the wavelength of both  $D$  transitions in  ${}^6\text{Li}$  is around 671 nm. It might seem a little strange that we work with ultracold lithium in its gaseous form; however the methods used to laser cool the lithium means it remains dilute enough to avoid forming a liquid or solid. The gas cannot be exposed to the atmosphere, so the experiment takes place inside an ultra high vacuum chamber. The experimental setup for the initial cooling stage is illustrated in figure 3.1.

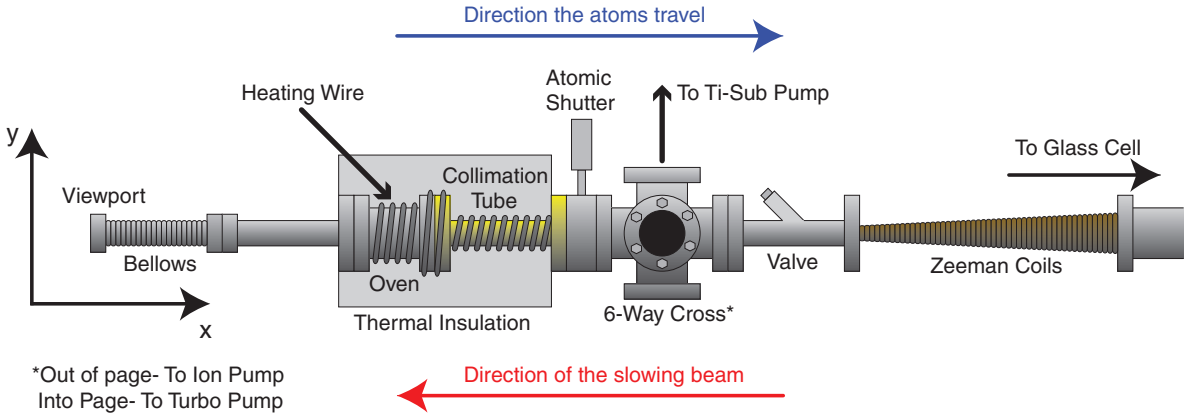


Figure 3.1: A not to scale side view of the initial cooling stages in the experiment including the oven and the Zeeman slower.

Here, solid lithium is heated up to around 350 °C in an oven making it hot enough to release a small amount of vapour. The heat for the oven is provided by heating wire and insulated with many layers of aluminium foil. Cooling this vapour means robbing the particles of their kinetic energy. At the start of a new experimental sequence, an atomic shutter opens up, allowing the atoms to pass through a 10 cm collimation tube and come out the other end as an atomic beam. The average velocity of the atoms in the beam is given as [125]

$$v_b = \frac{3}{4} \sqrt{\frac{2\pi k_B T}{m}}, \quad (3.1)$$

which amounts to  $v_b \approx 1740$  m/s. This is far greater than the capture velocity of

any MOT so the atoms are slowed by a counter propagating laser beam that is red detuned away from resonance with the atoms traveling at  $v_b$ , so it only captures a small percentage of atoms traveling at slower speeds in the tail of the Maxwell-Boltzmann distribution. These slower atoms are most likely to be able to absorb and scatter the photons. The momentum transferred to the atoms from the photons results in a net decrease in velocity in the direction of the atomic beam. The laser light is circularly polarised so that the atoms cycle between the same pair of hyperfine sublevels on an efficiently closed transition. This slowing laser beam is one of the components of the Zeeman slower, and the bellows and viewport shown in figure 3.1 are used to help align this beam. As the atoms slow down, they are Doppler shifted out of resonance with the laser light, so in order to slow them down further, a spatially varying magnetic field is applied, provided by the Zeeman coils shown in figure 3.1, which makes up the other component of the Zeeman slower. This magnetic field has a gradient such that as the atoms get slowed down, their Doppler shift is compensated by a Zeeman shift. The strength of the magnetic field increases as the atoms travel further away from the oven so that the Zeeman slower light is far detuned for atoms captured in the MOT. The polarisation of the laser beam must be  $\sigma^-$  enabling the Zeeman sublevels to shift in the right direction. After exiting the Zeeman slower, the atomic beam enters the science cell which is made of transparent quartz crystal so the atoms can be exposed to all of the different lasers required for our experiments. Here, the slowest atoms in the beam have lost enough of their kinetic energy to be captured by the MOT.

A sketch of the MOT along with the second half of the apparatus is shown in figure 3.2. A MOT consists of three orthogonal pairs of counter propagating laser beams and two magnetic field coils. Using the same principle that the Zeeman slower uses, these optical beams are circularly polarised and they apply a force to the atoms along their direction of propagation. The three sets of beams meet in the centre. An atom in the trapping region is Doppler shifted into resonance with the laser beam it is moving towards, hence slowing it and forming an optical molasses. The magnetic field coils are placed opposite each other in an anti-Helmholtz configuration so that the trap is exactly half way between the two coils. The current flow in both coils travel in opposite directions to each other which creates a magnetic field that goes to zero in the centre but grows in every direction as the distance from the trap centre increases.

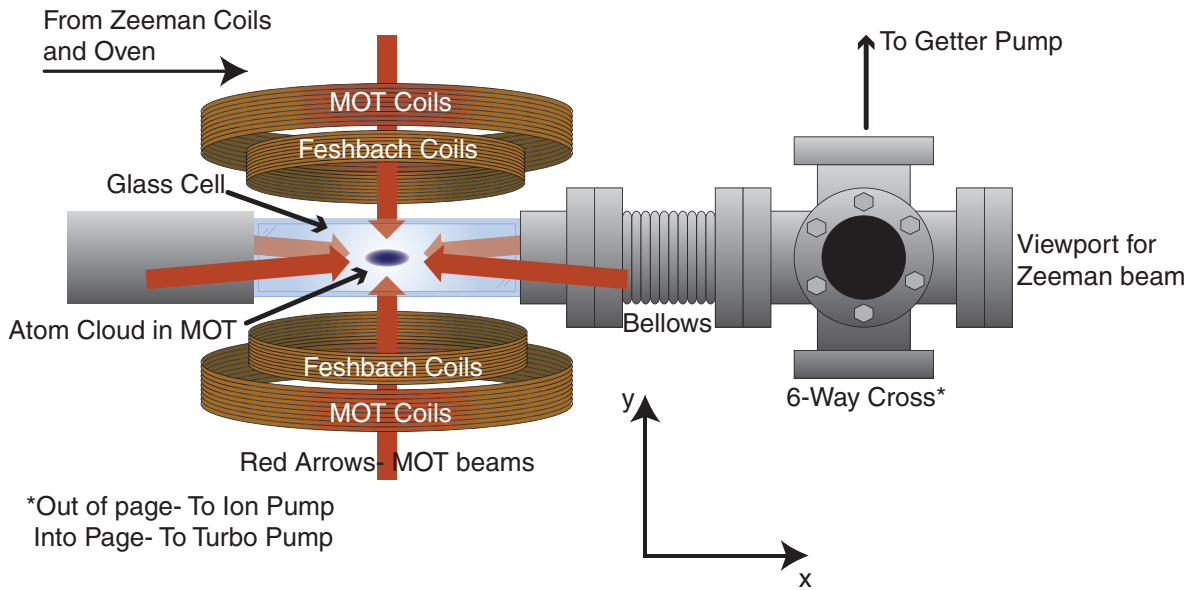


Figure 3.2: A not to scale illustration of the MOT, viewing from the side. This figure is a continuation of figure 3.1.

This allows the atoms to be trapped, as the scattering force now acquires a spatial dependence.

An energy level scheme showing the MOT cooling transition and repump is given in figure 3.3. The transition that provides the primary cooling is the  $D_2$ -line with  $|F = 3/2\rangle$  (ground state)  $\rightarrow |F' = 5/2\rangle$  (excited state); however a small proportion of the atoms can be excited to the  $|F' = 3/2\rangle$  state which can then relax to the  $|F = 1/2\rangle$  and can no longer be cooled on the main cooling transition. It is therefore necessary to include an additional frequency within these optical beams known as the repumper beam. The repumper beam is tuned to the transition frequency required to excite the  $|F = 1/2\rangle$  state to the  $|F' = 3/2\rangle$ , from where it can decay back into the cooling state and can continue to be cooled and trapped by the MOT. After around 30 s,  $\sim 10^9$  atoms have been captured in the MOT and it is then that the cloud goes through a compression stage where the MOT lasers are tuned closer to resonance and the atoms

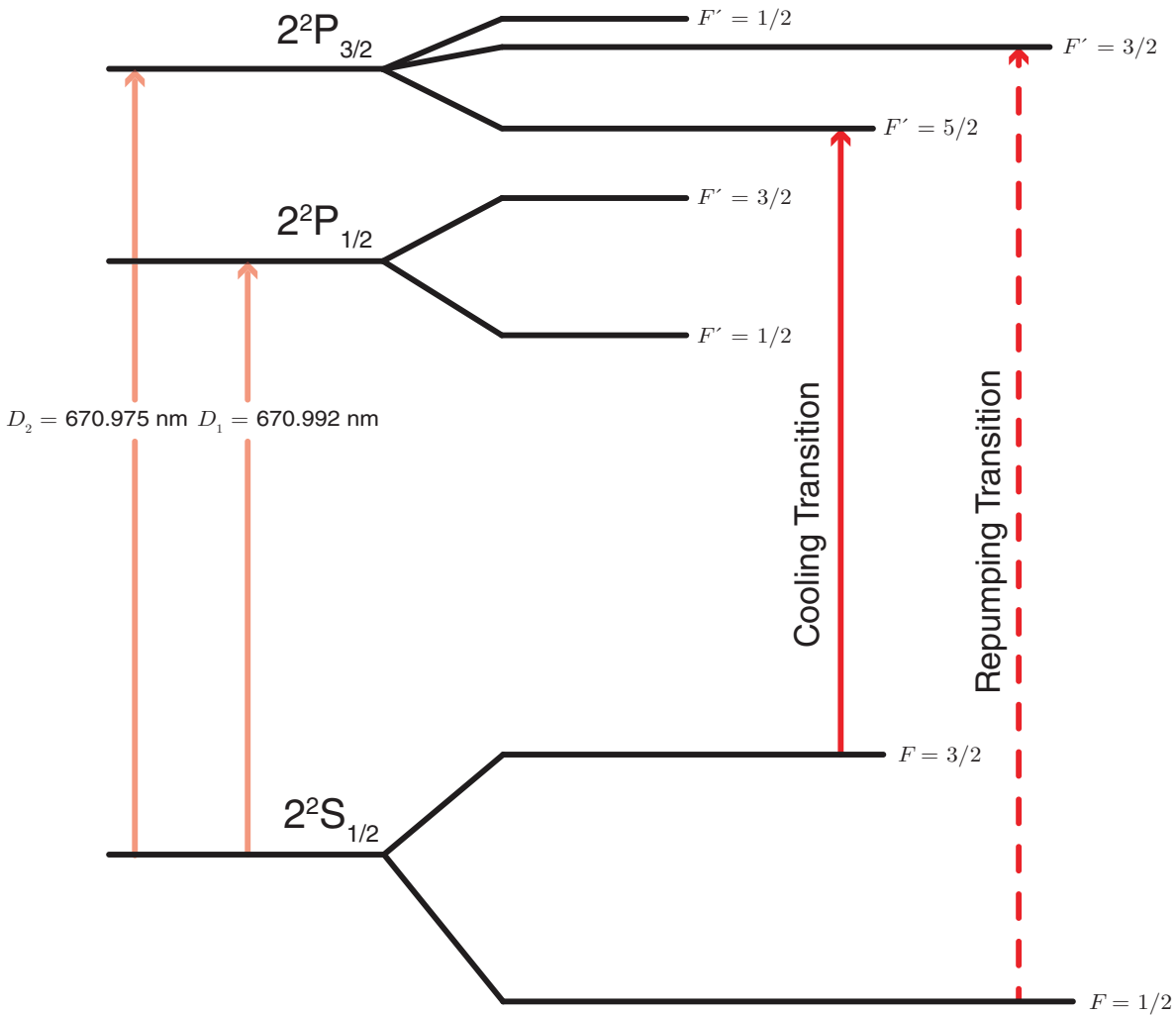


Figure 3.3: Energy level diagram for the MOT cooling transition in  ${}^6\text{Li}$ . The faded vertical arrows represent the two  $D$  transitions, the red solid arrow is the main trapping transition and the red dashed arrow is the repumping transition. Despite quoting the  $D$  lines in terms of wavelength in the figure, the electronic transitions and fine structure splittings are in terms of energy (albeit not to scale).

are pumped back into the  $|F = 1/2\rangle$  state. The magnetic field gradient is also ramped up by increasing the current in the MOT coils to compress the cloud which serves to increase the density. As the atoms are not yet close to degeneracy, they are then loaded into an optical dipole trap (ODT) for further cooling, a depiction of which is shown in figure 3.4.

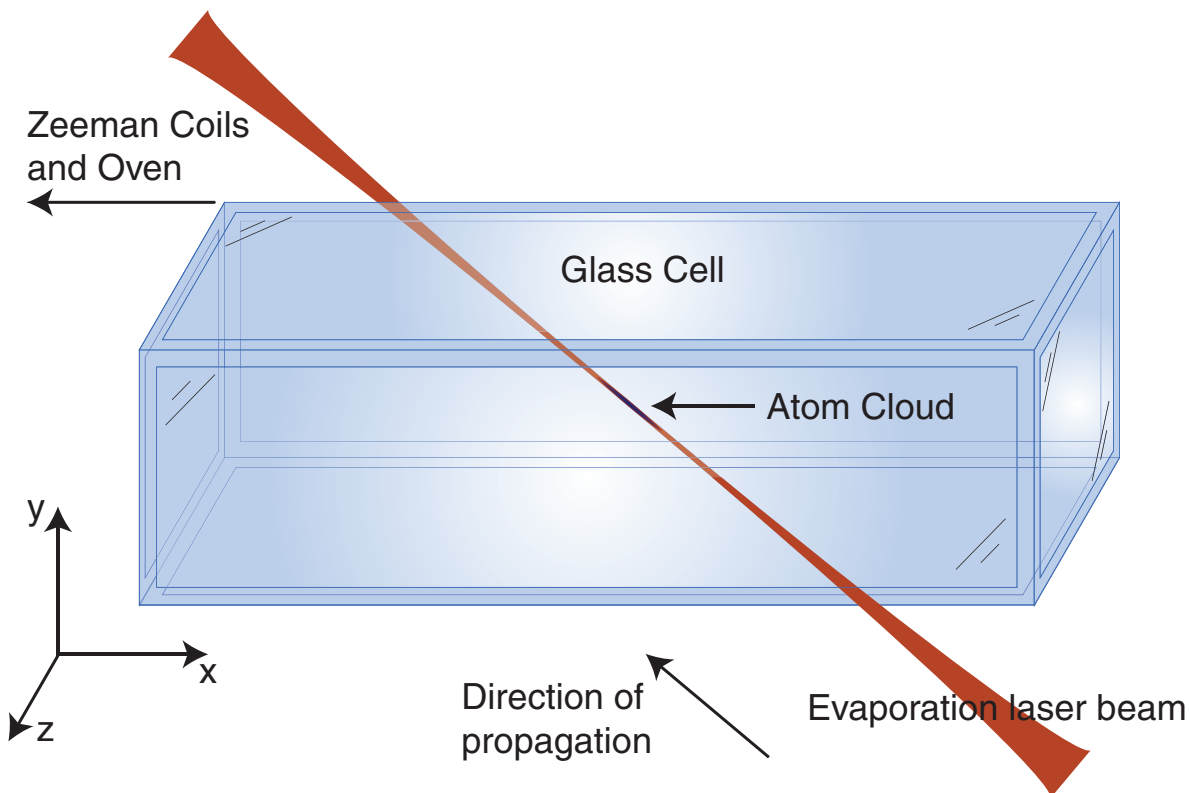


Figure 3.4: An illustration of the ODT that is loaded from the MOT and is then used to evaporatively cool the atoms.

This ODT uses far red-detuned laser light at a high intensity to create a trapping potential for the atoms with low spontaneous emission to avoid heating. This trapping scheme uses the AC Stark effect where the electric field provided by the laser light induces a dipole moment which leads to a dipole force between the atoms and light. The dipole force is proportional to the intensity gradient provided by the inhomogeneous optical field (typically a Gaussian) and the dipole potential experienced by an atom in the driving field is proportional to the intensity of the field. The polarisability determines the relationship between the induced dipole moment and the electric field. The dipole potential,  $U_{\text{dip}}$ , and the spontaneous scattering rate,  $\Gamma_{\text{sc}}$ , are given, respectively, as [126]

$$U_{\text{dip}}(r) \cong \frac{3\pi c^2 \Gamma}{2\omega_0^3 \delta} I(r), \quad (3.2)$$

$$\Gamma_{\text{sc}}(r) \cong \frac{3\pi c^2}{2\hbar\omega_0^3} \frac{\Gamma^2}{\delta^2} I(r), \quad (3.3)$$

where  $c$  is the speed of light,  $\omega_0$  is the resonant frequency of the atoms,  $\Gamma$  is the natural linewidth,  $I$  is the light intensity and  $\delta = \omega - \omega_0$  is the detuning of the light frequency  $\omega$  with respect to  $\omega_0$ . For our red-detuned trap,  $\delta < 0$  so the dipole potential is negative, meaning that the atoms are attracted to the high intensity regions of the field. Because the dipole potential is proportional to  $I/\delta$  and the scattering rate is proportional to  $I/\delta^2$ , having a large detuning and high intensity means that the spontaneous photon scattering rate can be made significantly smaller than the dipole potential such that the atoms can be trapped while heating due to spontaneous scattering is minimal.

As the trap-depth is proportional to the intensity, the optical dipole trap we use in this experiment is 100 W to trap as many atoms from the compressed MOT as possible, and its wavelength is 1075 nm making it far red-detuned. It is a cylindrically symmetric laser beam that propagates along a direction perpendicular to  $y$  at an angle with respect to the front of the glass cell and is focussed at the trap centre, providing a trapping potential as depicted in figure 3.4. As well as ramping up the ODT, a magnetic field is also switched on. This serves two purposes, the main one being to provide the Feshbach field to enhance elastic collisions for subsequent evaporation; however because they are in an imperfect Helmholtz configuration (i.e., the separation of the two coils is larger than the correct Helmholtz configuration), there is a residual magnetic field curvature that provides a trapping potential in the  $x$  and  $z$  directions, thus confining the atoms in all three dimensions. From here, evaporative cooling can start.

The magnetic field is tuned to the strongly interacting BEC side of the Feshbach resonance ( $B = 785$  G, where  $B_0 = 832.2$  G) and a radio-frequency (RF) pulse is switched on that is tuned to the microwave transition between  $|F = 1/2, m_F = \pm 1/2\rangle$  at this specific magnetic field. After the RF pulse has been applied for several Rabi cycles, the interactions within the gas cause decoherence, thus leaving the gas as an incoherent 50-50 spin mixture. Now the depth of the optical trapping potential is reduced by steadily decreasing the laser power and thus the most energetic particles can escape from the trap. Strong interactions enable the gas to re-equilibrate quickly which results in a net decrease in the overall temperature of the gas. After evaporation, we are typically left with  $\sim 2 \times 10^5$  atoms in each spin state at a temperature of around

$\sim 30$  nK or  $0.08T_F^{\text{HO}}$  (where  $T_F^{\text{HO}}$  is the trap-averaged Fermi temperature, defined as  $T_F^{\text{HO}} = E_F^{\text{HO}}/k_B$  where  $E_F^{\text{HO}}$  is given in equation 2.7. Refer to section 3.5 for more details.) depending on what the laser power is at the evaporation end point. At this point, we have finished the preparation of the Fermi gas and we can proceed to experiment with it<sup>1</sup>.

### 3.3 The final trap

Details of the cooling process outlined in the previous section are standard in our laboratory, but from here what we do with the gas is decided by the measurement we wish to carry out. After evaporation is complete, the atoms are usually loaded into a secondary ODT which is tailored to suit the needs of the measurement. Bragg spectroscopy is no exception to this and the main requirements for the experiments we present here are that the trap is harmonic and it provides an optically thin cloud along the main imaging axis (imaging discussed later in section 3.4). To achieve this we use another red-detuned ODT (1064 nm) and its optical setup is shown in figure 3.5.

Coming from the fibre laser, the beam travels through an acousto-optic modulator (AOM) to allow a computer to control the power in the 1st order beam with high precision, meaning that we can slowly ramp on the laser when it comes time to load the atoms into the trap. We usually use a 200 ms ramp time for this laser. Afterwards, the beam is focussed with a 30 mm achromatic lens through a  $50 \mu\text{m}$  pinhole in order to spatially filter the high spatial frequency components in the beam that come from the AOM. This ensures that the beam has a nice Gaussian profile and at the centre it is approximately parabolic. A 50 mm achromatic lens then collimates the beam again and mirrors are used to guide it to the final 100 mm cylindrical lens, which focusses the beam in only the  $y$ -direction (see figure 3.5). The final lens is specifically placed so its focus overlaps the trap centre as shown in figure 3.6, and we have measured beam waist radii of  $W_x = 511 \mu\text{m}$  and  $W_y = 69 \mu\text{m}$ .

The power of the laser at the trap centre is usually 950 mW, which was decided on by measuring the peak optical density of the trapped atom cloud versus trap power, in

---

<sup>1</sup>For more specific details of the apparatus (optics setups, etc.), refer to [123].

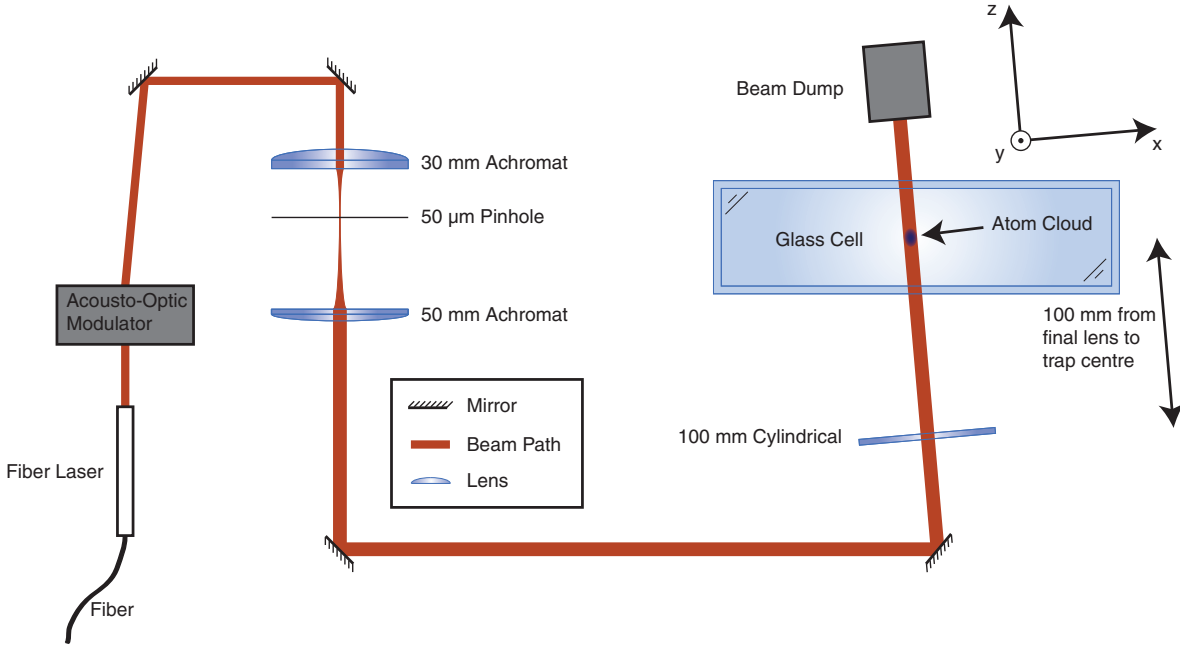


Figure 3.5: A not to scale view of the optical setup for the secondary optical dipole trap. This view is from the top.

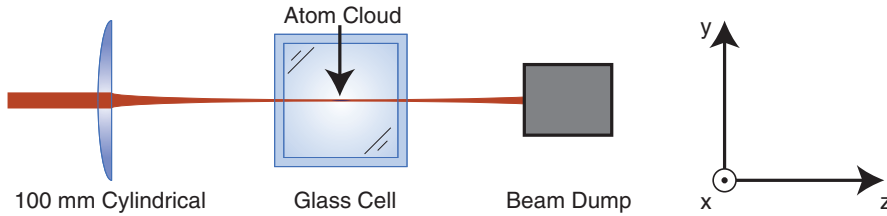


Figure 3.6: A view from the side starting from the final cylindrical lens shown in figure 3.5. The legend shown in figure 3.5 also applies here. From this view we can see the cylindrical lens focussing the beam.

which 950 mW gave the lowest peak optical density. For this power, the trap frequencies are measured to be

$$\omega_x/2\pi = 36.38 \pm 0.06 \text{ Hz} \quad \omega_y/2\pi = 250.30 \pm 1.47 \text{ Hz} \quad \omega_z/2\pi = 24.48 \pm 0.03 \text{ Hz}, \quad (3.4)$$

where the magnetic field strength is 833 G, corresponding to the centre of the Feshbach resonance. Measuring the trap frequencies was achieved by switching on and off a gradient magnetic field (provided by the MOT coils and used as a compensation for the

Feshbach field minimum) for 10 ms. This causes the cloud to start oscillating within the trap at the trap frequency. So measuring the centre of mass of the cloud versus hold time after time of flight expansion reveals these oscillations, and fitting a sinusoid to the measured cloud position yields the trap frequency. These oscillations are shown in figures 3.7, 3.8, and 3.9.

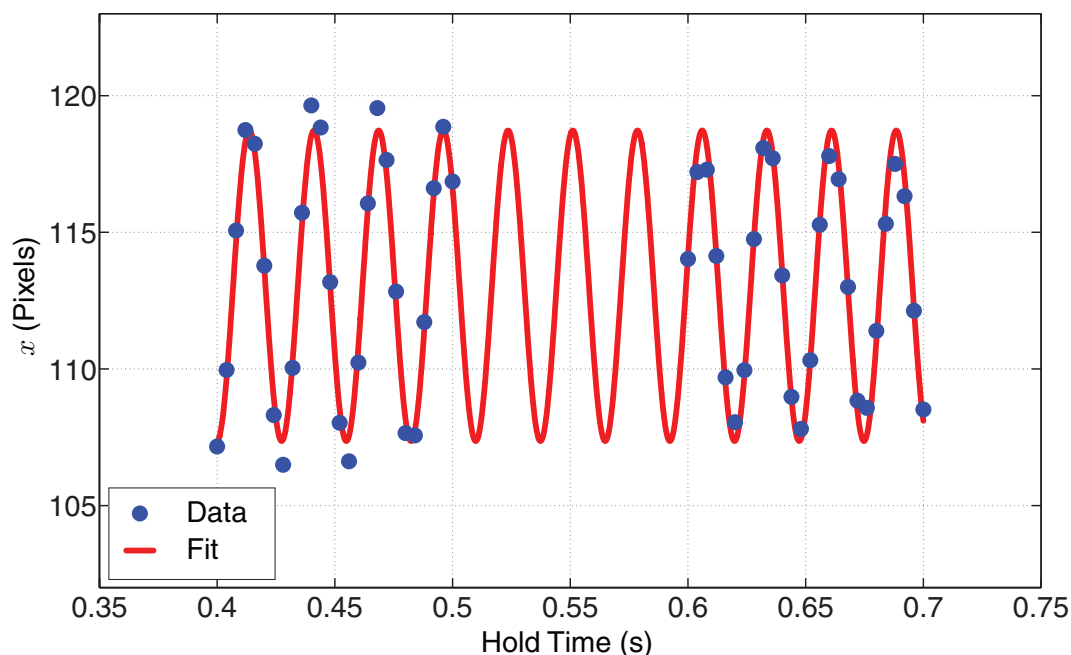


Figure 3.7: Oscillations in the  $x$ -direction,  $\omega_x/2\pi = 36.38 \pm 0.06$  Hz.

Each of the data points in these plots is an average of two shots. From these figures we can see that the amplitude of the oscillations is quite steady after several cycles, indicating that the trap is indeed highly harmonic with minimal damping. With a properly characterised trap, the gas is ready to be probed.

### 3.4 Absorption imaging

The most conventional way to obtain information about ultracold neutral atoms is through optical imaging techniques and in our experiment we use absorption imaging. This section will give an overview of the imaging system we use, but for in-depth

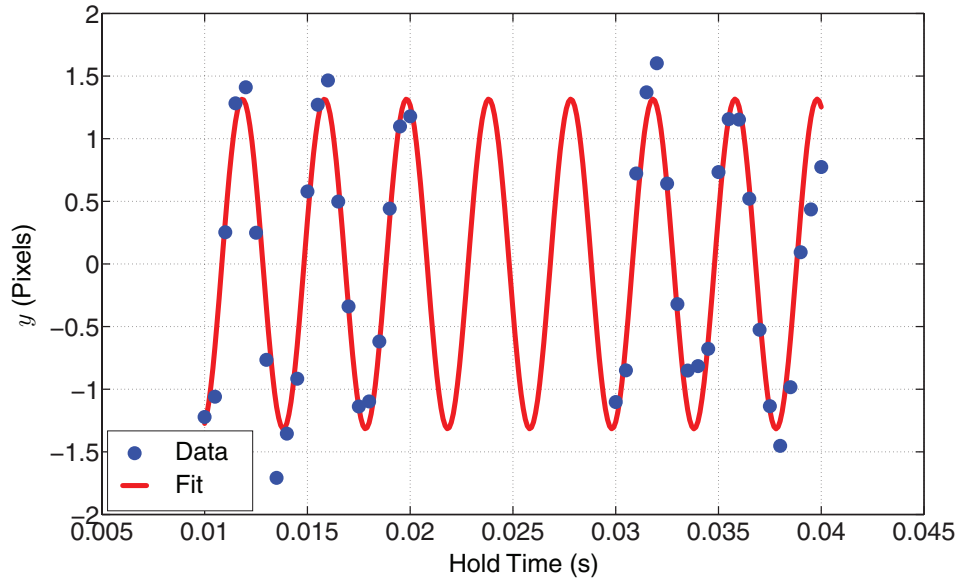


Figure 3.8: Oscillations in the  $y$ -direction,  $\omega_y/2\pi = 250.30 \pm 1.47$  Hz.

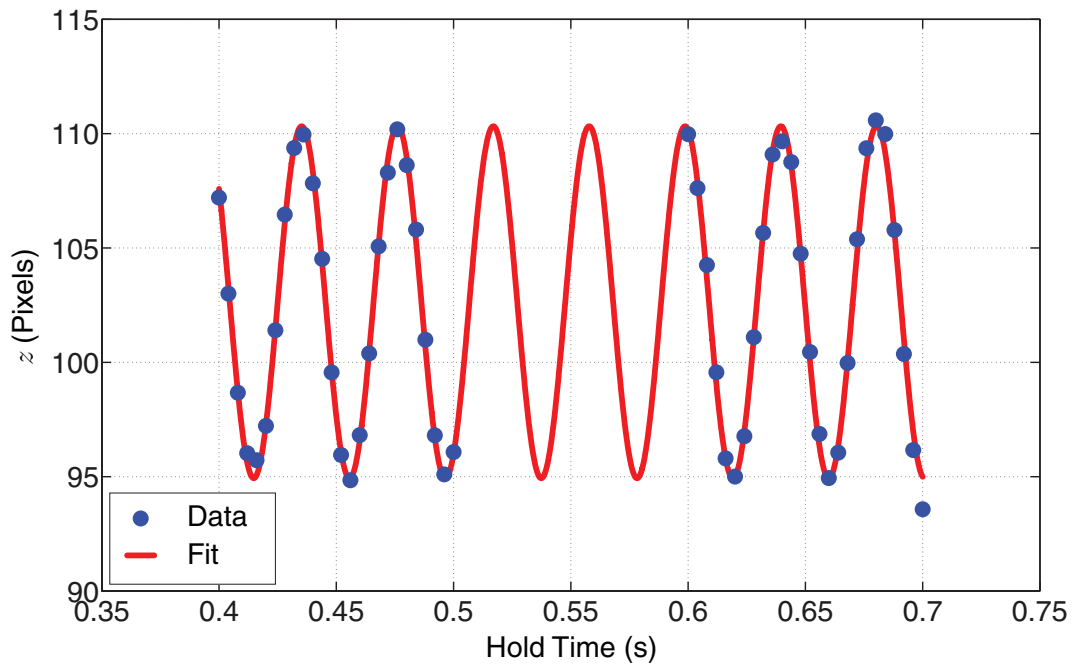


Figure 3.9: Oscillations in the  $z$ -direction,  $\omega_z/2\pi = 24.48 \pm 0.03$  Hz.

technical details of our imaging layout, refer to [123]. The basic setup for absorption imaging involves a laser beam which we call the imaging beam, which is resonant with one of the spin states and propagates along the imaging axis, which is the  $y$ -direction in our experiment. It then travels through the trap centre and a CCD camera is situated on the opposite side of the cloud with respect to the source of the imaging beam. When an individual photon travels through the cloud, it may scatter off an atom and in the event of this happening it is highly likely to scatter away from the propagation axis and thus will not be captured on the CCD. Looking at this scenario from the perspective of many photons interacting with many atoms, the cloud effectively attenuates the imaging beam and areas of the cloud that have a higher column density will cause a larger loss in the beam. This is expressed through Beer's law [127]

$$\frac{dI}{dy} = -n_\sigma \frac{\sigma_0}{1 + I/I_{\text{sat}}} I, \quad (3.5)$$

where  $n_\sigma$  is the atomic density for one spin state,  $I_{\text{sat}}$  is the saturation intensity, and  $\sigma_0 = 3\lambda^2/2\pi$  is the resonant absorption cross-section for a two level atom. The subscript,  $\sigma$  is used here in the density term to specify that the measured density from these images is for one spin state. This is because at high magnetic fields, the imaging beam is resonant with only one of the spin states and the imaging transitions are basically closed two-level systems [128], so in a 50-50 spin mixture this method reveals half of the atoms (i.e.  $n = 2n_\sigma$ ).  $I_{\text{sat}}$  for the CCD used in these experiments has been carefully calibrated [123] and 2.54 mW/cm<sup>2</sup> corresponds to 135 counts/pixel for a 1  $\mu$ s pulse duration. To extract the column density, several images are taken and used to make up a shot. These include:  $I_w(x, z)$  which represents an image of the beam that has passed through the atom cloud, or the beam intensity “with atoms;”  $I_{\text{wo}}(x, z)$  which is an image of the beam unperturbed by an atom cloud, or the beam intensity “without atoms;” and lastly  $I_{\text{dark}}(x, z)$  which is an image taken by the CCD with no imaging beam, or the “dark shot.” We then obtain  $I_a = I_w - I_{\text{dark}}$  and  $I_b = I_{\text{wo}} - I_{\text{dark}}$  and use these as the intensity limits after rearranging equation 3.5 into separate variables and integrating both sides. An image of the three-dimensional cloud can only reveal the

two-dimensional column density,  $\tilde{n}_{2\text{D},\sigma}(x, z) = \int n_{\sigma}(x, y, z)dy$ , which is given as

$$\tilde{n}_{2\text{D},\sigma}(x, z) = \frac{1}{\sigma_0} \left[ -\ln \left( \frac{I_a}{I_b} \right) + \frac{I_b - I_a}{I_{\text{sat}}} \right]. \quad (3.6)$$

The second term in equation 3.6 becomes important when imaging using high intensity probes. In these experiments, the atoms are imaged at large magnetic fields with large Zeeman splitting which means that it is straightforward to choose a laser polarisation and frequency such that only the  $\sigma^-$  transition takes place. As it is impossible to produce perfectly polarised light, an extra parameter,  $\phi$  (measured to be  $\approx 0.93$  in our case), is introduced into equation 3.6 to account for the extra counts that occur on the CCD due to photons of other polarisations within the imaging beam [128]. On top of this, a convenient way to decrease photon shot noise is to use a higher intensity probe while imaging  $I_{\text{wo}}(x, z)$ . In order to account for this, a scaling factor  $\beta$  ( $\approx 0.6$  typically) is also introduced into equation 3.6 to give

$$\tilde{n}_{2\text{D},\sigma}(x, z) = \frac{1}{\sigma_0} \left[ -\ln \left( \frac{I_a/\beta + (\phi - 1) I_b}{\phi I_b} \right) + \frac{\beta I_b - I_a}{I_{\text{sat}}} \right]. \quad (3.7)$$

From here the atom number,  $N_{\sigma}$ , for one spin state can be calculated by integrating over the two remaining directions:

$$N_{\sigma} = \int \tilde{n}_{2\text{D},\sigma}(x, z) dx dz. \quad (3.8)$$

It should be noted that this method of imaging is destructive as the resonant beam drastically heats up the cloud. Therefore only one *in situ* or low time of flight image can be taken per experimental cycle. In our experiment, after taking the first shot of the atoms in state  $|1\rangle$ , we can quickly ramp the frequency of the imaging probe so it is resonant with the other spin state and use the fast kinetics mode of the CCD to take a secondary shot of the atoms in state  $|2\rangle$  after another  $850 \mu\text{s}$ . While the interacting cloud will have heated dramatically by that point, we can still obtain some useful information from state  $|2\rangle$ .

### 3.5 Determining the homogeneous density

The previous section touched on the fact that the absorption imaging reveals a two-dimensional projection of a three-dimensional cloud which that  $\tilde{n}_{2D}(x, z)$  is the integration of true atomic density,  $n$ , along the direction of the imaging axis or line of sight,  $y$ . As explained later in this chapter, the local density approximation is used meaning that infinitesimal volumes of the cloud are considered homogeneous, therefore  $n$  is also referred to as the homogeneous density in this thesis. This is given as

$$\tilde{n}_{2D}(x, z) = \int n(x, y, z) dy. \quad (3.9)$$

For reasons explained later, it is also convenient to define the one-dimensional column density,  $\tilde{n}_{1D}(z)$  for the upcoming calculations which is the integral of the three-dimensional density over the imaging axis,  $y$ , and the  $x$ -direction:

$$\tilde{n}_{1D}(z) = \int n(x, y, z) dx dy. \quad (3.10)$$

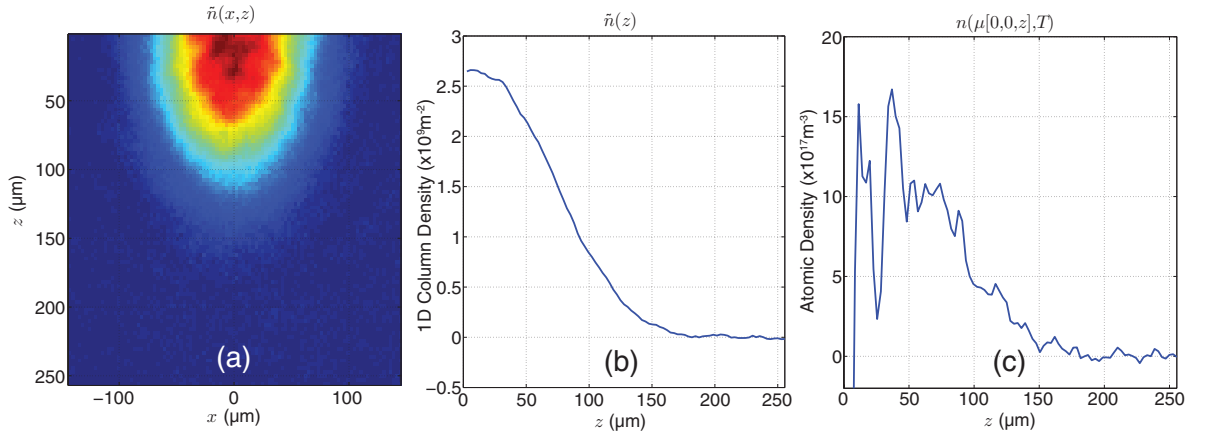


Figure 3.10: Extracting the homogeneous density from the one-dimensional column density. (a) Absorption image folded into a half cloud. (b) One dimensional column density of (a) found using equation 3.10. (c) Homogeneous density obtained by using equation 3.16 on (b).

Figure 3.10 shows this operation being performed to get  $\tilde{n}_{1D}(z)$  shown in figure 3.10(b),

from half of a cloud shown in figure 3.10(a). In general  $n(x, y, z)$  is an important parameter to be able to measure because infinitesimal volumes of the cloud can be described as homogeneous, thus enabling a smoother comparison between experiment and theory. For an inhomogeneous Fermi gas, the local Fermi energy,  $\epsilon_F$  is dependent on the homogeneous density as shown in subsection 2.5.3:

$$\epsilon_F(x, y, z) = \frac{\hbar^2}{2m} (3\pi^2 n(x, y, z))^{2/3}. \quad (3.11)$$

The atomic density becomes even more important in the strongly interacting Fermi gas because it sets the only relevant length scale in the system. This opens the door for experimentalists to perform measurements such as thermometry from *in situ* images of clouds to measure the temperature of the gas in a harmonic trap from an existing equation of state [72, 78, 80, 83, 84, 129, 130]. In this way, features like phase transitions can be detected when the temperature,  $T$ , is a certain fraction of the local Fermi temperature  $T_F(x, y, z) = \epsilon_F(x, y, z)/k_B$ .

There are a couple of methods we can use to find the homogeneous density. It is sufficient to calculate it along one axis that runs through the centre of the harmonic trap (e.g.  $z$ ) as we make sure the cloud has reached equilibrium before taking the image *in situ* meaning that the density throughout the cloud should be the same for a certain value of the trapping potential,  $V$ , regardless of the coordinates. Because the potential provided by the residual magnetic field curvature is extremely harmonic, the line of the trap we measure the homogeneous density along is  $z$ , so we measure  $n(0, 0, z)$  (this is not to say that the optical trapping field is full of imperfections, figures 3.7 and 3.8, show that it is indeed very harmonic). In 2010, a scheme was proposed to extract the homogeneous density from the doubly-integrated line density,  $\tilde{n}_{1D}(z)$  [82]. This method takes advantage of the local density approximation where the chemical potential can be expressed as  $\mu(\mathbf{r}) = \mu_0 - V(\mathbf{r})$ . For a harmonic trapping potential

$$\mu(x, y, z) = \mu_0 - \frac{1}{2}m(\omega_x^2 x^2 + \omega_y^2 y^2 + \omega_z^2 z^2), \quad (3.12)$$

where  $\mu_0$  is the chemical potential in the centre of the cloud. Setting  $x' = \omega_x x$  and

$y' = \omega_y y$ , we substitute  $r'^2 = x'^2 + y'^2$  into equation 3.12 to get

$$dr' = -\frac{d\mu}{mr'}. \quad (3.13)$$

Combining equation 3.13 with  $dx'dy' = 2\pi r'dr'$ , we get  $dx'dy' = -2\pi\mu/m$  which therefore allows us to express an integral over the two radial directions as an integral over the chemical potential:

$$dxdy = -(2\pi/m\omega_x\omega_y)d\mu. \quad (3.14)$$

Now equation 3.14 can be substituted into equation 3.10 and applying the Gibbs-Duhem equation for the pressure  $P = \int n d\mu$ , where  $T$  is constant, the homogeneous pressure along  $z$  turns out to be directly proportional to  $\tilde{n}_{1D}(z)$ :

$$P(\mu[0, 0, z], T) = \frac{m\omega_x\omega_y}{2\pi}\tilde{n}_{1D}(z). \quad (3.15)$$

The experimental group at ENS used this exact conversion in equation 3.15 to measure the equation of state for both a unitary Fermi gas [83], and a Fermi gas with varying interaction strengths [72]. Because  $P$  is a homogeneous quantity, it can be expressed as a function of  $\mu$  and  $T$ . The same goes for the homogeneous density. Using the Gibbs-Duhem equation again in equation 3.15, the homogeneous density can be extracted from the line density with the following:

$$n(\mu[0, 0, z], T) = -\frac{\omega_x\omega_y}{2\pi\omega_z^2}\frac{d\tilde{n}_{1D}(z)}{zdz}. \quad (3.16)$$

Figure 3.10(c) shows the homogeneous density that is calculated from figure 3.10(b) using equation 3.16. This ability to determine homogeneous quantities from integrated profiles is relevant to the work shown in chapter 5. We can see that figure 3.10(c) is noisy which can be attributed to the one-dimensional derivative used to calculate it. This noise makes it difficult to apply it in our thermometry measurements. Thankfully, there is a second, less noisy method of getting  $n(\mu[0, 0, z], T)$ . The true atomic density can be extracted through the use of the inverse Abel transform so long as the *in situ*

cloud has elliptical symmetry. This operation is given as

$$n(r, z) = -\frac{\omega_y}{\omega_x} \frac{1}{\pi} \int_r^\infty \frac{1}{\sqrt{x^2 - r^2}} \frac{d\tilde{n}(x, z)}{dx} dx. \quad (3.17)$$

An example of the application of the inverse Abel transform is shown in figure 3.11, where figure 3.11(a) has had equation 3.17 applied to it to give figure 3.11(b). Averaging figure 3.11(b) along equipotential lines gives the homogeneous density along the line of the harmonic potential shown in figure 3.11(c).

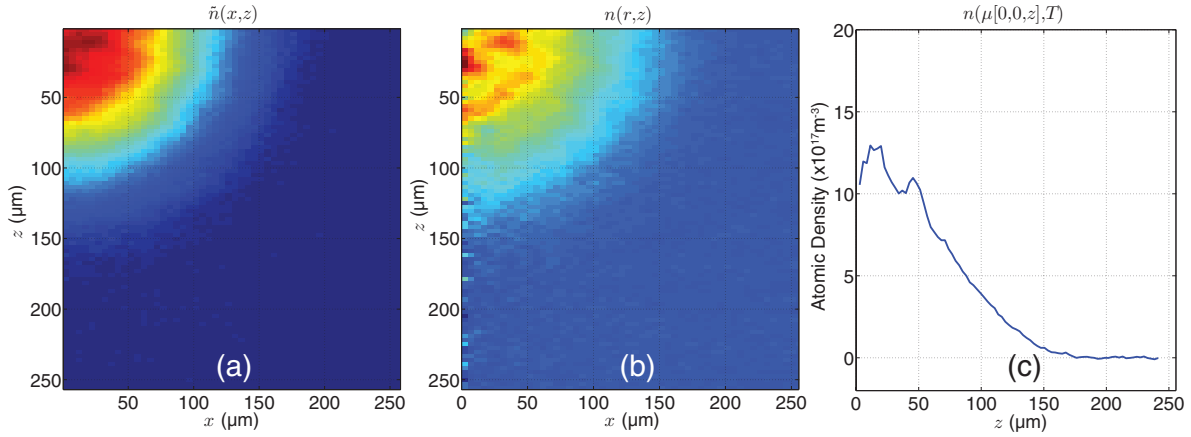


Figure 3.11: Carrying out an inverse Abel transform on an optical density image. (a) Absorption image folded into a quarter cloud. (b) Inverse Abel transform of (a). (c) Homogeneous density profile obtained by averaging (b) along equipotential lines of the harmonic trap.

The noise that shows up towards the centre of the cloud in figure 3.11(c) is due to the derivative in equation 3.17 as well as there being less pixels to include in the average along the equipotential line. However, the noise is far less than that of figure 3.10(c) as the inverse Abel transform allows for elliptical averaging to obtain the one-dimensional profile, as opposed to just integrating across the cloud. A way to self-consistently check if this operation has been carried out correctly is to use equation 3.16 on the homogeneous density to find  $\tilde{n}_{1D}(z)$  again and compare it to what was obtained from equation 3.10. Having calculated  $n(\mu[0, 0, z], T)$ , we now have access to the local Fermi energy and local Fermi temperature.

It should be noted from now onwards that there are two types of measurements

that are carried out in this thesis. The results in chapter 5, are local measurements, thus the local Fermi energy is  $\epsilon_F$  and is given by equation 3.11. The local Fermi temperature is denoted as  $T_F$  and Fermi wavevector  $k_F$ . In chapter 6 the main results are trap-averaged measurements (but we also investigate the local contact). Therefore the harmonic oscillator approach given in equation 2.7 gives the trap-averaged Fermi energy  $E_F^{\text{HO}}$ , where the superscript ‘‘HO’’ stands for ‘‘harmonic oscillator.’’ Therefore it follows on that the trap-averaged Fermi temperature is denoted  $T_F^{\text{HO}}$ , and the Fermi wavevector  $k_F^{\text{HO}}$ .

### 3.6 Thermometry

This section will explain how we measure the absolute temperature of a cloud in nanoKelvin and hence access local relative temperatures. The general idea is to fit the profiles obtained in the previous section to pre-existing equations of state for the unitary Fermi gas. At high local temperatures, a reliable theory used for fitting to data from the laboratory is the 3rd order virial expansion, already alluded to in section 2.5.3. At high temperature, the fugacity,  $Z = e^{\beta\mu}$ , is a small parameter which one can use in an expansion for the density equation of state, which is the said virial expansion. The density using this virial expansion is

$$n\lambda_{DB}^3 = e^{\beta\mu} + 2b_2e^{2\beta\mu} + 3b_3e^{3\beta\mu} + \dots, \quad (3.18)$$

where  $\beta = 1/k_B T$  and  $\lambda_{DB}$  is the thermal de Broglie wavelength. The virial coefficients are  $b_2 = 3\sqrt{2}/8$  [77] and  $b_3 = -0.29095295$  [78]. The virial expansion works well for all  $\beta\mu < -0.85$  [84].

Several methods have been used for obtaining the equation of state for a three-dimensional unitary Fermi gas. One method utilised at ENS involved the use of a Bose gas mixed in with the unitary Fermi gas which could be used as an external thermometer [83].

Another method involved fitting the high temperature wings of the cloud with the virial expansion to extract the equation of state for a gas in the normal phase [84]. These results were then compared to a theoretical simulation which utilised the

bold diagrammatic Monte Carlo method (BDMC). As the BDMC data is found in a way that is more likely to be free from systematics, it is generally regarded as one of the most reliable approaches for describing a unitary Fermi gas and was also found to agree very well with the experimental results. The other experimental measurement, at MIT, utilised scale invariance at unitarity to extract thermodynamic quantities such as density, pressure, and compressibility for high temperature clouds using a model independent analysis of the data based on the local density approximation. They then interpolated from the higher temperature data down to lower temperature regions, reaching as far down as below the superfluid transition [80]. At the time we performed the measurements in chapter 5 we only had access to the BDMC data but in this section, there will also be comparisons between our data and the MIT equation of state.

In the previous section it was outlined how to extract the homogeneous pressure,  $P(\mu, T)$  (equation 3.15). Fitting our data to the equation of state data, we can obtain the temperature,  $T$ , in Kelvin as well as the chemical potential in the centre of the cloud  $\mu_0$ . This is achieved by feeding  $P(\mu, T)$  versus  $z$  into the fitting function. It then converts  $z$  to  $\beta\mu$ , and the pressure to

$$F_P(\beta\mu) \equiv \frac{\lambda_{DB}^3}{k_B T} P(\mu, T), \quad (3.19)$$

where  $F_P(\beta\mu)$  is a universal function describing the dimensionless pressure. The fitting function proceeds to find the best values for  $T$  and  $\mu_0$  so that our data matches the BDMC data. An example of this type of fit is shown in figure 3.13.

The residual error in the absolute temperature from the fitting procedure is dependent on what percentage of the cloud could be fitted to the equation of state. For cold clouds this error is as high as 4%, however at higher temperatures where the equation of state can fit to the entire cloud the residual error is only around 2%. It should be noted that this error in the temperature does not take into account any possible errors in the equation of state itself. Upon extracting the absolute temperature and central chemical potential we have access to the local temperature,  $T/T_F$ , and local chemical potential over the Fermi energy,  $\mu/\epsilon_F$ , via our knowledge of the density. This method can also be checked self-consistently by comparing our measured  $T/T_F$  and  $\mu/\epsilon_F$  using our measured homogeneous density profile, with the data from the equation of state

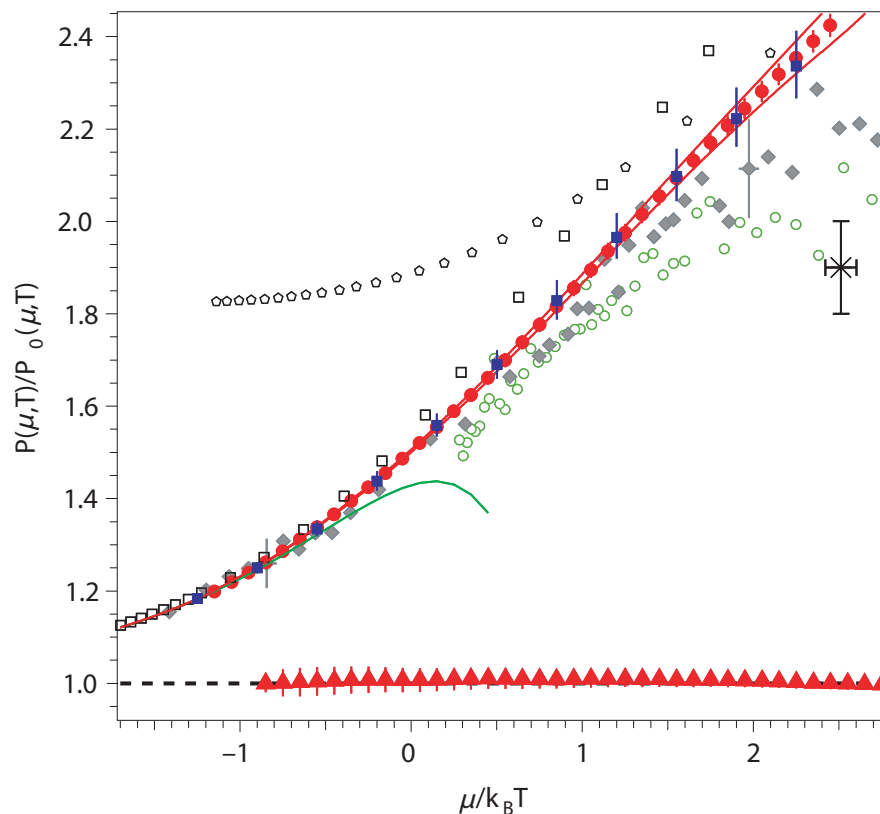


Figure 3.12: Pressure equation of state taken from [84]. The blue filled squares are the bold diagrammatic Monte Carlo calculation and the red filled circles are experimental data. The black dashed line and red triangles are theory and experimental data for the ideal Fermi gas. The green solid line is the 3rd order virial expansion. Various results from other simulations are shown- Empty squares: [131, 132], green empty circles: [133], star: [134]. Other experimental results - grey diamonds: [83], empty pentagons: [135]. Reprinted by permission from Macmillan Publishers Ltd: *Nature Physics*, advanced online publication, (28 09 2015). (doi: 10.1038/nphys2273).

[80].

### 3.7 Atom number calibration

The absorption imaging scheme that was reviewed in section 3.4 outlines how to extract the column density of an atom cloud from several different images taken in succession. As mentioned in section 3.3, the final optical dipole trap is specifically designed to reduce

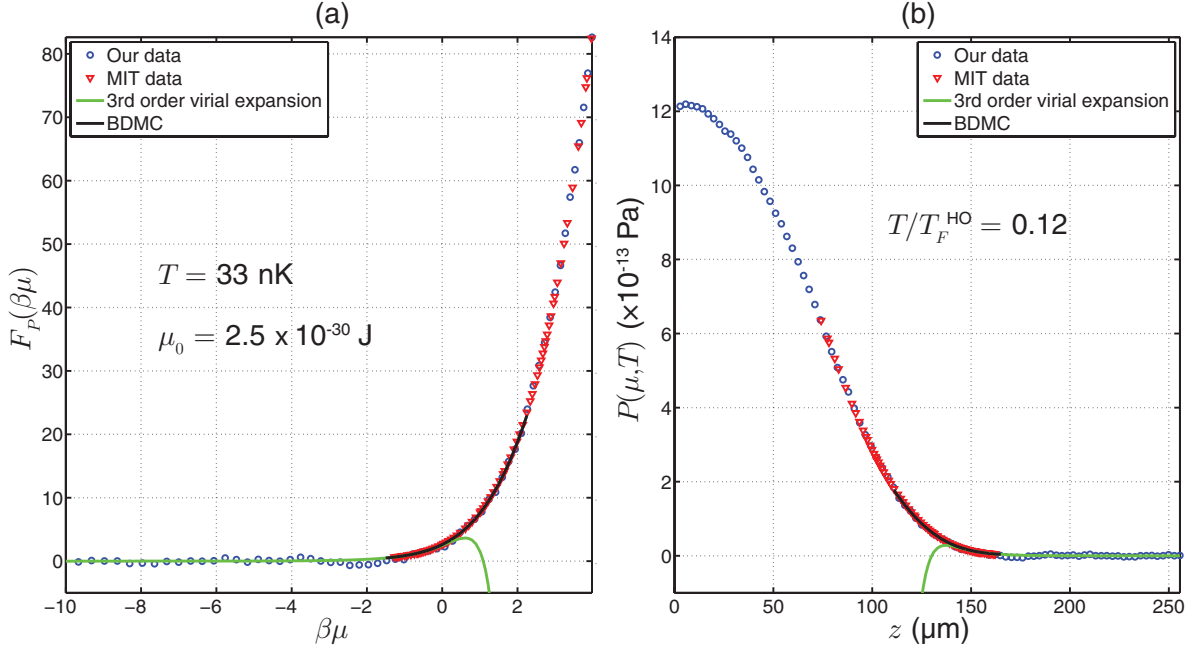


Figure 3.13: Data fitted to the pressure equation of state. (a) Fit to the pressure thermodynamic function  $F_P(\beta\mu)$ . Only the wings of the cloud, where  $T/T_F(z)$  is higher, can be fitted to the equation of state. (b) The data from (a) converted back to pressure using equation 3.19 except the pressure from the whole cloud is shown. As shown in (b), only the wings of the cloud can be fitted with the current equation of state.

the optical thickness along the  $y$ -direction. The reason being that it is particularly hard for the photons to penetrate the cloud, especially with a low power imaging probe (which tends to be more desirable to use in order to reduce the background noise), as well as reducing the chance of multiple scattering events occurring in volumes of high density. This means that after processing the low intensity images, we do not “see” all of the atoms and therefore the processed images generally underestimate the atom number.

This section focusses on finding a correction of the atom number (density) in our current experiments due to these factors, as well as finding the correct atom number for the trap that was used in our precision measurement of Tan’s contact parameter in reference [63]- its final value being  $N_\sigma = (300 \pm 25) \times 10^3$  atoms, where  $N_\sigma$  is the atom number in one spin state. The trap used for this earlier measurement utilised the same 1064 nm laser shown in section 3.3, but the optics setup is slightly different as shown in reference [123], such that it is a cylindrically symmetric trap ( $\omega_x/2\pi = \omega_y/2\pi = 97$  Hz,

and  $\omega_z/2\pi = 24.5$  Hz). The pulse for the imaging beam used in these measurements had a duration of  $1 \mu\text{s}$  and peak intensity of  $I \approx 4I_{\text{sat}}$ . This power for the imaging beam was thought at the time to be sufficient for obtaining a reliable measure of the true atom number for the given pulse duration but it soon became apparent after the new setup (the one outlined in section 3.3) was implemented that the imaging probe used in these measurements still underestimated the atom number. The way we calculated the contact in these measurements is from the structure factor Tan relation given by rearranging equation 2.37

$$\frac{\mathcal{I}}{Nk_F^{\text{HO}}} = \frac{4k}{k_F^{\text{HO}}} \left[ \frac{S_{\uparrow\downarrow}(k)}{1 - 4/(\pi ka)} \right], \quad (3.20)$$

where  $k_F^{\text{HO}} = (2m\bar{\omega}/\hbar)^{1/2}(6N_\sigma)^{1/6}$  is the trap-averaged Fermi wavevector and is the parameter where the contact has its atom number dependence. As this measurement of the contact was intended to be a precision measurement, it is important that all of the experimental parameters that go into this equation are known to a high degree of accuracy- including, for the purposes of this section, the atom number. The contact has a 1/6-power law dependence on the atom number, so it is one of the few parameters that can afford to have a considerable error, as a 10% error in the atom number corresponds to only roughly a 1.7% error in the contact.

As the ODT used to obtain the original Bragg data had since been modified, we used the evaporation ODT to gain the critical information we required to infer the atom number. The first step was to find a scaling factor that is dependent on the peak optical density with the given probe beam ( $I \approx 4I_{\text{sat}}$  and  $1 \mu\text{s}$  pulse duration). Firstly, the trap was evaporated down to a similar end point that was used in the precision contact measurement which is 760 nK, and then ramped up to 2500 nK by adiabatically compressing the trap so the expansion of the cloud that follows would occur more rapidly. The cloud was then released and shots are taken after various time of flights. The further the cloud expands, the more dilute it becomes and therefore more atoms are revealed as shown in figure 3.14.

As the time of flight reaches around 3-4 ms, figure 3.14 shows that the atom number comes close to plateauing. Increasing the time of flight also corresponds to a decreasing peak optical density as shown in figure 3.15.

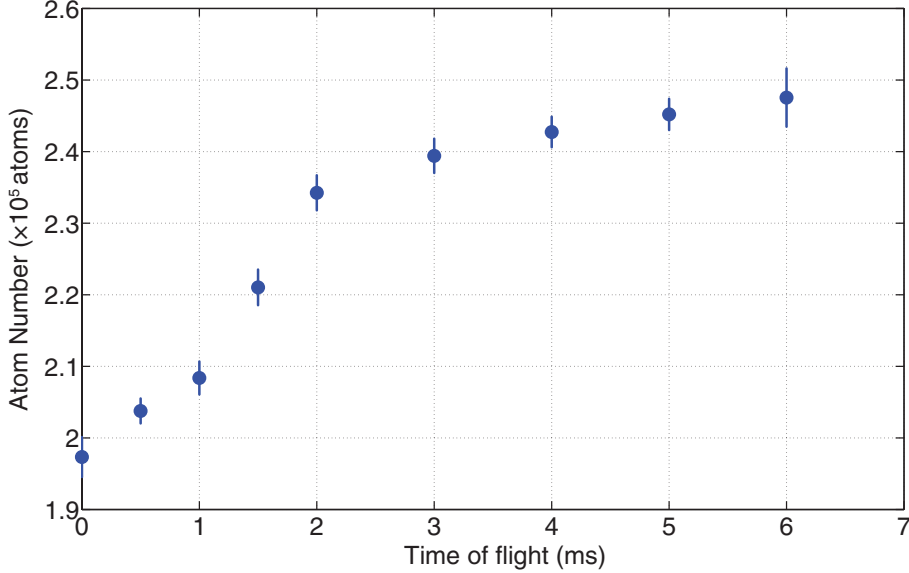


Figure 3.14: Number of atoms that the imaging scheme measures versus time of flight of the same cloud. The trap-depth at the end of evaporation is 760 nK, the imaging beam intensity is  $4I_{\text{sat}}$ , and the pulse duration is  $1 \mu\text{s}$ .

This same procedure was repeated for a trap evaporation end point of 310 nK (before ramping up to 2500 nK again) in order to vary the conditions and obtain universal scaling factor for this  $4I_{\text{sat}}$  image probe. Each atom number data point in each data set is now normalised by the measured atom number for the most dilute cloud in the set. This is shown in figure 3.16 where the green data set is for a 310 nK trap-depth and the blue is for the 760 nK trap-depth data shown before in figure 3.14. The 310 nK data has already plateaued.

From what is outlined so far, the normalised atom number for the 760 nK data at 6 ms time of flight should be exactly unity; however they fall just shy in figure 3.16. The reason for this comes from looking at the peak optical densities. The peak optical density for the 760 nK cloud at 6 ms time of flight is  $\sim 1.5$  (as shown in figure 3.15). This peak optical density is close to the peak optical density of the 310 nK cloud after 1 ms time of flight. It is also clear that the atom number in figure 3.14 has not yet plateaued by 6 ms. So, therefore, the normalised atom numbers in the 760 nK data set have been scaled additionally by the normalised atom number of the 310 nK data set at

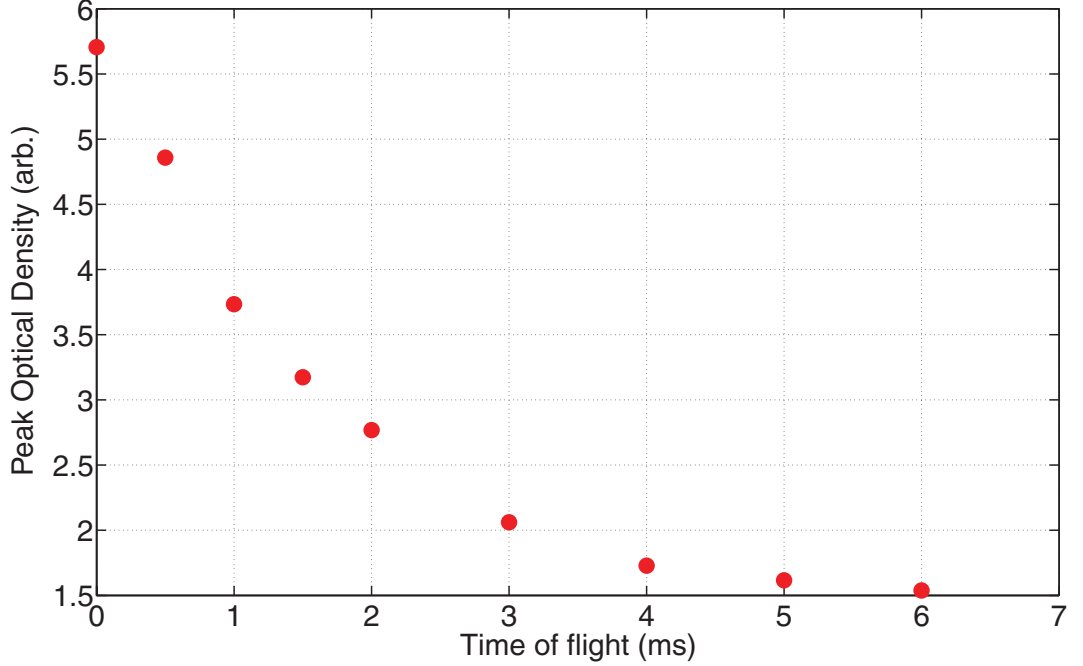


Figure 3.15: Peak optical density versus time of flight of the same cloud. The peak optical density is measured by taking the mean of a  $4 \times 4$  pixel area on the images in the region where the density is the highest. The trap-depth at the end of evaporation is 760 nK, the imaging beam intensity is  $I \approx 4I_{\text{sat}}$ , and the pulse duration is 1  $\mu\text{s}$ .

1 ms. The reason we do this extra normalisation is because we want to plot normalised atom number against peak optical density from both sets on the same curve. The result of this is shown in figure 3.17.

The data points are fitted to a quadratic function

$$NAN_{\text{DILUTE}} = a - bn_{\text{OD}}^2, \quad (3.21)$$

where  $NAN_{\text{DILUTE}}$  stands for normalised atom number in the dilute limit,  $n_{\text{OD}}$  is the peak optical density,  $a$  is the amplitude fitting parameter and  $b$  is the width fitting parameter. Here  $a = 1.002_{-0.009}^{+0.009}$  and  $b = 0.0068_{-0.0006}^{+0.0006}$ . As a result of this analysis, we can now work out a scaling parameter for images with  $n_{\text{OD}} < 6$  for any given image taken under the aforementioned conditions. For this same image, we use equation 3.8 to find the “raw” atom number which can then be divided by the scaling parameter to find the atom number in the dilute limit. The raw images taken for the precision

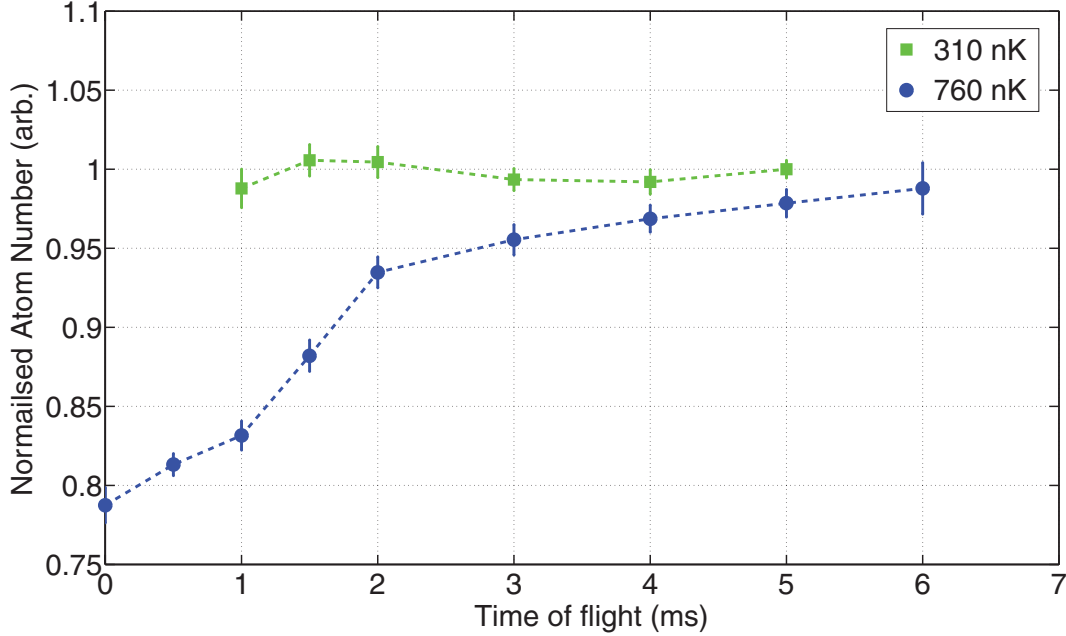


Figure 3.16: Normalised atom number versus time of flight of the same cloud. The green data is for a 310 nK trap-depth and blue data is 760 nK.

contact measurement have a peak optical density of  $n_{\text{OD}} \sim 5.5$  and an atom number that appears to be  $(220 \pm 10) \times 10^3$  from equation 3.8. This peak optical density gives a scaling factor of  $NAN_{\text{DILUTE}} \sim 0.80$  which means the atom number in the dilute limit for a  $4I_{\text{sat}}$  pulse is  $(274 \pm 17) \times 10^3$ , where the new error has taken into account the 95% confidence bounds on the fit.

An additional correction is required to account for the imaging intensity. In doing this, the true *in situ* density is revealed as more photons can penetrate the cloud and scatter off atoms farther along the imaging axis. This time the measurements are made on atoms trapped in the cylindrically asymmetric trap described in section 3.3 so that the gas *in situ* is optically thin. The imaging intensity is varied from  $1I_{\text{sat}}$  to  $20I_{\text{sat}}$  in an attempt to measure how the atom number varies and obtain another scaling factor that allows for a correction due to low imaging intensity. Again, an atom number is obtained for each imaging intensity using equation 3.8, and we notice that it increases against intensity until it plateaus. Each of these atom numbers is divided by the atom number at  $20I_{\text{sat}}$  and plotted in figure 3.18.

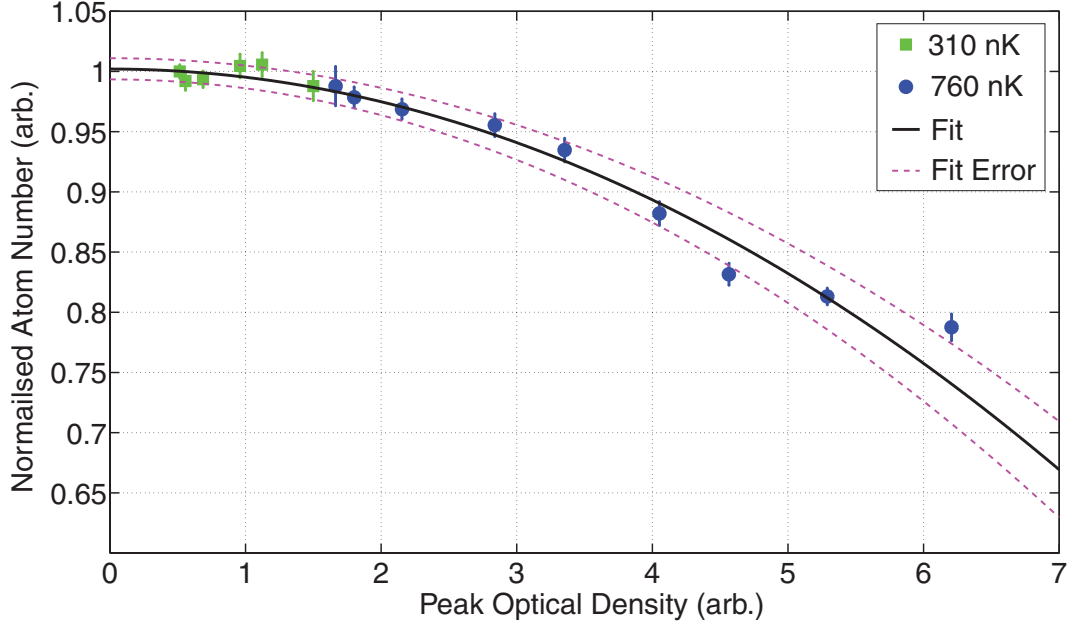


Figure 3.17: Normalised atom number versus peak optical density for both clouds after various times of flight. The green data is for 310 nK trap-depth, the blue data is 760 nK, the black solid line is the fit of the form  $NAN_{\text{DILUTE}} = a - bn_{\text{OD}}^2$ , and the magenta dashed lines are 95% confidence bounds on the fit.

This is fitted to a different function which empirically provides a good fit to the data, given as

$$NAN_{\text{INTENSITY}} = 1 - ce^{-d(I/I_{\text{sat}})}, \quad (3.22)$$

where  $NAN_{\text{INTENSITY}}$  is the normalised atom number for the intensity correction, while  $c$  and  $d$  are the fitting parameters. Here  $c = 0.17_{-0.03}^{+0.03}$  and  $d = 0.25_{-0.07}^{+0.07}$ . This new scaling factor provides another correction to the atom number which is  $NAN_{\text{INTENSITY}} \sim 0.94$  at  $4I_{\text{sat}}$ , that consequently brings the atom number up to  $(292 \pm 21) \times 10^3$  atoms. Again, the error in the atom number has taken into account the 95% confidence bounds on the fit in figure 3.18.

The final correction to the atom number arises from a self-consistency check. As pointed out in section 2.5 the radial cloud width,  $R_i$ , has a dependence on the atom number. Unfortunately at unitarity, there is no simple way to extract  $R_i$  from a fitting function at finite temperature to a cloud profile so in order to carry out this self-consistency check we take high intensity shots at  $20I_{\text{sat}}$  of the density in the weakly

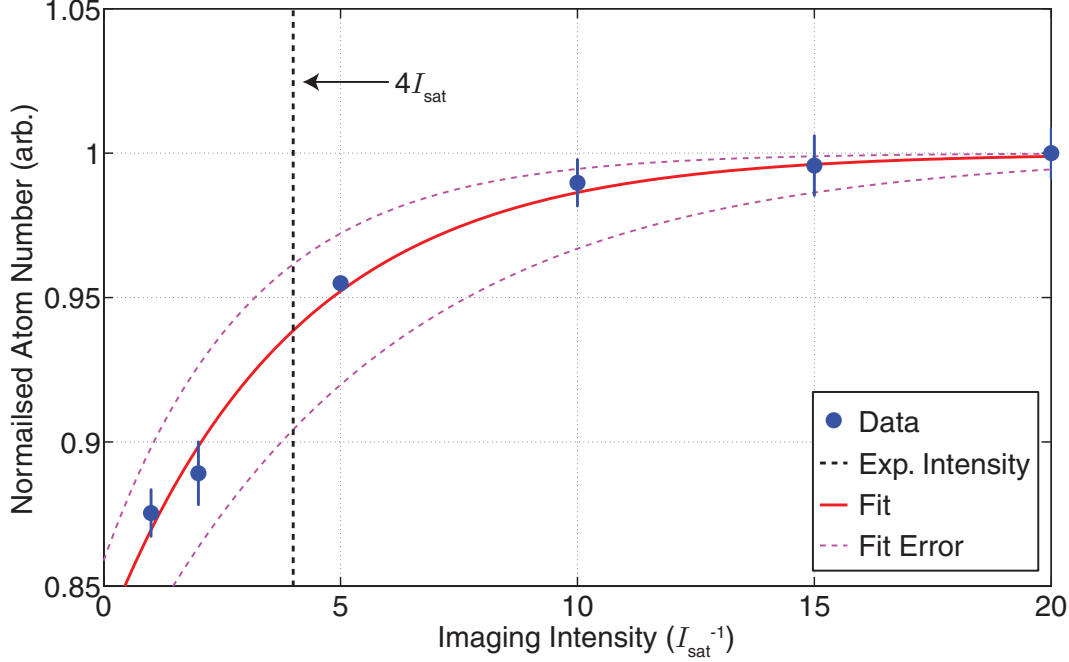


Figure 3.18: Normalised atom number against peak intensity of the imaging probe in units of  $I_{\text{sat}}$ . The blue dots are the data points, the red line is the fitted line to equation 3.22, the vertical black dashed line is the imaging intensity of the experimental data ( $4I_{\text{sat}}$ ) and the magenta dashed lines are the 95% confidence bounds on the fit.

interacting BCS regime. The Feshbach field is set to 976 G, making the scattering length  $a = -4537.7a_0$ , where  $a_0$  is the Bohr radius. The trap frequencies are measured to be  $\omega_x/2\pi = 37.62 \pm 0.06$  Hz,  $\omega_y/2\pi = 250.30 \pm 1.47$  Hz,  $\omega_z/2\pi = 26.33 \pm 0.06$  Hz. The atom number is measured the usual way in these images using equation 3.8 and then the 1D profile is extracted along the  $z$ -direction using equation 3.10 (for one spin state). The profile is then fitted to a polylogarithm function,  $\text{Li}_{5/2}(z)$ , that generally describes a non interacting gas, but in our case the gas is weakly interacting enough to give approximately the correct parameters. The fitting function is

$$\tilde{n}_{1\text{D},\sigma,\text{FIT}}(z) = A \frac{\text{Li}_{5/2} \left( -\exp \left[ \beta\mu - \frac{z^2}{R_z^2} f(e^{\beta\mu}) \right] \right)}{\text{Li}_{5/2}(-e^{\beta\mu})}, \quad (3.23)$$

where  $f(x) = \frac{1+x}{x} \ln(1+x)$  [90]. The fitting parameters are,  $A$ , for the amplitude,  $\beta\mu$ , and the width parameter,  $R_z$ , which we are interested in. The result of fitting the

profile to equation 3.23 is shown in figure 3.19. The Fermi radius,  $R_z$  in pixels comes

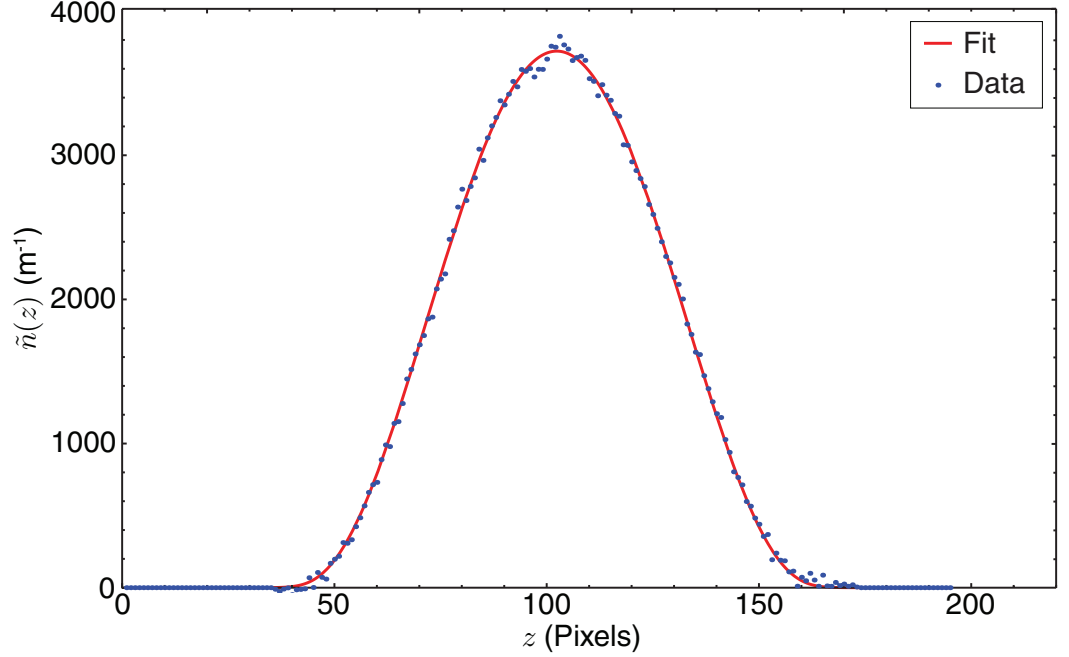


Figure 3.19: 1D column density,  $\tilde{n}_{1D,\sigma}(z)$ , versus  $z$  in pixels for a cloud at 976 G imaged with a  $20I_{\text{sat}}$ ,  $1 \mu\text{s}$  imaging pulse. The data points are the blue dots and are fitted to equation 3.23, which is the red solid line.

out as  $61.30 \pm 0.45$  which in real units is  $R_z = 174.0 \pm 1.3 \mu\text{m}$ . From here the Fermi energy can be extracted through the use of equations 2.24 and 2.25 which are shown here in equation 3.24, as well as  $k_F^{\text{HO}} = \sqrt{(2mE_F^{\text{HO}})/\hbar}$ :

$$R_z = R_{F,z} \left( 1 - \frac{256}{315\pi^2} k_F^{\text{HO}} |a| \right) \quad R_{F,z} = \sqrt{\frac{2E_F^{\text{HO}}}{m\omega_i^2}}. \quad (3.24)$$

Here,  $R_{F,z}$  is the non-interacting Thomas-Fermi radius. Once we know the Fermi energy, we can then use  $E_F^{\text{HO}} = (6N)^{1/3} \hbar\bar{\omega}$  (equation 2.7), to work out the true atom number. Comparing the atom number obtained from the two different methods to one another, we find that the atom number obtained from a double integration of the image needs to be divided by a factor  $NAN_{\text{WIDTH}} = 0.97 \pm 0.03$ . This is the final scaling factor that brings us to the final value  $N_\sigma = (300 \pm 25) \times 10^3$  atoms. Therefore, the Fermi wavevector has an error of less than 1.5% meaning that with a precise determination of

the static structure factor, the contact can be measured to a high degree of accuracy.

For the rest of this thesis, when determining the true atomic density in the new cylindrically asymmetric trap, atoms are imaged with a high intensity probe and the final correction factor of  $1/0.97$ , that arises from the BCS cloud width is applied. As the cloud is already optically thin for the remainder of the measurements presented in this thesis, usually no other correction is needed under these conditions.

### 3.8 Summary

This chapter gives an overview of some of the technical and experimental aspects that relate to this work. First, a reminder of how we achieve degeneracy was briefly covered before delving into the setup for the final optical dipole trap. We chose for the trap to be cylindrically asymmetric in order to reduce the optical thickness of the cloud along the imaging axis, which helps to reduce systematics. The characterisation of the trap was also presented. Extracting the column density via absorption imaging is then covered which leads to calculating the true atomic density from these images, as well as how to measure the temperature of the imaged clouds. From here, there is a detailed overview of how we managed to determine a precise atom number for the results in [63] using different calibration techniques. This chapter, however, did not contain information on the Bragg spectroscopy setup as this is covered in the next chapter.

# Chapter 4

## Bragg spectroscopy and linear response

### 4.1 Introduction

The main results of this thesis are obtained through probing the unitary Fermi gas using Bragg spectroscopy. The aim of this chapter is to explain the key elements of Bragg spectroscopy and lay a foundation for the next two results chapters. This discussion includes the experimental aspects such as the laboratory setup and the methods used to extract the Bragg response from the absorption images and analysing a Bragg spectrum. Probing the density-density response with Bragg scattering yields the imaginary part of the dynamical susceptibility and this is related to the dynamic structure factor, therefore some theoretical background is provided on these topics. The  $f$ -sum rule is also introduced, which allows the static structure factor to be measured with high accuracy.

### 4.2 Bragg spectroscopy

As described in the previous chapter, the  ${}^6\text{Li}$  atoms are cooled in their gaseous form by depleting their kinetic energy through conventional laser cooling and trapping techniques. The atoms are held in an optical dipole trap in a 50-50 mixture of their two

lowest hyperfine states, enabled by the application of a strong magnetic field which tunes the  $s$ -wave interactions to the strongly interacting regime. After the gas has equilibrated, the unitary Fermi gas is ready to be probed. Bragg scattering of atoms from an optical standing wave was first observed in 1988 [136], where the subject was a beam of sodium atoms. Since then, Bragg spectroscopy has been used in other laboratories to probe BEC's [32, 117, 137], and in our laboratory at Swinburne to probe Fermi gases [34]. This section covers our experimental implementation of Bragg spectroscopy as well as the interpretation of the Bragg spectra.

### 4.2.1 Experimental setup

The setup for the Bragg spectroscopy experiments in the Swinburne laboratory have been described in-depth previously in several theses coming from our group [120, 122]. More specifically, the Bragg spectroscopy setup in this thesis is basically the same as described in Sascha Hoinka's thesis [123]. Two-photon Bragg scattering involves exposing the atoms to two laser beams that intersect at an angle, which in our case is  $2\theta = 84^\circ$ . An atom is excited into a virtual state via absorption of a photon from one beam, and then stimulated emission into the other beam returns the atom back to its ground state again. A net two-photon momentum,  $\hbar\mathbf{k}$ , is transferred to the atoms in the direction of the moving interference pattern, in which its speed is governed by the frequency difference between the two Bragg beams,  $\omega = \omega_A - \omega_B$ , which is the Bragg frequency. The Bragg wavevector is given by  $\mathbf{k} = \mathbf{k}_A - \mathbf{k}_B$ , where  $\mathbf{k}_A$  and  $\mathbf{k}_B$  are the wavevectors of the individual Bragg beams. The magnitude of the two-photon momentum,  $k$ , transferred to the atoms is determined by  $\theta$  and the wavelength of the laser beams,  $\lambda_L$ :

$$k = \frac{4\pi}{\lambda_L} \sin \theta. \quad (4.1)$$

Because the angle between the two Bragg beams is large, the momentum transfer is also large (i.e.  $k > k_F$ ), meaning that the probe is sensitive to the scattering of single particles [118] (or see section 2.7 of this thesis). If an atom undergoes this Bragg scattering process, it receives a momentum of  $\hbar\mathbf{k}$ , resulting in a change in kinetic energy. For an atom that was initially at rest, its change in kinetic energy is given as  $\hbar^2 k^2 / 2m$ . If the energy difference between the two Bragg beams,  $\hbar\omega$ , matches this change in

kinetic energy, the atom will scatter resonantly meaning that the atomic resonance,  $\omega_r$ , is given as

$$\omega_r = \frac{\hbar k^2}{2m}. \quad (4.2)$$

If the atom is initially moving at velocity  $\mathbf{v}_i$ , it will then be able to scatter resonantly if the Bragg frequency matches the following:

$$\omega = \omega_r + \mathbf{k} \cdot \mathbf{v}_i. \quad (4.3)$$

This means that the moving interference pattern is Doppler shifted according to the moving atom, and therefore Bragg spectroscopy is a momentum selective process. In a gas of many atoms, Bragg scattering results in a perturbation of the atomic density. The scheme for Bragg scattering is illustrated in figure 4.1.

Figure 4.1(a) shows an *in situ* cloud as well as the angles that the two Bragg beams are directed at the cloud, which are represented by the waveforms. The Bragg beams are collimated with a waist diameter  $\sim 5.3$  mm that is large compared to the size of the atom cloud, so all atoms experience the same intensity. Bragg scattering leads to a momentum kick along the  $x$ -direction resulting in figure 4.1(b), where the cloud has moved with respect to figure 4.1(a). This has been made clearer in figure 4.1(c) and figure 4.1(d) where figure 4.1(c) is the integrated profile over  $z$  of figure 4.1(a) while figure 4.1(d) is the integrated profile of figure 4.1(b). From these two profiles it can be easily seen that there is a change in the centre-of-mass of the cloud due to the Bragg pulse.

In order to measure the density-density response (i.e. the response of the density due to the density perturbation), the frequency detunings and polarisations of the Bragg beams are configured in a specific way. The virtual levels involved in the Bragg process must be approximately the same detuning away from their closest excited state for both ground states. At the same time, access to other excited states must be heavily suppressed. The Bragg transitions are blue detuned from the two resonances in order to avoid molecular photoassociation which can occur at specific red detunings. In these experiments, the detunings we use are  $\Delta_{\uparrow} = 584$  MHz and  $\Delta_{\downarrow} = 662$  MHz. Figure 4.2 shows the relevant transitions.

We are aiming for a virtual excitation with  $\Delta m_J = -1$ , which requires circularly po-

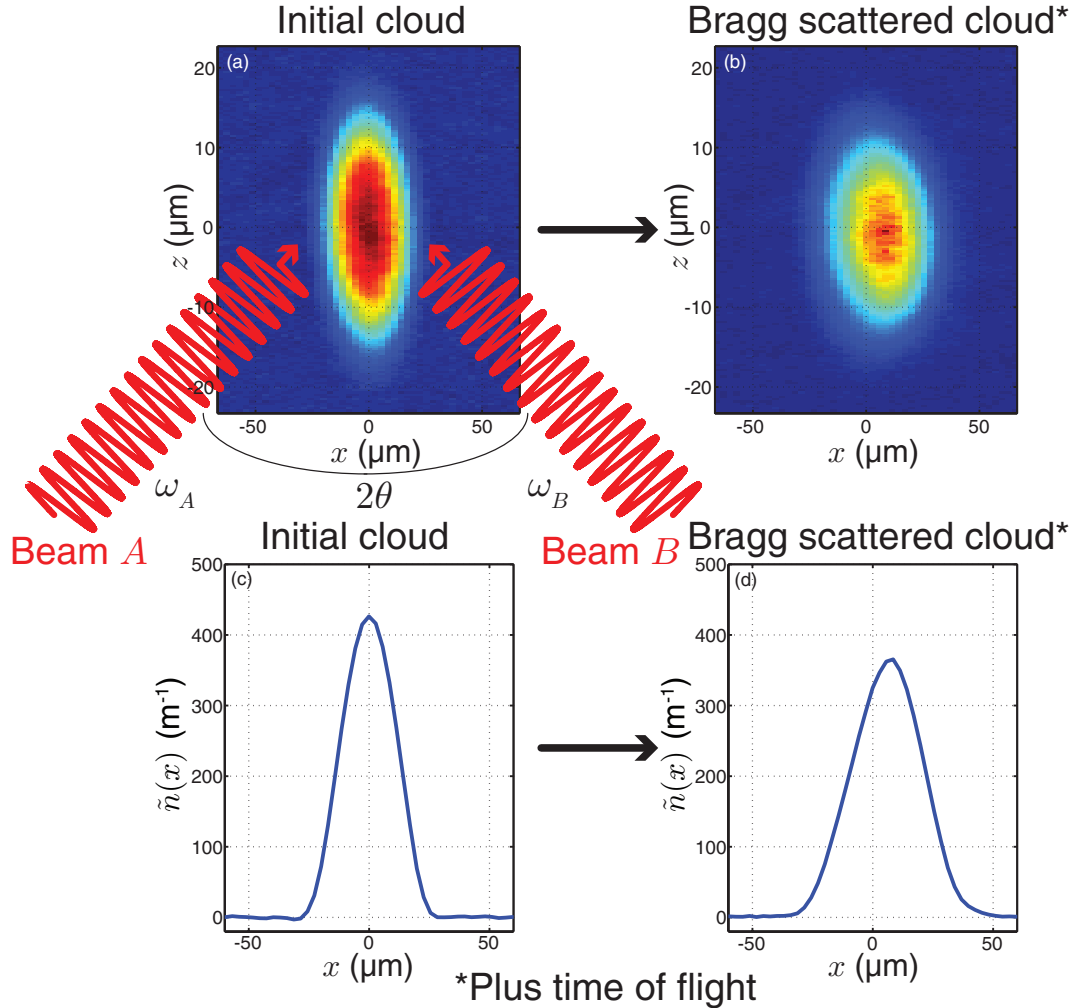


Figure 4.1: The effect of Bragg scattering on an atom cloud. (a) A false colour image of the atom cloud taken *in situ* with no perturbation. The red waveforms show the angles in which the two Bragg beams propagate. In these experiments  $2\theta = 84^\circ$  and the frequency in “beam A” is increased with respect to “beam B” to cause a momentum kick along  $x$  toward the right hand side of the page. (b) False colour image of the cloud after Bragg scattering with a finite  $\omega$  after some time of flight. The cloud has been kicked along the  $x$ -direction due to the Bragg pulse. (c) Integrated profile of the cloud in image (a). (d) Integrated profile of the cloud in image (b).

larised  $\sigma^-$  light. Therefore, the Bragg beams are horizontally polarised (perpendicular to the Feshbach magnetic field) which means that in the intersecting region, a pattern of  $\sigma^+$  and  $\sigma^-$  light alternates periodically in a lattice, as shown in figure 4.3.

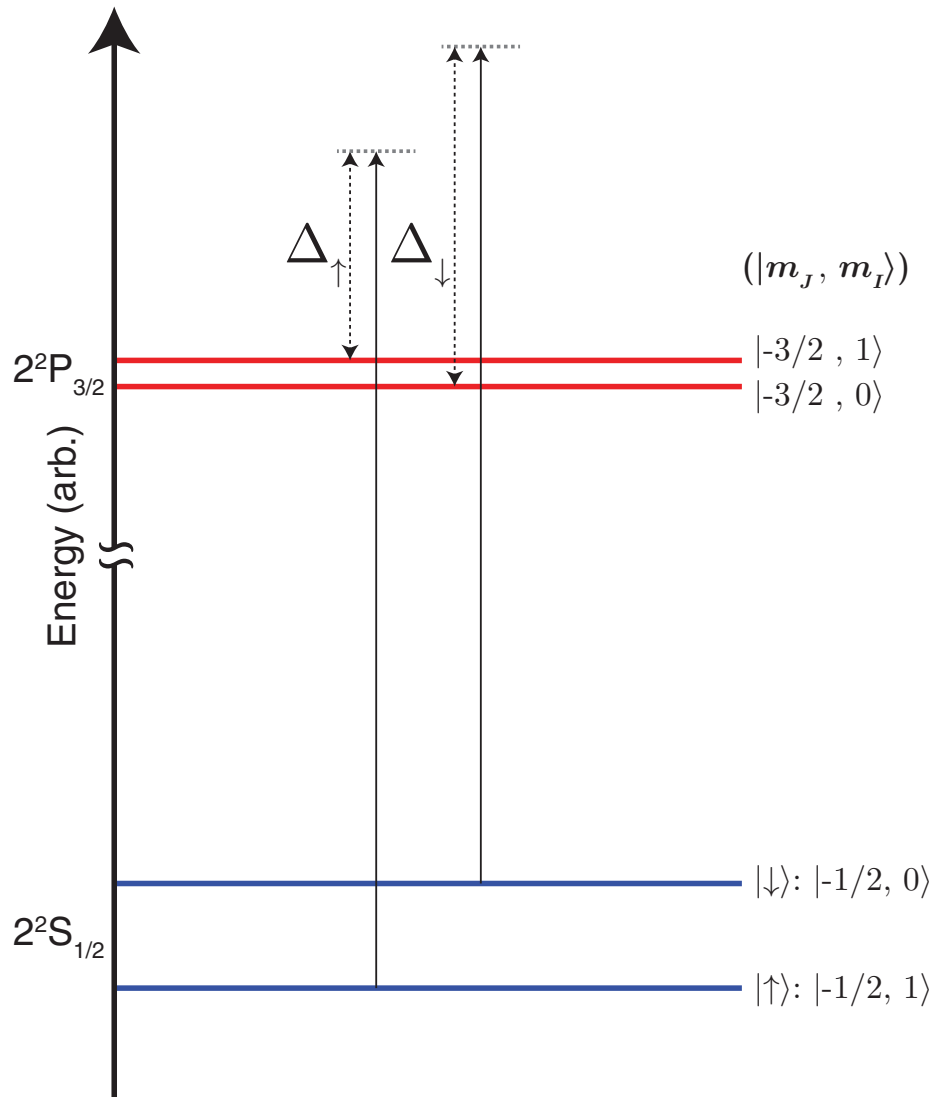


Figure 4.2: A not to scale diagram of the energy transition we take advantage of for Bragg scattering. Here,  $m_J = -1/2 \rightarrow m_J = -3/2$  and  $\Delta m_I = 0$ . The Bragg laser frequency, shown by the black solid vertical arrows, is far detuned from both transitions so that  $\Delta_{\uparrow} \approx \Delta_{\downarrow}$ .

The  $\sigma^+$  transition is much weaker than  $\sigma^-$  due to the Clebsch–Gordan coefficients, as well as being much further detuned due to the Zeeman shift of the excited state, so the atoms will only scatter off  $\sigma^-$  light which travels along the positive  $x$ -direction. The optical setup which applies to both Bragg beams is basically the same, so a single beam setup is shown in figure 4.4.

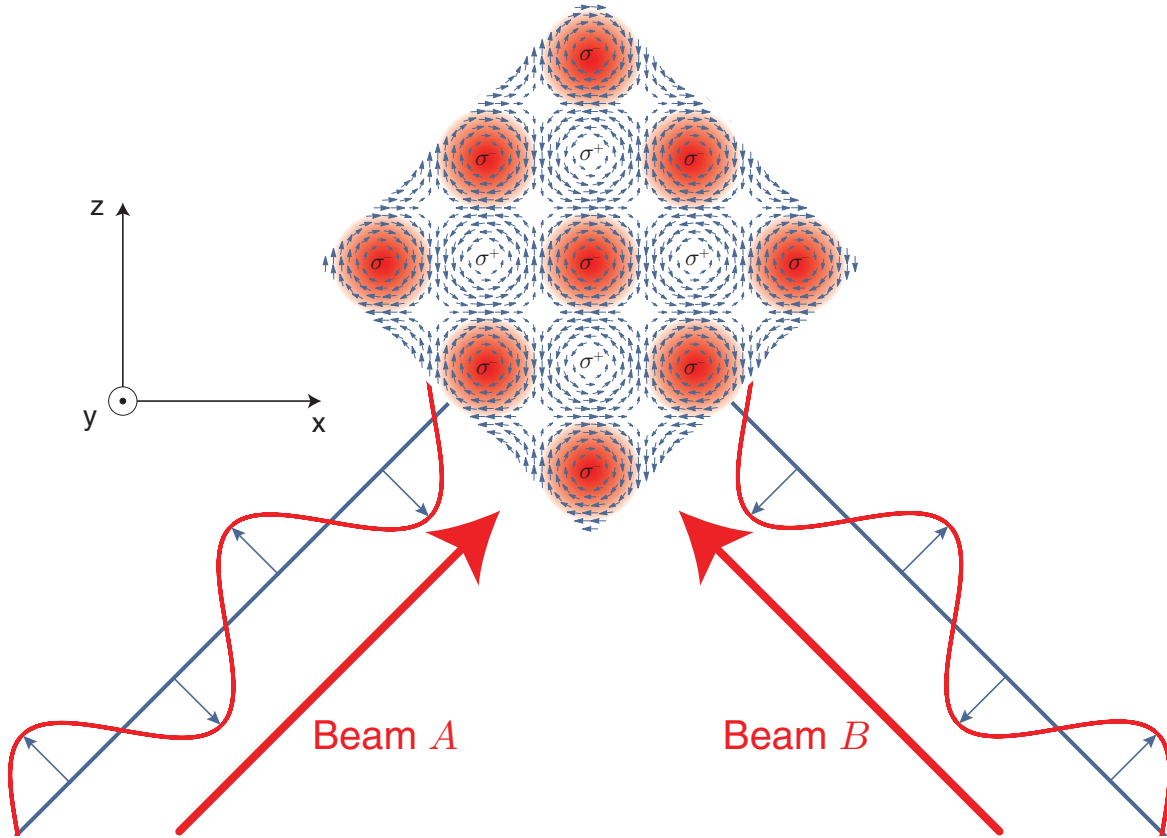


Figure 4.3: An illustration of the Bragg scattering lattice. The two waveforms represent the two incoming Bragg beams, both of which are horizontally polarised as indicated by the blue vector arrows which show the direction of the electric field. When the two beams meet they form the alternating  $\sigma^+$  and  $\sigma^-$  lattice, in which almost all of the atoms Bragg scatter in the  $\sigma^-$  regions highlighted in red. Again, the blue arrows within the lattice represent the direction of the electric field. It should be noted that in this depiction, the two Bragg beams intersect at  $2\theta = 90^\circ$ .

The Bragg lasers are prepared on a table separate from the experiment in order to achieve the correct laser frequencies. On this table, light from a single laser is split into two beams which make up beams *A* and *B* and then their frequencies are independently controlled precisely via a digital synthesiser that is connected to two separate AOMs. The laser beams are coupled into separate single-mode polarisation maintaining optical fibres which lead to the experiment table where the light is collimated at the output and polarised horizontally with the assistance of the two half-waveplates and the polariser,

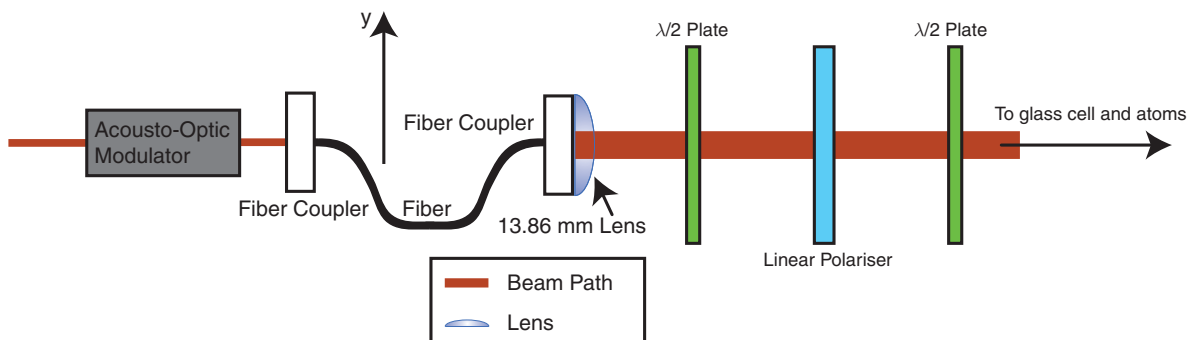


Figure 4.4: A not to scale side view of the final components that make up one of the Bragg beams. Both Bragg beams have a similar setup.

as shown in figure 4.4. Both beams have a Gaussian spatial profile with a waist diameter of 2.65 mm and they are directed to the atoms at the angles indicated in figure 4.1(a). Once the Bragg beams have traveled through the glass cell, their individual powers are measured on two separate photodiodes so that we can monitor and control the intensity of each Bragg pulse.

### 4.2.2 Obtaining a Bragg spectrum

There is a variety of useful information that can be found by probing an ultracold gas using Bragg scattering, even for a fixed momentum. Bragg spectroscopy in our experiment involves varying  $\omega$  by scanning the frequency of Bragg beam *A* whilst beam *B* remains fixed and then measuring how the cloud responds to the pulse. The clouds are exposed to a range of Bragg frequencies in the range  $\omega/2\pi \approx 0 - 360$  kHz in steps of usually around 10 kHz, depending on what feature of the spectrum we are trying to resolve. The response to a Bragg pulse in our experiments is quantified by the momentum transferred to the cloud; however the energy transferred can also be measured. The momentum transferred can be found from the centre-of-mass displacement between a cloud that is scattered with a  $\omega > 0$  pulse and a cloud exposed to a  $\omega = 0$  pulse [34]. The centre-of-mass location of a cloud is found by evaluating its first moment,  $\langle x(\omega) \rangle$ ,

which is given as

$$\langle x(\omega) \rangle = \frac{\sum_i x_i n_\omega(x_i)}{\sum_i n_\omega(x_i)}, \quad (4.4)$$

where  $n_\omega$  is found by essentially calculating  $\tilde{n}(x)$  for a Bragg scattered cloud by integrating over the  $z$ -direction. Because we are only interested in the position of the cloud,  $n_\omega$  can be in arbitrary units. Therefore the response due to the Bragg pulse is

$$X(\omega) = \langle x(\omega) \rangle - \langle x(0) \rangle. \quad (4.5)$$

The energy transferred can be measured through calculating the difference in the widths of the clouds which can be expressed as the difference of their second moments,  $\sigma^2$ :

$$\sigma^2(\omega) = \langle x^2(\omega) \rangle - \langle x(\omega) \rangle^2. \quad (4.6)$$

The response is therefore

$$\Delta\sigma^2(\omega) = \sigma^2(\omega) - \sigma^2(0). \quad (4.7)$$

Because it is difficult to determine the contribution to the width due to the interaction energy, it is desirable to measure the response in this manner for short times of flight before the results can be distorted. While both methods are valid, measuring the response using  $\Delta\sigma^2(\omega)$  tends to yield noisier data because the dark current noise in each camera image away from the cloud centre has a greater contribution to the result (due to the squared terms). Also referring back to section 2.5, the Fermi radius of a cloud has a dependence on the atom number which can fluctuate by 10%, which results in fluctuations in  $\Delta\sigma^2(\omega)$ , and thus is avoided in preference for data obtained by measuring  $X(\omega)$ .

As explained in section 3.4, the CCD takes two images of the atoms. The atoms in state  $|1\rangle$  are captured after a short time of flight (200-300  $\mu\text{s}$  depending on the measurement), and then the atoms in state  $|2\rangle$  are imaged 850  $\mu\text{s}$  later. Despite considerable heating of the cloud by the first imaging pulse, the second image provides crucial information in that the first moment of the cloud after a longer time of flight can still be calculated. The response can therefore be found using a differential approach, expressed

as

$$\Delta X(\omega) = X_2(\omega) - X_1(\omega), \quad (4.8)$$

where  $X_{1(2)}(\omega)$  is the centre-of-mass difference found in equation 4.5 where the first moments are extracted from the state  $|1\rangle(|2\rangle)$  images. In carrying out the measurements in this manner, the signal-to-noise is improved and sensitivity due to fluctuations in the initial cloud position is essentially eliminated.

Measuring the response for a range of Bragg frequencies reveals a spectrum. Shown in figure 4.5 are examples of such Bragg spectra that were used to measure Tan's contact parameter precisely for a cold cloud [63]. These response functions provide a great deal of insight into the properties of the gas, so the rest of this chapter is devoted to the interpretation of these Bragg spectra.

### 4.2.3 Bragg scattering pairs

Usually, two-photon Bragg scattering at high momentum is considered as a process that affects single particles. However, looking at figure 4.5(a), which is a Bragg spectrum for a cold cloud ( $T = 0.08T_F^{\text{HO}}$ ) at unitarity, we can see that there are actually two peaks present that show two separate resonances. One of these peaks occurs very close to the expected atomic resonance,  $\omega = \omega_r$ , and the larger peak occurs at half of the atomic resonance  $\omega = \omega_r/2$ . The Bragg condition in equation 4.2 has a mass term in the denominator, which could indicate that Bragg spectroscopy is sensitive to pairs with a mass of  $2m$  in the system. In two-component Fermi gases, two atoms with different spins can form a pair and their properties are dependent on the  $s$ -wave scattering length and the temperature. As described in more detail in section 2.5 and references therein, these pairs can become tightly bound molecules for positive values of the  $s$ -wave scattering length,  $a > 0$ , or they can be long range Cooper pairs for  $a < 0$  as a consequence of being part of a many-body system. At unitarity where  $a = \infty$ , these pairs display characteristics of both molecules and Cooper pairs. In all three cases, pair-condensation can occur at low temperatures, due to an increase of the number of pairs with zero centre-of-mass momentum. In figure 4.5(b), the spectrum was measured on the BEC side of the Feshbach resonance where the pairs are more tightly bound, and the response at  $\omega = \omega_r/2$  is much more pronounced. As both of these spectra show

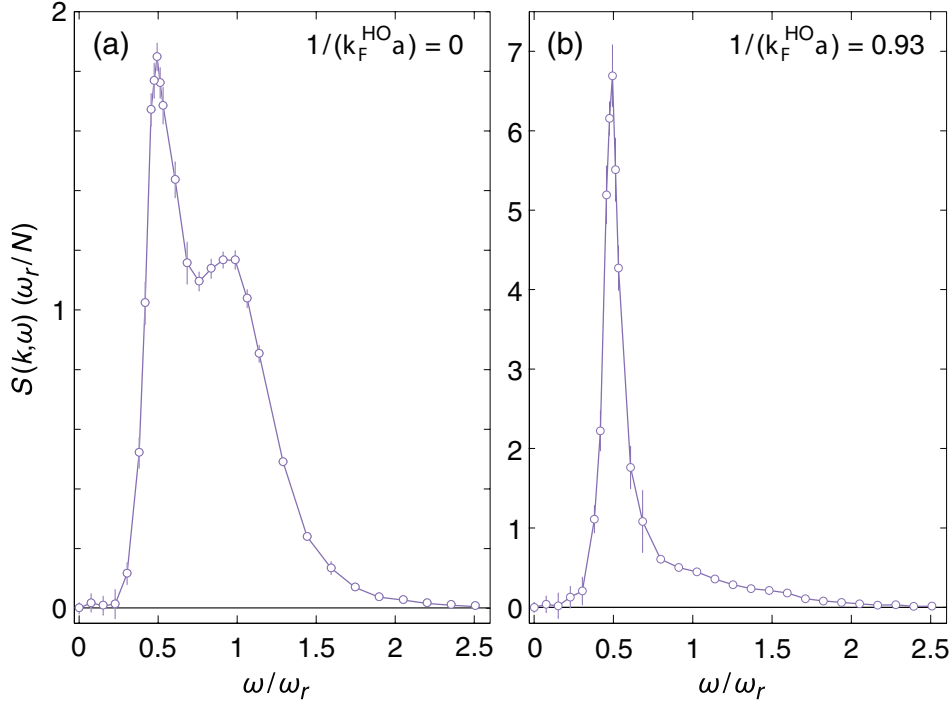


Figure 4.5: Bragg spectra of cold clouds below  $T_C$  from [63]. These show measurements of the dynamic structure factor,  $S$  (which is directly proportional to  $\Delta X$  and introduced later in this chapter), versus Bragg frequency divided by  $\omega_r$ . (a) Spectrum measured at unitarity. (b) Spectrum measured on the BEC side. Reprinted figures with permission from S. Hoinka, M. Lingham, K. Fenech, H. Hu, C. J. Vale, J. E. Drut, and S. Gandolfi, “Precise determination of the structure factor and contact in a unitary Fermi gas,” *Physical Review Letters* **110**(5), 055305 (2013). Copyright 2015 by the American Physical Society (doi: 10.1103/PhysRevLett.110.055305).

a large peak at  $\omega = \omega_r/2$ , this could be an indication that we are scattering many pairs with zero centre-of-mass momentum, which is consistent with pair-condensation.

Due to the marked increase in the Bragg response observed in the spectra shown in figure 4.5 at  $\omega = \omega_r/2$ , it is clear that it is possible to Bragg scatter these atom pairs. But because the energy transferred due to the Bragg pulse is much larger than the amount of energy required to break a weakly bound pair with a binding energy of  $2\Delta$ , the question one might ask is how can these pairs be Bragg scattered?

To clearly understand this scenario we examine this process in terms of centre-of-mass and relative coordinates. We picture two particles, particle 1 and particle

2, in a pair each with velocities  $\mathbf{v}_{1i}$  and  $\mathbf{v}_{2i}$ , respectively. In a weakly bound pair, the electron wavefunctions remain localised with their respective atoms, thus effectively only a single atom from the pair interacts with the lasers driving a two-photon Bragg process. Therefore, if one of the particles, say particle 1, is Bragg scattered whilst particle 2 remains unaffected, the final velocity of particle 1 becomes  $\mathbf{v}_{1f} = \mathbf{v}_{1i} + \hbar\mathbf{k}/m$ . The change in energy in the centre-of-mass degree of freedom,  $\Delta E_{\text{COM}}$ , and the change in energy in the relative degree of freedom,  $\Delta E_{\text{REL}}$ , are

$$\Delta E_{\text{COM}} = \frac{\hbar^2 \mathbf{k}^2}{4m} + \frac{\hbar\mathbf{k}(\mathbf{v}_{1i} + \mathbf{v}_{2i})}{2} \quad \Delta E_{\text{REL}} = \frac{\hbar^2 \mathbf{k}^2}{4m} + \frac{\hbar\mathbf{k}(\mathbf{v}_{1i} - \mathbf{v}_{2i})}{2}. \quad (4.9)$$

The results from chapter 5 show the increase in the number of pairs with zero centre-of-mass momentum by observing the Bragg response of the gas for a Bragg frequency  $\omega_r/2$  as the temperature goes below  $T_C$ . Therefore, we are interested in pairs where  $\mathbf{v}_{2i} = -\mathbf{v}_{1i}$ . In this case,  $\Delta E_{\text{REL}}$  becomes

$$\Delta E_{\text{REL}} = \frac{\hbar^2 \mathbf{k}^2}{4m} + \hbar\mathbf{k}\mathbf{v}_{1i} = \frac{\hbar\omega_r}{2} + \hbar\mathbf{k}\mathbf{v}_{1i} = \hbar\omega - \frac{\hbar\omega_r}{2}, \quad (4.10)$$

where  $\mathbf{k}\mathbf{v}_{1i}$  can be found in equation 4.3. If  $\omega \approx \omega_r/2$ , the change in relative energy can be very small. If the energy required to break a pair in a two-body or many-body setting is twice the pairing gap, we can compare this to the relative degree of freedom in equation 4.10 to find the inequality  $\Delta E_{\text{REL}} < 2\Delta$ :

$$\frac{\omega}{\omega_r} < \frac{2\Delta}{E_r} + \frac{1}{2}. \quad (4.11)$$

Knowing that the value of the pairing gap at unitarity,  $\Delta \approx 0.44\epsilon_F$ [114], is far less than the energy input,  $\omega_r/2$ , it may seem intuitive that the pair will break under these conditions. However this is not the case as the inequality in equation 4.11 can be satisfied for  $\omega \approx \omega_r/2$  with  $2\Delta/E_r$  being non-negligible, therefore a pair may scatter without being broken for  $\omega = \omega_r/2$  or slightly above. If we want to know where the energy goes, by the same token we can take a look at centre-of-mass degree of freedom for  $\mathbf{v}_{2i} = -\mathbf{v}_{1i}$ , and get

$$\Delta E_{\text{COM}} = \frac{\hbar^2 k^2}{4m} = \frac{\hbar\omega_r}{2}. \quad (4.12)$$

This equation holds for any Bragg frequency as long as  $\mathbf{v}_{2i} = -\mathbf{v}_{1i}$ , therefore, for  $\omega = \omega_r/2$ , there is no leftover energy to affect the relative motion. This means that the pair scatters out of the cloud as one with an energy equal to the pairing resonance, and thus most of the energy transferred at the pairing resonance ends up in the centre-of-mass degree of freedom. It is also worth noting that the total energy transferred comes to

$$\Delta E_{\text{TOTAL}} = \Delta E_{\text{COM}} + \Delta E_{\text{REL}} = \hbar\omega, \quad (4.13)$$

meaning that it is conserved in these two degrees of freedom under this scheme. In analysing the Bragg process using these arguments, it is shown that the energy transferred can be shared between the centre-of-mass and the relative degrees of freedom, such that even weakly bound pairs may be Bragg scattered near  $\omega = \omega_r/2$ . At higher Bragg frequencies (e.g.  $\omega \sim \omega_r$ ), pairs with a binding energy that is less than half of the recoil energy will break and free atoms can be scattered leading to the atomic peak near  $\omega_r$ .

### 4.3 Linear Response Theory

This section will outline what the response to a Bragg pulse actually tells us about the system being probed and also sets the restrictions on the Bragg beams in order to obtain reliable information. As described in subsection 4.2.1 the Bragg beams are similarly detuned away from resonance from both spin states. There is no change to either of the internal states, so under these conditions we measure the density perturbation by measuring the response of the density itself, thus it is known as the density-density response. The goal of this work is to measure the momentum transferred to the cloud which is directly proportional to  $\Delta X$ , and then interpret what this tells us about the cloud. The theoretical treatment of this scenario presented here, where a many-body system receives a density perturbation via a momentum transfer due to a Bragg pulse, is closely aligned with the treatment shown in [138] where the context in this reference is neutron scattering. The full Hamiltonian of the many-body system in the absence of

the Bragg perturbation is

$$H_0 = \sum_i \left[ \frac{\mathbf{p}_i^2}{2m} + U(\mathbf{r}_i) \right] + \frac{1}{2} \sum_{i \neq j} V(\mathbf{r}_i - \mathbf{r}_j), \quad (4.14)$$

where  $U$  is the external trapping potential,  $V$  is the interaction potential between atoms, and  $\mathbf{r}_i$  and  $\mathbf{p}_i$  are position and momentum of the  $i$ th particle respectively. The interaction between the Bragg pulse and the ultracold gas can be described by the following Hamiltonian which represents a “walking” wave:

$$H_{\text{Bragg}}(t) = \rho_k^\dagger \varphi(k, \omega) e^{-i\omega t} + \rho_k \varphi^\dagger(k, \omega) e^{i\omega t}. \quad (4.15)$$

Here,  $\rho_k = \sum_i e^{-i\mathbf{k} \cdot \mathbf{r}_i}$  is the Fourier transform of the particle density and describes the density fluctuation around  $\rho_0$ . The  $\varphi(k, \omega)$  term in the Hamiltonian is the Fourier transform of the scalar potential  $\varphi(\mathbf{r}, t)$  provided by the Bragg pulse. This perturbs the density and is given as

$$\varphi(k, \omega) = 2\pi V_{\text{Bragg}} e^{-i\mathbf{k} \cdot \mathbf{R}_{\text{Bragg}}} \delta(\omega - \mathbf{k} \cdot \mathbf{v}_i), \quad (4.16)$$

where  $V_{\text{Bragg}}$  is the Fourier transform of the interaction potential between particle and Bragg light. This is given here as

$$V_{\text{Bragg}} = \hbar \Omega_R, \quad (4.17)$$

where  $\Omega_R$  is the two-photon Rabi frequency and  $\mathbf{R}_{\text{Bragg}}$  is the position of the Bragg scattering event. Equation 4.16 shows that the potential only acts on particles that are resonant with the Bragg pulse. The aim here is to find  $\langle \rho(k, \omega) \rangle$ , which is the expectation value of the density fluctuation due to the probe that determines the momentum transferred to the system. This may be solved through time-dependent perturbation theory to the first order as we are only interested in the linear response. The Hamiltonian in equation 4.15 represents the perturbation so the Schrödinger equation becomes

$$i\hbar \frac{\partial}{\partial t} |\psi(t)\rangle = (H_0 + H_{\text{Bragg}}) |\psi(t)\rangle, \quad (4.18)$$

and the system wave function can be expanded on the basis of unperturbed eigenstates as

$$|\psi(t)\rangle = \sum_n a_n(t) e^{-iE_n t/\hbar} |n\rangle, \quad (4.19)$$

where  $E_n$  is the energy of the eigenstates,  $|n\rangle$ , of  $H_0$ , and  $0 \leq |a_n|^2 \leq 1$  gives the probability that the system is in state  $|n\rangle$ . From here,  $\langle \rho(k, t) \rangle = \langle \psi(r, t) | \rho_k | \psi(r, t) \rangle$  can be solved up to the first order perturbation as outlined in [138], assuming a translationally invariant system ( $\langle 0 | \rho_k | 0 \rangle$ ), given as

$$\langle \rho(k, t) \rangle = \varphi(k, \omega) e^{(-i\omega + \eta)t} \sum_n \left\{ \frac{|(\rho_k^\dagger)_{n0}|^2}{\omega - \omega_{n0} + i\eta} - \frac{|(\rho_k)_{n0}|^2}{\omega + \omega_{n0} + i\eta} \right\}, \quad (4.20)$$

where  $|n\rangle$  and  $|0\rangle$  cannot be coupled by both  $\mathbf{k}$  and  $-\mathbf{k}$  (i.e.  $(\rho_k)_{n0}(\rho_k)_{0n} = 0$ ). Here,  $\omega_{n0} = (E_n - E_0)/\hbar$ ,  $(\rho_k)_{n0} = \langle n | \rho_k | 0 \rangle$  and  $\eta$  is an extra variable included that is positive but close to zero to indicate that the interaction is turned on adiabatically so that the system remains in its ground state  $\epsilon = 0$ . This comes about mathematically by multiplying  $H_{\text{Bragg}}$  by a factor  $e^{\eta t}$  prior to undergoing the perturbation theory. At this point,  $\langle \rho(k, \omega) \rangle$  can be written as it is the Fourier transform of  $\langle \rho(k, t) \rangle$  given as

$$\langle \rho(k, \omega) \rangle = \langle \rho(k, t) \rangle e^{i\omega t} e^{-\eta t}, \quad (4.21)$$

where it is assumed that the perturbation is switched on slowly and it is periodic in time. Substituting equation 4.20 into equation 4.21 leads to

$$\langle \rho(k, \omega) \rangle = \varphi(k, \omega) \sum_n \left\{ \left| (\rho_k^\dagger)_{n0} \right|^2 \frac{1}{\omega - \omega_{n0} + i\eta} - \frac{1}{\omega + \omega_{n0} + i\eta} \right\}, \quad (4.22)$$

where time reversal invariance has been taken advantage of, which states that two degenerate states,  $|m\rangle$  and  $|n\rangle$  can have momenta  $\mathbf{k}$  and  $-\mathbf{k}$  respectively, meaning

$$\sum_n |(\rho_k^\dagger)_{n0}|^2 = \sum_m |(\rho_k)_{m0}|^2. \quad (4.23)$$

Equation 4.22 tells us the expectation value of the density perturbation to the first order, and we will see its usefulness in the context of our experiments, as well as the

limitations we place on the experiment.

### 4.3.1 Dynamical susceptibility and structure factors

An important parameter to consider in these experiments is the dynamical susceptibility,  $\chi$ , and explanations of it can be found in [138–142]. It is a property of the many-body system that describes how it behaves when perturbed by an external field and comes from the fluctuations between particles in the system. In this context, it is given by the ratio of the mean (first order) density perturbation,  $\langle\rho(k, \omega)\rangle$ , to the external potential,  $\varphi(k, \omega)$ :

$$\chi(k, \omega) = \frac{\langle\rho(k, \omega)\rangle}{\varphi(k, \omega)}. \quad (4.24)$$

Hence  $\chi$  is also known as the linear response function. Upon exposure, the response of the system is a combination of a linear term due to the transferral of energy,  $\hbar\omega$ , and momentum,  $\hbar k$ , and higher order terms due to nonlinear effects such as Rabi oscillations and system depletion. The dynamical susceptibility describes the linear part of the response due to the field. It is comprised of a real part,  $\chi'$ , and an imaginary part,  $\chi''(k, \omega)$ , the latter being the observable of interest as it is a measure of the energy dissipation, and therefore the part that (inelastic) Bragg spectroscopy measures. At ultracold temperatures and high- $k$ , the  $\chi''$  is proportional to the dynamic structure factor,  $S(k, \omega)$ . The aim of this section is to understand these parameters and how they relate to our experiments.

Firstly, it is convenient to take a look at the probability flux that arises from the transfer of momentum and energy from the beams. An assumption will be made that the density response is linear, therefore particles are only being scattered in one direction. The Hamiltonian that describes this interaction between the probe and particles can then be written as

$$H_{\text{int}} = \sum_{\mathbf{k}} V_{\text{Bragg}} \rho_{\mathbf{k}}^{\dagger} e^{-i\mathbf{k}\cdot\mathbf{R}_{\text{Bragg}}}. \quad (4.25)$$

Prior to Bragg scattering, the system is in  $|0\rangle$  and both of the Bragg beams have a combined momentum of  $N_A\hbar\mathbf{k}_A + N_B\hbar\mathbf{k}_B$ , where  $N_{A(B)}$  is the number of photons in beam  $A(B)$ . After a single scattering event, beam  $A$  has lost a photon to beam  $B$ , so

the total momentum of the beams is now  $(N_A - 1)\hbar\mathbf{k}_A + (N_B + 1)\hbar\mathbf{k}_B$  and the system ends up in state  $|n\rangle$ . Therefore

$$\langle n, (N_A - 1)\hbar\mathbf{k}_A + (N_B + 1)\hbar\mathbf{k}_B | \sum_{\mathbf{k}} V_{\text{Bragg}} \rho_{\mathbf{k}}^\dagger e^{-i\mathbf{k} \cdot \mathbf{R}_{\text{Bragg}}} | 0, N_A \hbar\mathbf{k}_A + N_B \hbar\mathbf{k}_B \rangle = V_{\text{Bragg}} \left( \rho_{\mathbf{k}}^\dagger \right)_{n0}. \quad (4.26)$$

Using equation 4.26 in Fermi's golden rule, we can find the probability per unit time,  $\Gamma$  of transferring energy,  $\hbar\omega$  and momentum  $\hbar\mathbf{k}$ . This gives

$$\Gamma(k, \omega) = \frac{2\pi}{\hbar} |V_{\text{Bragg}}|^2 \sum_n \left| \left( \rho_{\mathbf{k}}^\dagger \right)_{n0} \right|^2 \delta(\omega - \omega_{n0}) = \frac{2\pi}{\hbar} |V_{\text{Bragg}}|^2 S(k, \omega), \quad (4.27)$$

where we have introduced the dynamic structure factor,  $S(k, \omega)$ :

$$S(k, \omega) = \sum_n \left| \left( \rho_{\mathbf{k}}^\dagger \right)_{n0} \right|^2 \delta(\omega - \omega_{n0}). \quad (4.28)$$

Equation 4.28 shows that the dynamic structure factor reveals the excitation spectrum in which density fluctuations can occur for a given energy and momentum. From a historical perspective, the dynamic structure factor has been measured in liquid  $^4\text{He}$  using inelastic neutron scattering. It was realised in the 1950's that the pair correlations of a system in both space and time can be determined using this technique by measuring the differential scattering cross-section [24] of the atoms in the sample. This scheme is described in many texts including [29, 138], and others. A beam of neutrons impinge upon a sample of cold  $^4\text{He}$ , and proceed to deflect off the  $^4\text{He}$  nuclei where they are then picked up by an array of detectors located at different angles. The angle at which the neutron deflects off the sample can give the momentum transferred  $\hbar\mathbf{k}$ . These measurements are performed over a time span so the detectors can also measure the histogram of neutrons colliding with them over time,  $\tau$ , which gives  $S(k, \tau)$ . Taking the Fourier transform of this histogram over the time domain gives the dynamic structure factor (in the frequency domain) and knowledge of the incident energy of the neutrons allows determination of the energy transferred,  $\hbar\omega$ . Probing the liquid  $^4\text{He}$  in this manner using a high momentum transfer (i.e.  $1/k > n^{-3}$ , where  $n$  is the density) proved to be useful as the momentum distribution of the sample could then be determined using the impulse approximation [25]. Then through a series of theoretical studies an accurate

value of the condensate fraction of  $(10 \pm 1.25)\%$  was found [29, 31] for a temperature  $T = 0.35T_C$ .

Taking the Fourier transform of the dynamic structure factor in equation 4.28 gives  $S(k, \tau)$  and allows one to look at the time evolution of the density correlations:

$$S(k, \tau) = \sum_n \left| \left( \rho_k^\dagger \right)_{n0} \right|^2 e^{-i\omega_{n0}\tau} = \hbar \sum_n \langle 0 | e^{iH\tau/\hbar} \rho_k e^{-iH\tau/\hbar} | n \rangle \langle n | \rho_k^\dagger | 0 \rangle. \quad (4.29)$$

In the interaction picture the time dependence of the density correlation operator is given as  $\rho_k(\tau) = e^{iH\tau/\hbar} \rho_k e^{-iH\tau/\hbar}$ . Therefore, equation 4.29 gives

$$S(k, \tau) = \langle 0 | \rho_k(\tau) \rho_k^\dagger(0) | 0 \rangle. \quad (4.30)$$

The dynamic structure factor at  $\tau = 0$  is of interest here, as it gives information about the instantaneous density correlations in the system without the perturbation. In fact  $S(k, \tau = 0)$  is known as the static structure factor,  $S(k)$ , which as explained in section 2.6 is a quantity from which Tan's universal contact can be derived. This can be expressed as the integral of the dynamic structure factor across all energies per particle, or the zeroth order moment of the dynamic structure factor:

$$S(k) = \frac{1}{N} \int S(k, \omega) d\omega. \quad (4.31)$$

As mentioned previously, the imaginary part of the dynamical susceptibility can be related to the dynamic structure factor. To understand this, we return to the definition of the dynamical susceptibility in equation 4.24. Substituting equation 4.22 and equation 4.16 into equation 4.24, the first order susceptibility becomes

$$\chi(k, \omega) = \sum_n \left| \left( \rho_k^\dagger \right)_{n0} \right|^2 \frac{2\omega_{n0}}{(\omega + i\eta)^2 - \omega_{n0}^2}. \quad (4.32)$$

The susceptibility can be related back to the dynamic structure factor by integrating both sides of equation 4.28 and making  $\omega = \omega'$ , and inserting it into equation 4.32 to

eliminate the  $\delta$ -function:

$$\chi(k, \omega) = \int_0^\infty d\omega' S(k, \omega') \left[ \frac{1}{\omega - \omega' + i\eta} - \frac{1}{\omega + \omega' + i\eta} \right]. \quad (4.33)$$

In this form,  $\chi$  can be split into its real and imaginary parts through the use of the formula

$$\lim_{\eta \rightarrow 0} \frac{1}{\omega - \omega' + i\eta} = \frac{P}{\omega - \omega'} - i\pi\delta(\omega - \omega'), \quad (4.34)$$

where  $P$  is the principal value. Through the use of Kramers-Kronig relations [143, 144] the real and imaginary parts of the dynamical susceptibility are expressed as

$$\chi'(k, \omega) = P \int_0^\infty d\omega' S(k, \omega') \frac{2\omega'}{\omega^2 - \omega'^2}, \quad (4.35)$$

$$\chi''(k, \omega) = \pi[S(k, \omega) - S(-k, -\omega)]. \quad (4.36)$$

Equation 4.36 indicates that not only is there scattering of particles due to the probe, but also scattering from particles into the probe. The latter can only occur if there are particles that initially have energy  $\hbar\omega$  that can be transferred back to the probe. The probability of this occurring is  $e^{-\beta\hbar\omega}$ , the temperature dependence coming from  $\beta = 1/k_B T$ . This leads to the detailed balancing condition:

$$S(k, \omega) = e^{-\beta\hbar\omega} S(-k, -\omega). \quad (4.37)$$

Therefore at zero-temperature  $\chi''(k, \omega) = \pi S(k, \omega)$  and at finite temperature we have the fluctuation-dissipation theorem [139]:

$$\chi''(k, \omega) = \pi[1 - e^{-\beta\hbar\omega}]S(k, \omega). \quad (4.38)$$

For the experiments presented in this thesis, we measure this parameter (i.e.  $\chi''(k, \omega) \propto \Delta X(\omega)$ ). The cloud temperatures are very small meaning that  $e^{-\beta\hbar\omega} \ll 1$  for the range of  $\hbar\omega$  that we scan in our high- $k$  Bragg measurements in order to measure the response. This means that the  $\chi''(k, \omega) \approx \pi S(k, \omega)$  under our conditions.

### 4.3.2 $f$ -sum rule

The Bragg measurements that have been described so far are sensitive to the energy dissipation into the system, which is the imaginary part of the dynamical susceptibility  $\chi''(k, \omega)$ . In the limit of high momentum and low temperature, this turns out to be proportional to the dynamic structure factor  $S(k, \omega)$ . The next step in the process is to find out how to extract meaningful quantities from a Bragg spectrum. What we have so far is a signal measured in pixels using equation 4.8, from which it is easy enough to calculate the momentum transferred to the cloud, knowing the time of flight and pixel size on the CCD. To investigate the quantities probed by Bragg spectroscopy further, we begin by considering the full Hamiltonian,  $H_0$  given in equation 4.14. We will make use of the commutator  $[\rho_k, H_0]$ , taking advantage of the fact that  $U$  and  $V$  are velocity independent:

$$[\rho_k, H_0] = \frac{\hbar}{2m} \sum_i \mathbf{k} \cdot \mathbf{p}_i e^{-i\mathbf{k} \cdot \mathbf{r}_i} + e^{-i\mathbf{k} \cdot \mathbf{r}_i} \mathbf{k} \cdot \mathbf{p}_i. \quad (4.39)$$

Relating this back to the current density fluctuations which is given by the Fourier transform of the current density operator

$$\mathbf{J}_k = \frac{1}{2m} \sum_i \mathbf{p}_i e^{-i\mathbf{k} \cdot \mathbf{r}_i} + e^{-i\mathbf{k} \cdot \mathbf{r}_i} \mathbf{p}_i, \quad (4.40)$$

we can see that in the Heisenberg picture (i.e.,  $i\hbar \partial \rho_k / \partial t = [\rho_k, H]$ ) the Fourier transform of the continuity equation,  $\partial \rho / \partial t + \nabla \cdot \mathbf{J} = 0$ , is derived as

$$i\hbar \frac{\partial \rho_k}{\partial t} = [\rho_k, H_0] = \hbar \mathbf{k} \cdot \mathbf{J}_k. \quad (4.41)$$

This means that the commutator relates the time evolution of the density fluctuation to the current density fluctuation. Particle conservation comes into the picture when we evaluate the double commutator,  $[[\rho_k, H_0], \rho_k]$  with its eigenvalues in the ground state,  $\langle 0 | [[\rho_k, H_0], \rho_k] | 0 \rangle$ . The explicit derivation of the double commutator yields

$$[[\rho_k, H_0], \rho_k] = \frac{N\hbar^2 k^2}{m}, \quad (4.42)$$

where  $N$  is the total atom number or the sum of all  $i$  particles. The double commutator in the ground state is found by inserting the identity operator  $\sum_n |n\rangle \langle n|$ :

$$\langle 0 | [[\rho_k, H_0], \rho_k] | 0 \rangle = \sum_n \hbar \omega_{n0} |(\rho_k^\dagger)_{n0}|^2 + \sum_n \hbar \omega_{n0} |(\rho_k)_{n0}|^2 = 2\hbar \sum_n \omega_{n0} |(\rho_k^\dagger)_{n0}|^2, \quad (4.43)$$

where the final answer on the right hand side of equation 4.43 comes about from time reversal shown invariance in equation 4.23. Therefore

$$\sum_n \omega_{n0} \left| (\rho_k^\dagger)_{n0} \right|^2 = \frac{N\hbar k^2}{2m}. \quad (4.44)$$

Multiplying both sides of equation 4.28 by  $\omega$  and then integrating over  $\omega$  gives exactly the quantity considered in equation 4.44. The expression below is known as the  $f$ -sum rule, which applies for all  $k$  and is a consequence of particle conservation:

$$\int d\omega \omega S(k, \omega) = \frac{N\hbar k^2}{2m}. \quad (4.45)$$

So we can see that the expectation value of the double commutator in the ground state reveals the first moment of the dynamic structure factor, and comparing it to the explicit calculation of the double commutator in equation 4.42 gives the particle conservation law that the dynamic structure factor obeys. In section 6.3, it is explained how these identities enable the measurement of the structure factors through a simple normalisation, rather than performing difficult measurements on experimental parameters in the laboratory.

## 4.4 Summary

Bragg spectroscopy is a highly useful technique to measure density correlations in a many-body system. By exposing an ultracold gas to two off-resonant lasers with a frequency difference of  $\omega$ , the system responds due to the momentum transfer from the probe, which can be quantified by measuring the centre-of-mass displacement of the cloud. When Bragg scattering a two-component Fermi gas, a pairing resonance arises

at  $\omega = \omega_r/2$ , as well as the usual atomic resonance,  $\omega = \omega_r$ , which means that this technique is sensitive to the scattering of pairs. The density response to the first order of the ultracold gas is proportional to imaginary part of the dynamical susceptibility and hence the dynamic structure factor. The dynamic and static structure factors can be calculated and should obey the  $f$ -sum rule. In the subsequent chapters, these understandings will form the basis of our data analysis.

# Chapter 5

## Local measurement of pair-condensation

### 5.1 Introduction

A key to furthering our understanding of various low-temperature systems is to identify phase boundaries as the system is cooled [29, 110, 145]. However, observing and identifying pair-condensation in a unitary Fermi gas has proven quite a challenge in the past as it leads to only a slight variation in the atomic density which is difficult to detect [90]. As mentioned in chapter 1, pair-condensation was first observed in 2004 where a gas of  $^{40}\text{K}$  atoms was released from the trap and subjected to a fast ramp to the far BEC side, making the pairs tightly bound [16–18]. The pairs maintained their original centre-of-mass momentum, so below a certain temperature a bimodal distribution appeared indicating the appearance of pair-condensation. It can be assumed that the pairs maintained their centre-of-mass momentum when the timing of this rapid ramp is tuned correctly while the scattering length is tuned; however there are other effects that occur with such a sweep, such as an increase in the paired fraction leading to production of molecules within the sweep [89]. Another problem with this technique arises due to the varying trapping potential provided by the hybrid optical and magnetic trap in which the atoms are held. This results in a varying density (and therefore Fermi energy) throughout the atomic cloud making it inhomogeneous, and since condensation

occurs where the temperature of the cloud is a small enough fraction of the local Fermi temperature only the high density regions of a sufficiently cold cloud will condense. So when the cloud is released from the trap with a long time of flight to measure the momentum distribution, information about where the condensate formed in the initial trap is not accessible in images of the expanded cloud.

Another signature of condensation is the collective, or Goldstone mode [146–148]. This mode is the lowest possible excitation in a system that has undergone a continuous symmetry breaking transition to gain long-range order. As outlined in section 2.7, at low momentum, this mode has linear dispersion, which provides information on the speed of sound in the system. For higher momentum the dispersion evolves into a quadratic relation [118], indicating that it is associated with the scattering of pairs of atoms out of the condensate [33, 46, 149, 150].

Signatures of pairing have been observed using spectroscopic techniques such as radio-frequency spectroscopy [20–23], and as shown in the previous chapter, Bragg spectroscopy. The limitations to these techniques include the inhomogeneity of the harmonically trapped gas, and also the fact that absorption imaging obtains a two-dimensional projection of a three-dimensional cloud. A suitable way to overcome these limitations when measuring the homogeneous density is through the use of the inverse Abel transform, as shown in section 3.5. However, Bragg scattering loses the symmetry required for the inverse Abel transform, so it is not practical for these measurements. In order to measure the point where pair-condensation occurs, measurements will need to be made locally. This chapter presents a technique used to directly observe local pair-condensation by probing the cloud *in situ* using Bragg spectroscopy.

## 5.2 A closer inspection of Bragg scattered images

As mentioned in subsection 4.2.2 of the previous chapter, Bragg spectroscopy on a cold cloud prepared at unitarity reveals a free atom peak and a pair peak. As the temperature of the cloud increases, the height of the pairing peak shrinks and eventually disappears. Because pair-condensation involves a macroscopic number of pairs with zero centre-of-mass momentum, this could prompt one to take a closer look at what is happening at the two peaks in the Bragg spectra.

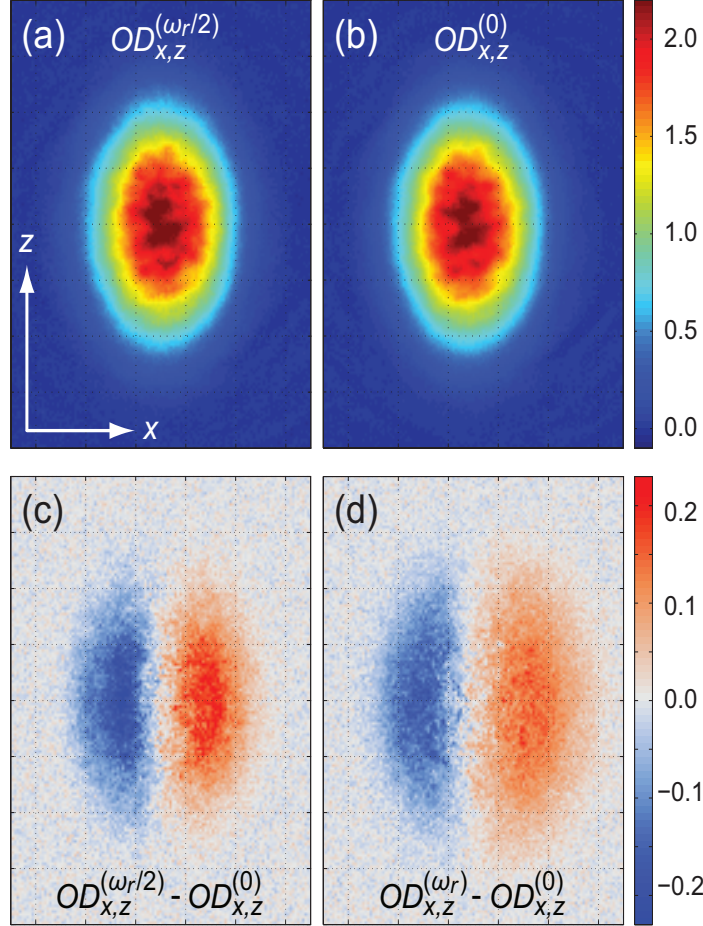


Figure 5.1: (a) and (b): Absorption images of atoms that have been Bragg scattered with  $300 \mu\text{s}$  time of flight after exposure to a  $200 \mu\text{s}$  long Bragg pulse with  $33 \mu\text{W}$  in each beam. (a) is scattered at the pairing resonance  $\omega = \omega_r/2$ , while (b) has experienced no Bragg scattering  $\omega = 0$ . (c) is the  $\omega = 0$  image subtracted from the  $\omega = \omega_r/2$  image. (d) is the  $\omega = 0$  image subtracted from the  $\omega = \omega_r$  image. This image has been taken directly from [1].

Shown in figure 5.1 are two images that look rather similar. Figure 5.1(a) has been exposed to a  $\omega = \omega_r/2$  Bragg pulse which is sensitive to the scattering of pairs whereas figure 5.1(b) has received no momentum transfer ( $\omega = 0$ ). Subtracting figure 5.1(b) from figure 5.1(a) reveals the difference between the two images, figure 5.1(c). We can see that the atoms in figure 5.1(a) have been displaced in the  $x$ -direction with respect to figure 5.1(b). Figure 5.1(d) is similar to figure 5.1(c), except the  $\omega = 0$  image has been

subtracted from a  $\omega = \omega_r$  image which is sensitive to the scattering of free atoms. If we look closely at figures 5.1(c) and 5.1(d), we can see a subtle difference. In figure 5.1(c), the displacement of atoms appears to occur mostly from the centre of the cloud but in figure 5.1(d) the response is more diffuse and we see more displacement around the wings of the cloud. It was noted in the last chapter that the size of the Bragg beams are much larger than the cloud diameter, therefore all of the atoms experience the same intensity.

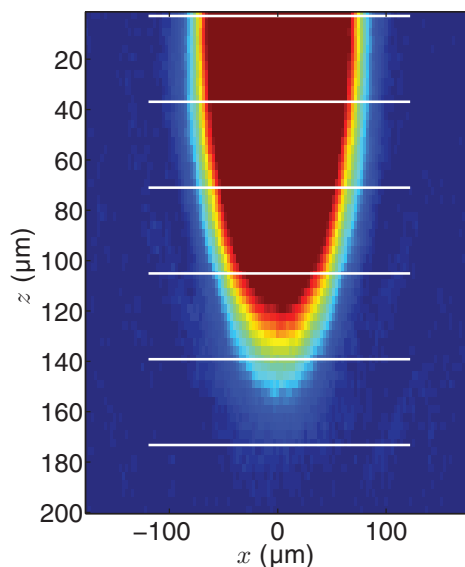


Figure 5.2: Example of an absorption image folded in half and divided into slices with a width of twelve pixels.

Taking into account these observations, the centre-of-mass displacement in the  $x$ -direction can be measured as a function of  $z$ -direction. This is achieved by dividing each image in the spectrum into slices with a certain pixel width as shown in figure 5.2 and measuring the response within each slice. The result of this is shown in figure 5.3. The pairing peak shrinks with increasing  $z$  while the atomic response increases, due to the fact that the local  $T/T_F(z)$  is increasing. The response or centre-of-mass displacement of each slice is weighted by the number of atoms in the slice and is an integrated quantity over both the imaging axis,  $y$ , and the direction which the atoms are Bragg scattered,

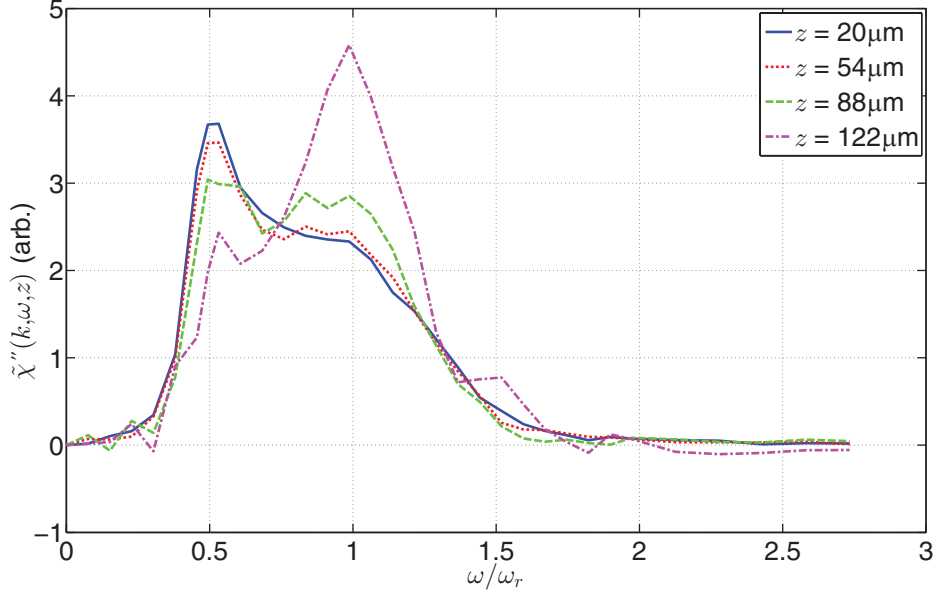


Figure 5.3: The response spectra for every slice along the  $z$ -direction shown in figure 5.2. We can see that as  $z$  increases, the peak at  $\omega_r/2$  decreases. For these figures, the Bragg pulse duration is  $50 \mu\text{s}$  and the time of flight is  $300 \mu\text{s}$ .

$x$ :

$$\tilde{\chi}''_{(k,\omega)}(z) = \frac{1}{\tilde{n}(z)} \int \chi''_{(k,\omega)}(\mu(\mathbf{r}), T) n(\mu(\mathbf{r}), T) dx dy. \quad (5.1)$$

Here,  $\chi''_{(k,\omega)}$  is the homogeneous density-density response function,  $\mu$  is the chemical potential,  $T$  is the temperature of the cloud,  $\tilde{n}(z) = \int n(\mu(\mathbf{r}), T) dx dy$  is the doubly-integrated line density, and  $n(\mu(\mathbf{r}), T)$  is the homogeneous density. We have assumed that both  $n$  and  $\chi''$  follow the local density approximation. The density can be treated as such because small volumes of the cloud can be assumed to be homogeneous which allows us to infer homogeneous density from the line density, as shown in section 3.5.  $\chi''$  can also follow the local density approximation because at high- $k$ , the scattering is sensitive to short-range correlations (i.e.  $1/k < n^{-1/3}$ ). All such measurements are density-weighted, so the measurement of the bulk response is equivalent to integrating equation 5.1 over  $z$  as well. Equation 5.1 shows that the response per slice is the homogeneous response function weighted by the local density and integrated over all atoms in the slice; hence we call it the line response.

### 5.3 Extracting local information

The aim is now to extract the homogeneous response,  $\chi''$ , from the density-weighted line response,  $\tilde{\chi}''$ . The results in this chapter use a generalised version of the scheme shown in [82], and outlined again in section 3.5 of this thesis where the homogeneous density was extracted from the doubly-integrated density profile. Here we show that this method can be extended to any variable that satisfies the local density approximation, including dynamic quantities. Picture any homogeneous quantity,  $A(\mu, T)$ , where the signal obtained,  $\tilde{A}$ , is density-weighted. This can be expressed in a similar way to equation (5.1):

$$\tilde{A}(z) = \frac{1}{\tilde{n}(z)} \int_{-\infty}^{\infty} A(\mu(\mathbf{r}), T) n(\mu(\mathbf{r}), T) dx dy. \quad (5.2)$$

Substituting the Gibbs-Duhem equation  $dP = n d\mu$  and equation (3.14) gives

$$\tilde{A}(z) \tilde{n}(z) = \frac{2\pi}{m\omega_x \omega_y} \int_{P[\infty, \infty, z]}^{P[0, 0, z]} A(\mu(\mathbf{r}), T) dP. \quad (5.3)$$

Differentiating both sides with respect to  $P$  gives

$$\frac{d(\tilde{A}(z) \tilde{n}(z))}{dP} = \frac{2\pi}{m\omega_x \omega_y} \int_{P[\infty, \infty, z]}^{P[0, 0, z]} \frac{dA(\mu(\mathbf{r}), T) dP}{dP}. \quad (5.4)$$

As the distance from the centre of the cloud goes to  $x, y \rightarrow \infty$ , the chemical potential goes to  $\mu \rightarrow -\infty$ , meaning that the density and the pressure in this limit,  $P[\infty, \infty, z] \rightarrow 0$ . The other limit,  $P[0, 0, z]$  is given by equation (3.15) so we conclude the following:

$$A(\mu[0, 0, z], T) = \frac{d[\tilde{A}(z) \tilde{n}(z)]}{d\tilde{n}(z)}. \quad (5.5)$$

This means that the local value  $A$  along the axis  $z$  of the harmonic trap through the centre of the cloud can be evaluated from the derivative of density-weighted quantity,  $\tilde{A}$ , multiplied by the line density.

## 5.4 Measuring the homogeneous density-density response

The variable  $A$  in equation 5.5 can take the form of a range of dynamic variables including the RF spectral function or, in this case, a Bragg response. Replacing  $A$  with  $\chi''_{(k,\omega)}$  in equation 5.5, we extract the homogeneous response to a two-photon Bragg pulse:

$$\chi''_{(k,\omega)}(\mu[0, 0, z], T) = \frac{d[\tilde{\chi}''_{(k,\omega)}(z)\tilde{n}(z)]}{d\tilde{n}(z)}. \quad (5.6)$$

Applying equation (5.6) to the sliced spectra in figure 5.3, we obtain homogeneous Bragg spectra, as shown in figure 5.4 for various slices with their distance from the cloud centre shown in the legend. Note that even though the Bragg scattering process breaks the cylindrical symmetry of the cloud, we can still obtain local information as the cloud was initially trapped in a harmonic trap and we integrate over the  $x$ -direction to obtain the line profile.

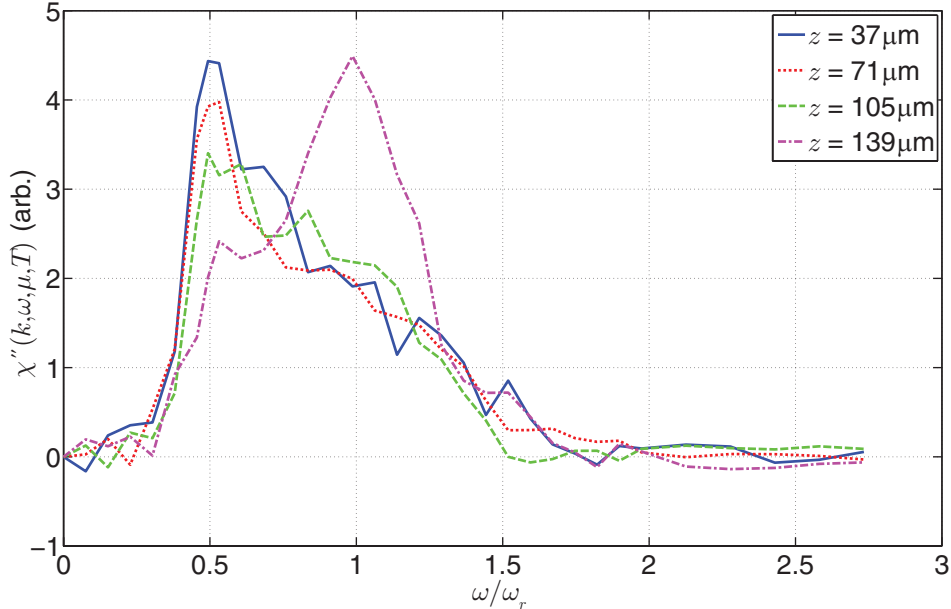


Figure 5.4: Homogeneous spectra at various  $z$ -locations in a cloud. In order to carry out the derivative in equation 5.6, the difference is taken between the spectra in figure 5.3; hence the values of  $z$  have changed to be halfway between the initial slices.

As these spectra all come from a single cloud, we are able to cover a range of local temperatures  $T/T_F(z)$  and wavevectors  $k/k_F(z)$  in a single measurement. There is a qualitative difference between the homogeneous spectra shown in figure 5.4, compared to the trap-averaged case (see figures 4.5(a) and 6.2). The homogeneous spectra close to the cloud centre show just a single peak at  $\omega = \omega_r/2$  which has a long tail to high- $\omega$  and no clear atomic peak. This shows similar qualitative behaviour to the homogeneous spectrum calculated by Combescot *et al.* reference [33]. Again, the peak at  $\omega_r/2$  recedes for higher local temperatures out in the wings of the cloud and the atomic response at  $\omega_r$  actually dominates the spectrum. Weighting these spectra by the density and adding them together would return the bulk spectrum of the entire cloud again, except now we have spatial information on where the two peaks come from. Using this new technique to extract local information, it is now possible to identify what is really happening at the pairing peak.

## 5.5 Response at the pairing resonance

Next, we take a series of shots of Bragg scattered clouds, alternating the Bragg frequency between  $\omega = 0$  and  $\omega = \omega_r/2$  for a range different temperatures. The thought process here is that for  $\omega = \omega_r/2$  we expect to be sensitive to the scattering of pairs with zero centre-of-mass momentum, as explained in subsection 4.2.3, so local measurements could provide an insight into the number of these pairs as a function of the local temperature. The global temperature of the cloud can be varied by releasing the atoms from the optical trap for a short time (0-2 ms) and recapturing the cloud and waiting 500 ms for re-equilibration. Another way we control the temperature is to vary the evaporation end point. For these measurements, the Bragg pulse duration is increased to 200  $\mu\text{s}$  in order to narrow the Fourier spectral width, and the power of both Bragg lasers is 33  $\mu\text{W}$ . After the Bragg pulse, the atoms are released from the trap for 300  $\mu\text{s}$  before they are imaged. In order to increase signal to noise, the imaging pulse duration is increased to 5  $\mu\text{s}$ , but low intensity,  $I=0.8I_{sat}$ , because we are only interested in centre-of-mass related information from these images while the atom number is not so much of a concern. From these images, the line response,  $\tilde{\chi}(k, \omega_r/2, z)$ , is extracted. Shown in figure 5.5(a) are the line responses for four different temperature clouds.

These are obtained by using a ten pixel wide window and finding the centre-of-mass displacement within the window. The central pixel is  $z$  and then the window is shifted by  $z + 1$  to get the next data point. Toward the centre of the cloud, the window size is restricted. Because these windows are smaller, the signal from the pixels close to the centre becomes noisier.

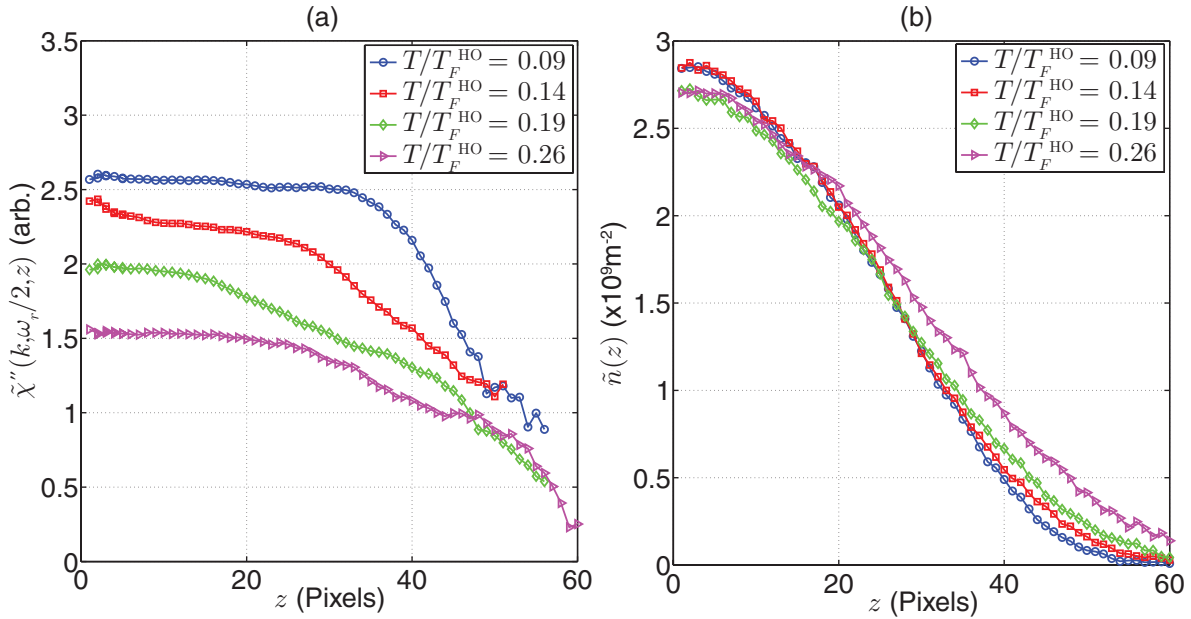


Figure 5.5: The two parts needed to extract the homogeneous response. The bulk temperatures are quoted in the legends. (a) The density-weighted response. A ten pixel wide window is used where the centre-of-mass displacement is found within that window, and then the window is shifted by one pixel.  $z$  is the central pixel of the window. (b) Doubly-integrated line density found by taking *in situ* shots with a high intensity imaging beam ( $\tau = 1 \mu\text{s}$ ,  $I = 20I_{\text{sat}}$ ). In both figures, the blue circles represent data from a cloud with a bulk temperature  $T = 0.09T_F^{\text{HO}}$ , the red squares are data for  $T = 0.14T_F^{\text{HO}}$ , the green diamonds are data for  $T = 0.19T_F^{\text{HO}}$ , and the magenta triangles are data for  $T = 0.26T_F^{\text{HO}}$ .

Along with the Bragg scattered images, several *in situ* shots are taken at each temperature to obtain the doubly-integrated line density  $\tilde{n}(z)$ . These are also used to extract the homogeneous density and perform thermometry on the cloud as described in sections 3.5 and 3.6. The imaging intensity for these shots is increased to  $I=20I_{\text{sat}}$  in order to accurately determine the true optical density of the cloud, while the pulse

duration is decreased to  $1 \mu\text{s}$  to reduce recoil blurring and Doppler shifting of the atoms out of resonance mid pulse, as lithium is a very light element. Integrating these images across  $x$  gives  $\tilde{n}(z)$ , as shown in figure 5.5(b). Now that we have both  $\tilde{\chi}(k, \omega_r/2, z)$ , and  $\tilde{n}(z)$ , equation 5.6 can be applied to give figure 5.6.

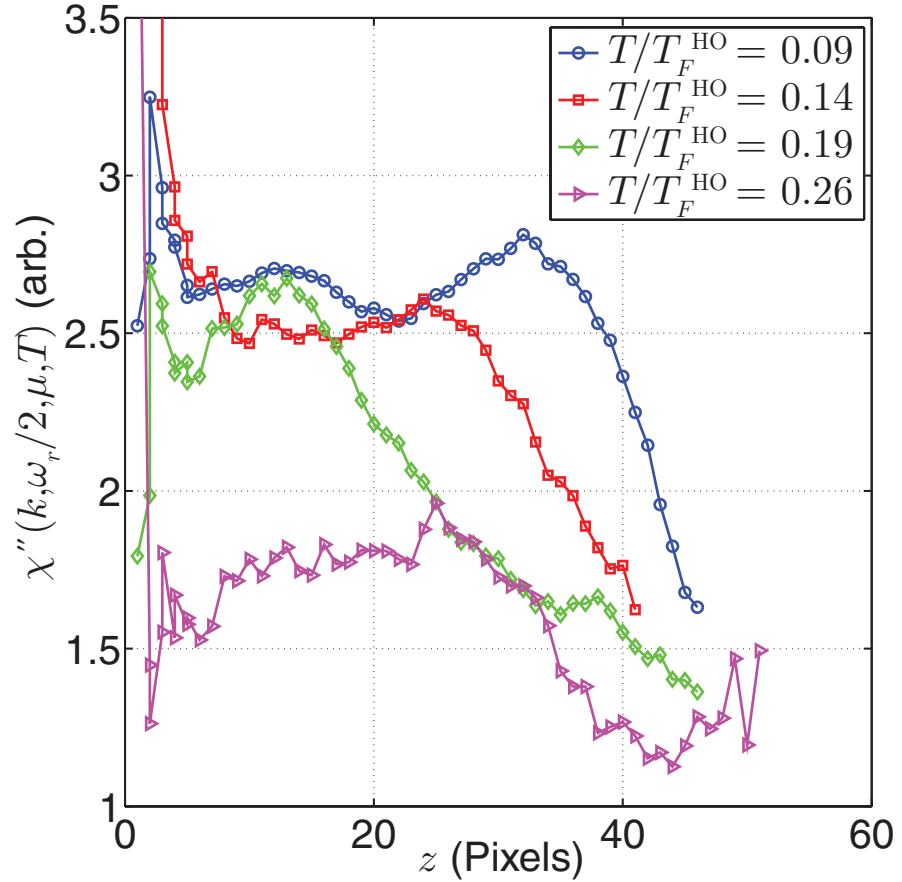


Figure 5.6: Homogeneous response versus  $z$  extracted from the data sets in figure 5.5. The blue circles represent data from a cloud with a bulk temperature  $T = 0.09T_F^{\text{HO}}$ , the red squares are data for  $T = 0.14T_F^{\text{HO}}$ , the green diamonds are data for  $T = 0.19T_F^{\text{HO}}$ , and the magenta triangles are data for  $T = 0.26T_F^{\text{HO}}$ .

The noise toward the centre of the clouds is attributed to the smaller window sizes mentioned before and the fact that a derivative has been performed on the noisy data. At around  $z > 10$ , the signal becomes more clear. Inspecting this data, we can see that for the three coldest clouds ( $T/T_F^{\text{HO}} = 0.09, 0.14, 0.19$ ), the homogeneous responses towards the centre are similar. However, the response drops for increasing  $z$  with the

first to drop being the data represented by the green diamonds which is the hottest of the three aforementioned clouds, then the red squares drop, followed the blue circles which is the coldest of the three. The colder the cloud is, the further away from the centre the homogeneous response drops suggesting a higher fraction of pairs with zero momentum. This provides an indication that the physical size of the pair-condensate in the trap grows as the global temperature is reduced. We can also see that the response for the hottest cloud ( $T/T_F^{\text{HO}} = 0.26$ ) represented by the magenta triangles in figure 5.6, does not reach anywhere near as high as the response data for the other three clouds, indicating that there is no pair-condensation present in this cloud.

## 5.6 Homogeneous response and its temperature dependence

Now we are able to determine the dependence of the homogeneous density-density response on the local temperature. Using the *in situ* images that were taken in parallel to the Bragg scattered images, the global temperature and the homogeneous density can be determined as described in sections 3.5 and 3.6 to yield  $T/T_F(z)$ . We can therefore plot  $\tilde{\chi}''(k, \omega/2, z)$  versus  $T/T_F(z)$ . In figure 5.7, the four clouds that were shown in figure 5.6 are now plotted in this manner.

For the three clouds where the local temperature decreases below  $T_C = 0.167T_F$  [80], we notice that the homogeneous response increases sharply. As the density-density response is also dependent on the momentum  $k$ , it is necessary to relate the response to the local Fermi wave vector  $k/k_F$  as well, where  $k_F = \sqrt{2m\epsilon_F}/\hbar$ . We perform this same measurement for 16 different temperature clouds, where data for each cloud is an average of 30 shots, and build up a two-dimensional image of the homogeneous response versus local temperature and local wavevector.

Figure 5.8 shows this response of  $\omega_r/2$  which is relatively flat for temperatures above  $T_C$  with a fairly weak dependence on the wavevector; however when the temperature drops below  $T/T_F \approx 0.2$ , we observe a sharp increase in  $\chi''$  indicating the buildup of zero momentum pairs in the gas. The white dashed lines show the range of  $T/T_F$  and  $k/k_F$  spanned by each different temperature cloud used to build this image. The data

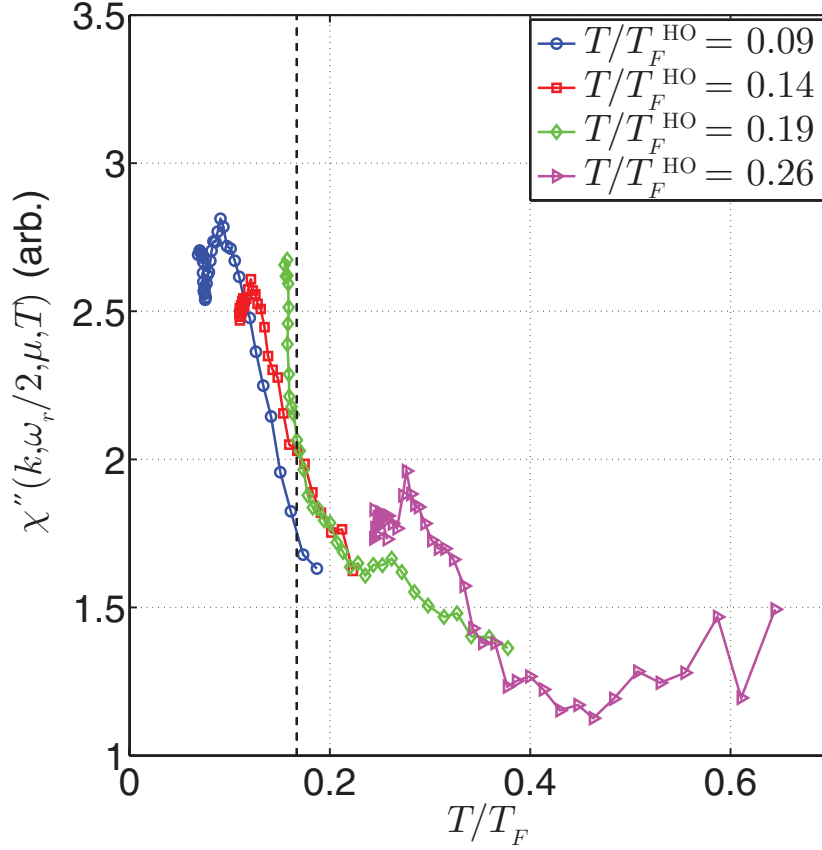


Figure 5.7: Homogeneous response versus local temperature for the four clouds shown before. The vertical dashed line represents the superfluid phase transition  $T_C = 0.167T_F$  [80].

is averaged into bins along  $T/T_F$  and  $k/k_F$  to reduce the noise. The grey shaded area of the image ( $4.5 < k/k_F < 5.5$ ) is an area we have selected to generate figure 5.9 for a clearer way to see the  $T/T_F$  dependence. As a side note, we did generate plots using other ranges of  $k/k_F$  with similar results, however the range we have selected has a considerable number of data points both above and below  $T_C$ .

The data above and below  $T_C$  are approximately linear so therefore fits are made to the two phases of the response data in figure 5.9. One fit spans data ranging  $0.11 < T/T_F < 0.17$  and the other fit ranges  $0.2 < T/T_F < 0.6$ . The point where these fits intersect gives us an estimate for the critical temperature for pair-condensation, which comes out to be  $T_C = 0.18^{+0.03}_{-0.02}T_F$ . This value for the critical temperature

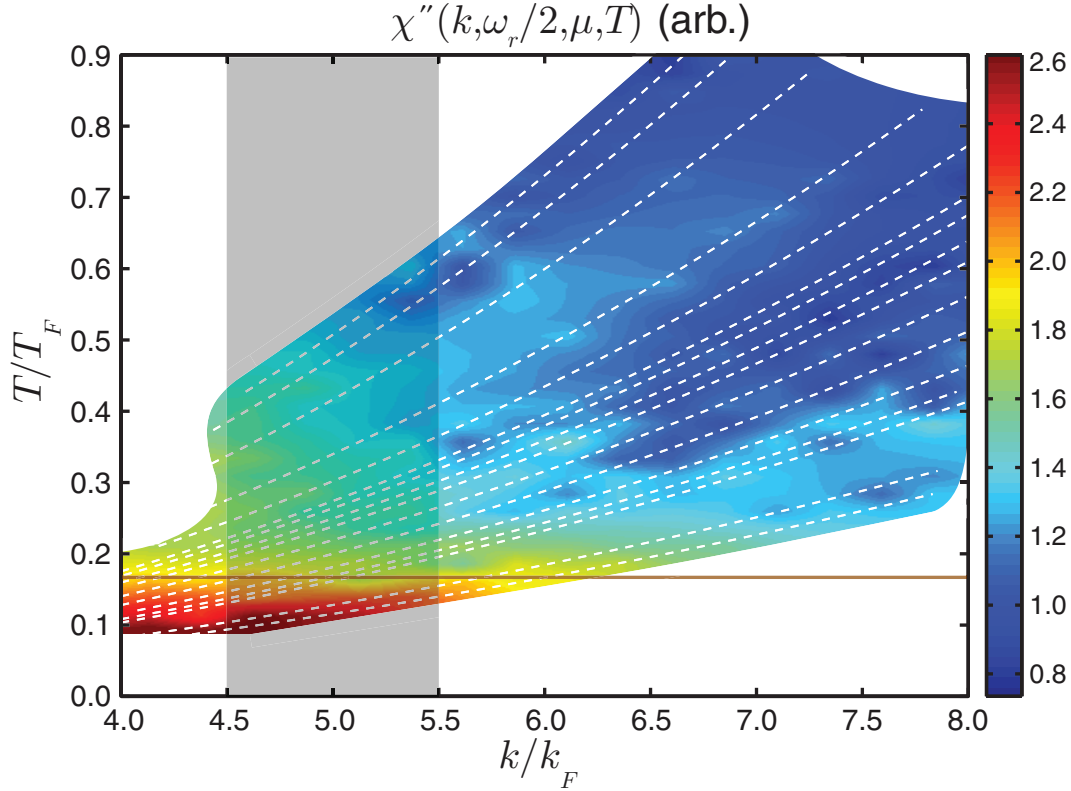


Figure 5.8: Homogeneous response versus local temperature and local wavevector. The white dashed lines represent data contributed by each individual cloud. The brown solid line is the superfluid phase transition  $T_C = 0.167T_F$ . The grey shaded area is used to generate figure 5.9

for pair-condensation is in good agreement with the superfluid transition temperature of  $T_C = 0.167T_F$  [80], which is consistent with the fact that pair-condensation and superfluidity occur simultaneously in a 3D Fermi gas. Uncertainties in this measurement arise due to the finite slice width which necessarily averages over a small range of varying densities within a slice. The short time of flight also means that atoms will diverge along the  $z$ -direction in an interacting gas due to elastic collisions. These two effects are taken into account in the error bars.

Also shown in figure 5.9 is the calculated response of an ideal gas at the same  $T/T_F$ . This is found by calculating the momentum distribution,  $n(\mathbf{p})$ , of an ideal gas for finite temperatures, and then using the impulse approximation which holds for inelastic scattering at high momentum [151], to determine  $S(k, \omega_r/2)$ . This is then convoluted

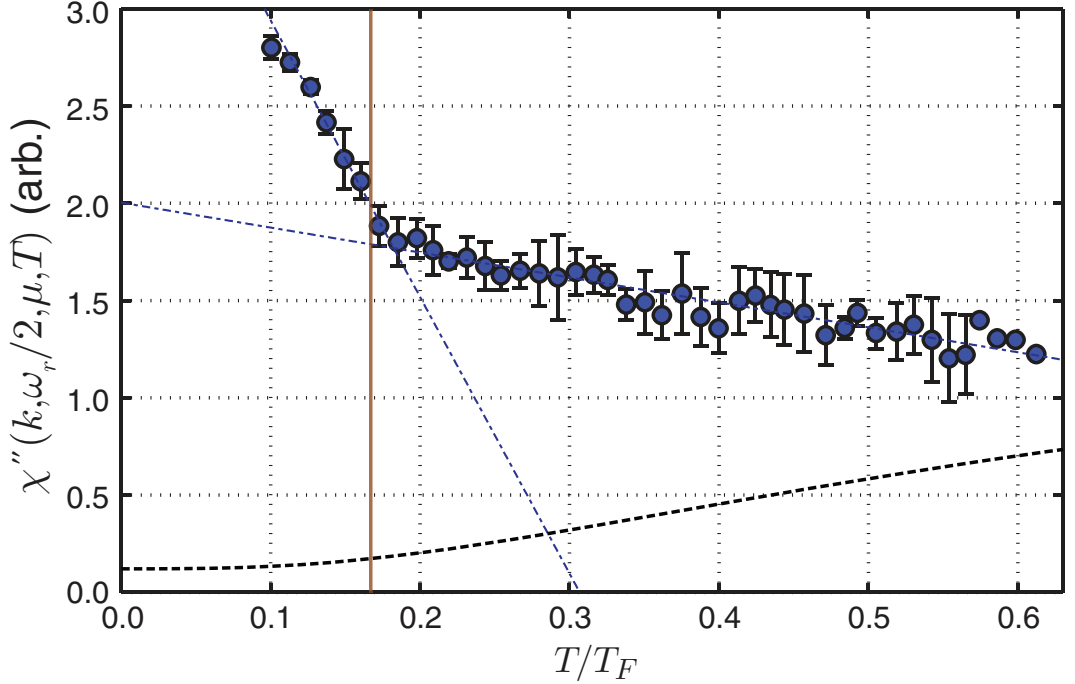


Figure 5.9: Homogeneous response versus local temperature for  $4.5 < k/k_F < 5.5$ . The brown solid line is the superfluid phase transition  $T_C = 0.167$  [80]. The black dashed line shows non-interacting data for a wave vector of  $5k_F$ . The dash-dotted blue lines are linear fits to the data in the two different phases.

with the Fourier transform of the  $200 \mu\text{s}$  Bragg pulse to arrive at a prediction for the measured response. It is interesting to note that above  $T_C$ , the homogeneous response has the opposite temperature dependence to the ideal gas. For higher temperatures the response due to the scattering of single atoms will also be playing a role at  $\omega_r/2$  as interactions enhance short-range density-density correlations. Thus, we cannot say whether this temperature dependence indicates the presence of preformed pairs. For this we would need a way to observe that pairing gap which is possible at low- $k$ .

## 5.7 Summary

The onset of pair-condensation has been observed *in situ* using local measurements on a Bragg scattered cloud at the pairing peak. A scheme for extracting the homogeneous density-density response from the density-weighted response was derived, which

extended a previous method used to extract the homogeneous pressure and density from the doubly-integrated density [82, 83]. This scheme can be used to obtain homogeneous information from any local measurement, including dynamic variables that satisfy the local density approximation. Comparing the homogeneous response to the local temperature, a sudden increase is observed in the response below  $T_C$ , indicating a sudden increase in the number of pairs with zero centre-of-mass momentum which is a definitive signature of pair-condensation.

# Chapter 6

## Temperature dependence of the trap-averaged contact

### 6.1 Introduction

From a theoretical point of view, calculating certain parameters in a strongly interacting Fermi gas comes with great difficulty because simple perturbation theory is no longer valid. One such parameter is the contact, described previously section 2.6 of this thesis and first derived in [39–41]. The contact describes the likelihood of finding a spin-up particle close to a spin-down particle within a system, yet it also contains information on the bulk thermodynamics through a number of exact relations [42, 43, 47, 55]. Several theoretical calculations have been performed in an effort to measure the contact parameter, however the results of these vary by up to 10% [50, 57, 58, 60, 61]

In the past, several different measurements have been performed to find the contact for a harmonically trapped cloud by employing various methods. These include measuring the amplitude of the high momentum tail of the momentum distribution, measuring the high frequency tail in an RF spectrum [68], the number of closed channel molecules [64, 65], measuring the frequency of collective oscillations [66, 67], measuring the total energy of the system throughout the crossover [72], and finding the high momentum spin-antiparallel static structure factor [35] using Bragg spectroscopy. The last method has yielded the most accurate result with a 3% error for a cold Fermi gas

with a temperature  $T/T_F^{\text{HO}} = 0.08$  [63]. This same method is employed again to obtain the results shown in this chapter, where we present precise measurements of the contact parameter for trapped clouds at higher temperatures and work towards building up a curve showing its temperature dependence, which can serve as a meaningful benchmark for comparison with different theoretical calculations.

## 6.2 Method

The aim here is to find the contact from the structure factors which can be derived from a Bragg spectrum. With this measurement, we cannot simply Bragg scatter a cloud with any pulse and expect to get meaningful information from the consequential density response. Care must be taken to ensure that we are actually measuring the linear response. With a Bragg pulse that has a high intensity or a long duration, atoms may begin to Rabi cycle between the initial and final momentum states. Bragg scattering atoms out of the cloud depletes the cloud itself, and therefore changes its properties. In these measurements we want this effect to be negligible. Here, we use a Bragg pulse of around  $50 \mu\text{s}$  as it is very short compared to a quarter of a trap period ( $\sim 7 \text{ ms}$ ). Therefore, the power of the Bragg beams must be limited so that the response for this pulse duration is still linear. As shown in equation 4.17, the response is dependent on the two-photon Rabi frequency,  $\Omega_R$ , which in turn is dependent on the product of the beam intensities  $I_1 I_2$ . This necessitates performing some calibration measurements in order to establish the linear response regime experimentally.

In this measurement the response due to the Bragg pulse,  $\Delta X(\omega)$ , is quantified using the methods shown in subsection 4.2.2 and measured against the Bragg intensity,  $I_1 I_2$ . For an ideal gas, this measurement would reveal Rabi oscillations and the linear response region would occur at low Bragg intensities where the beginning of the cycle is approximately linear. In this region, the gas has not yet been depleted of atoms in their initial momentum state significantly, thus allowing us to gain information on the initial state of the system. For the strongly interacting gas, the interactions within the timescale of the Bragg pulse have a heavy damping effect on the Rabi cycles via collisional decoherence, but the response will still deviate from linearity at higher Bragg intensities.

Three main features within a Bragg spectrum are identified as key areas to explore their linearity: these are the pairing peak at  $\omega_r/2$ , the atomic peak at  $\omega_r$  and the high frequency tail at  $2\omega_r$ . The reason both of the peaks are selected is because the strongest response comes at those frequencies as well as being where the probe depletes the cloud at the fastest rate, therefore we expect to see the response decrease away from linearity for lower Bragg intensities at these frequencies, placing an upper limit on the intensity product we use for other Bragg frequencies near these features. Also, pairs and single atoms couple differently to the Bragg lasers as pairs have twice the polarisability of individual atoms and couple twice as strongly to the Bragg light. The tail has its own linearity check because the signal is small and the response is far weaker, so we can afford to kick the clouds with a higher Bragg intensity to increase the signal to noise. For each of these three frequencies, the response is measured against  $I_1 I_2 / I_{\text{sat}}^2$  (where  $I_{\text{sat}} = 2.54 \text{ mW/cm}^2$  is the saturation intensity) in order to get an idea of where the linear regime cuts off. This is shown in figure 6.1.

The blue circles are data for the response for a Bragg frequency of  $\omega_r/2$ . For low values of the intensity product, the response has a rough linear relationship up until  $I_1 I_2 / I_{\text{sat}}^2 \approx 0.008$  as indicated by the blue dashed line, which is a linear fit to the first few data points. Above this value, the response decreases with respect to the linear fit meaning that the initial state has been significantly depleted. For that reason, our Bragg measurements at frequencies around the pairing peak will have a limited probe intensity below  $I_1 I_2 / I_{\text{sat}}^2 \approx 0.008$ . The red squares show the linearity check for  $\omega = \omega_r$  and the red dot-dashed line is the linear fit. This shows that the response is linear up to  $I_1 I_2 / I_{\text{sat}}^2 \approx 0.013$ , which is a slightly higher intensity than the linearity check at the pairing peak. This is in part due to the fact that molecules have twice the polarisability of free atoms. It should be noted that for both peaks, the response never turns around and shows Rabi cycling due to the elastic collisions in this strongly interacting cloud which leads to decoherence (i.e. atoms changing their momentum). It was shown in the supplemental material of [152] that for a cloud with weaker interactions in the BEC regime, a similar measurement on the pairing peak reveals these Rabi oscillations for one or two cycles before the damping due to collisions take over. Lastly, the green triangles in figure 6.1 show the response at  $\omega = 2\omega_r$ . Since it is far away from any resonance, the response is significantly smaller and the linear regime is deemed to range up to

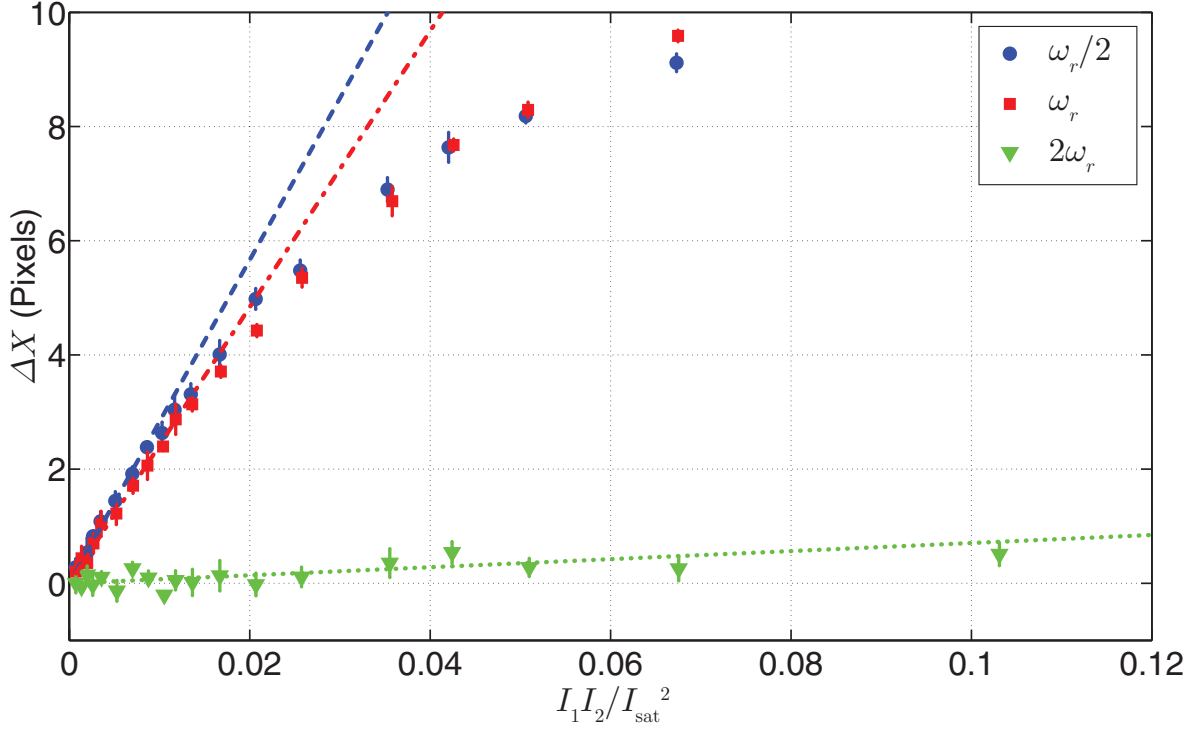


Figure 6.1: Response in pixels measured against intensity product of the probe. The intensity product is in units of  $I_{\text{sat}}^2$ . The blue circles are data for a Bragg frequency of  $\omega = \omega_r/2$ , the red squares are for  $\omega = \omega_r$  and the green triangles are for  $\omega = 2\omega_r$ . The straight lines are fits to the linear response regions. The blue dashed line is the fit to the data for a Bragg frequency of  $\omega = \omega_r/2$  up to  $I_1 I_2 / I_{\text{sat}}^2 \approx 0.008$ , the red dot-dashed line is for a Bragg frequency of  $\omega = \omega_r$  up to  $I_1 I_2 / I_{\text{sat}}^2 \approx 0.013$ , and the green dotted line is for a Bragg frequency of  $\omega = 2\omega_r$  up to  $I_1 I_2 / I_{\text{sat}}^2 \approx 0.026$ .

$I_1 I_2 / I_{\text{sat}}^2 \approx 0.026$  as indicated by the fit shown by the green dotted line.

As summarised in table 6.2, when measuring a Bragg spectrum, the Bragg frequencies are divided into four separate sets in which a certain Bragg intensity is used to maximise the signal in each set, yet ensured through the linearity checks that we are measuring the linear response. Recalling that the atomic resonance is  $\omega_r/2\pi = 131.7$  kHz, the spectral points around the pairing peak in set 1 use an intensity product,  $I_1 I_2 / I_{\text{sat}}^2 \approx 0.008$ , as given from the linearity check in figure 6.1. This same argument is applied to the other data sets, except for set 3 where we introduced an additional range because it was found that the Bragg frequencies that lie far enough from  $\omega_r$  could use a slightly higher intensity while staying in the linear regime.

Set	Bragg Frequency's (kHz)	Step Size (kHz)	Intensity Product ( $I_1 I_2 / I_{\text{sat}}^2$ )
1	0→60, 65, 70→110	10	≈0.008
2	0, 120→210	10	≈0.013
3	0, 220→250	10	≈0.015
4	0, 260→360	20	≈0.026

Table 6.1: This table shows which Bragg frequencies contribute to the spectra shown later in this chapter as well as the Bragg intensity for each frequency. Where there are →'s in the column that is second from the left, the step size is indicated in the next column over. Just as a reminder, the atomic resonance is  $\omega_r/2\pi = 131.7$  kHz.

For each set, there are also shots taken at  $\omega = 0$  in order to provide a reference shot for the given intensity product. The Bragg frequency is swept from shot to shot per set in an ascending order until the final Bragg frequency of the set, and then swept back down in a descending order to restrict any effects of long term experimental drift in the cloud position. All up, there are around 15 shots taken at each Bragg frequency. Throughout the entire data collection phase, some images are also taken of the unperturbed gas *in situ* to determine the atom number and the temperature of the clouds and make sure those parameters remain consistent. To image Bragg scattered clouds, we use an imaging pulse duration of  $5 \mu\text{s}$  with an intensity  $0.8I_{\text{sat}}$  to avoid systematics whereas the *in situ* shots use a shorter pulse length of  $1 \mu\text{s}$  and a much higher intensity  $14I_{\text{sat}}$ . The Bragg pulse duration of  $50 \mu\text{s}$  is actually shorter than other Bragg measurements from our laboratory. Because measuring the contact involves integrating across all  $\omega$ , we can afford to shorten the Bragg pulse duration without the worry of spectral broadening (provided all measurements are performed in the same way) as the relative area under each spectrum should still be preserved. This also minimises the heating of the cloud during the pulse. Once all the images have been taken, the centre-of-mass displacement per Bragg frequency,  $\Delta X(\omega)$  (equation 4.8), can be calculated as described in depth in chapter 4. Because we are confident that each cloud in the spectrum has been probed in the linear response region, each  $\Delta X(\omega)$  is then divided by the intensity product,  $I_1 I_2$ , used to probe it so that responses from each different set can be combined on a single plot.

### 6.3 Measured structure factors

The identities for the static and dynamic structure factors in subsection 4.3.1 are put to practical use when analysing a Bragg spectrum. Having measured  $\Delta X(\omega)$  across a range of  $\omega$ , we know this is proportional to the dynamic structure factor meaning that  $\Delta X(\omega) = A_{\text{Bragg}} S(k, \omega)$ , where  $A_{\text{Bragg}}$  is a constant that encapsulates all of the experimental parameters that determine the actual centre-of-mass displacement. Such parameters include the Bragg laser intensity  $I_1 I_2$ , the time of flight of the cloud between the Bragg pulse and imaging pulse, the momentum transferred,  $\hbar k$ , and the detuning of the Bragg beams from the resonant transition. Starting off with the following two equations:

$$\int \Delta X(\omega) d\omega = A_{\text{Bragg}} \int S(k, \omega) d\omega, \quad (6.1)$$

and

$$\int \omega \Delta X(\omega) d\omega = A_{\text{Bragg}} \int \omega S(k, \omega) d\omega, \quad (6.2)$$

we can divide equation 6.1 by 6.2, and then substitute the  $f$ -sum rule in equation 4.45 as well as equation 4.31. We then have

$$\frac{\int \Delta X(\omega) d\omega}{\int \omega \Delta X(\omega) d\omega} = \frac{A_{\text{Bragg}} N S(k)}{A_{\text{Bragg}} N \hbar k^2 / 2m} = \frac{S(k)}{\omega_r}, \quad (6.3)$$

which eliminates the need to know anything about the parameters of the experiment that go into the constant  $A_{\text{Bragg}}$ , or even the atom number to find the static structure factor. The one exception to this is the Bragg recoil frequency,  $\omega_r$ , which can be accurately measured either by measuring the angle between the two Bragg beams and applying equations 4.1 and 4.2, or measuring the Bragg spectrum of an ideal gas and finding the frequency that corresponds to the peak [123]. The static and dynamic structure factor in the context of Bragg scattering are therefore given as

$$S(k) = \frac{\omega_r \int \Delta X(\omega) d\omega}{\int \omega \Delta X(\omega) d\omega}, \quad (6.4)$$

$$\frac{S(k, \omega)}{N} = \frac{\omega_r \Delta X(\omega)}{\int \omega \Delta X(\omega) d\omega}. \quad (6.5)$$

These structure factor identities work when using a response measurement due to the momentum transferred  $\Delta X(\omega)$ . As a side note, if the measured response were to come from the energy transferred  $\Delta\sigma^2(\omega)$  from equation 4.7, the dynamic structure factor is then equal to

$$\frac{S(k, \omega)}{N} = \frac{\omega_r \Delta\sigma^2(\omega)}{\omega \int \Delta\sigma^2(\omega) d\omega}. \quad (6.6)$$

Figure 6.2 shows dynamic structure factors for six different temperature clouds ranging below and above the critical temperature for a trap-averaged cloud  $T_C^{\text{HO}} \approx 0.22T_F^{\text{HO}}$ .  $T_C^{\text{HO}}$  indicates the temperature at which superfluid starts to form, i.e. where the local temperature in the cloud centre goes below the  $T_C$  [80]. The temperature of the gas is controlled by varying the evaporation endpoint and quantified by fitting the local pressure found in the *in situ* images to the equation of state measured in [80] as described in section 3.6. Because the Bragg pulse duration is shorter than previous experiments, the Fourier width is increased, which causes the peaks to shift slightly, weighting towards frequencies with higher responses as well as decreasing the height of the narrow pairing peak, and broadening. Despite these spectra being trap-averaged, we observe that the peak around  $\omega_r/2$  still appears to be at least a good signature for pair-condensation towards the centre of the cloud where the local temperature is still lower than  $T_C$  [1].

Before the first moment,  $\langle x \rangle_{\text{Image}}$  (equation 4.4), of an imaged cloud is calculated an appropriate region of interest is taken to include the entire cloud but leave out as much of the background as possible. Once the centre-of-mass is calculated within this region, the region is then varied several times and the centre-of-mass is calculated for each region.  $\langle x \rangle_{\text{Image}}$  is taken as the average of all of these centre-of-masses. The reasoning behind calculating  $\langle x \rangle_{\text{Image}}$  in this way is because there is noise in the background of each image and considering the fact that we want to resolve some values of  $\Delta X(\omega)$  that are less than a pixel, this noise can become relevant. Changing the regions of interest in this manner and then averaging will help to average over any contribution due to noise in the background of the image. The variation in the first moment due to the noise contributes to the error bars shown in figure 6.2. Another factor contributing to the error bars is the shot-to-shot variations which includes minor fluctuations in the initial position of the cloud. Lastly, the calculated centre-of-mass displacement and error bars

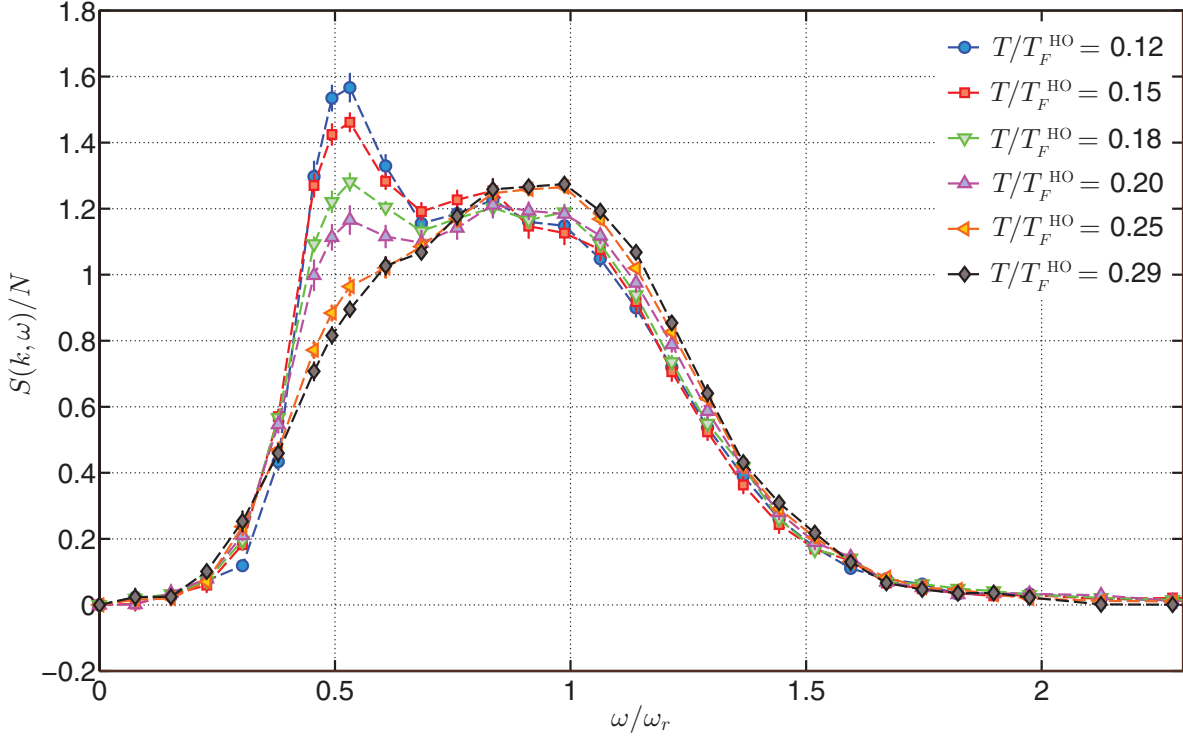


Figure 6.2: Dynamic structure factors plotted against the normalised Bragg frequency for a range of different bulk temperatures above and below the critical temperature ( $T_C^{\text{HO}} = 0.22T_F^{\text{HO}}$ ). Temperatures include  $T = 0.12T_F^{\text{HO}}$  (blue circles),  $T = 0.15T_F^{\text{HO}}$  (red squares),  $T = 0.18T_F^{\text{HO}}$  (green downward-pointing triangles),  $T = 0.20T_F^{\text{HO}}$  (violet upward-pointing triangles),  $T = 0.25T_F^{\text{HO}}$  (orange left-pointing triangles),  $T = 0.29T_F^{\text{HO}}$  (grey diamonds).

for each Bragg frequency are normalised by the Bragg intensity used for that frequency, which is why the error bars are smaller at higher Bragg frequencies (refer to table 6.2).

Having calculated the dynamic structure factors, the static structure factors can then be calculated by integrating them across all  $\omega$ , which comes from substituting equation 6.5 into equation 6.4:

$$S(k) = \frac{1}{N} \int S(k, \omega) d\omega. \quad (6.7)$$

## 6.4 Trap-averaged contact

The contact can be calculated from the dynamic structure factor in a couple of different ways, one of which comes from observing the high-frequency tail. It is predicted that the dynamic structure factor in the limit of high energy has a universal dependence of  $\lim_{\omega \rightarrow \infty} S(k, \omega) \propto \omega^{-7/2}$  [45, 46, 153]. At high momentum, the contact is contained within the amplitude of the high-frequency tail which is given as [123]

$$\frac{\mathcal{I}}{Nk_F} = \frac{45\pi^2}{16\sqrt{2}} \frac{k}{k_F} \left( \frac{\omega}{\omega_r} \right)^{7/2} \lim_{\omega \rightarrow \infty} S(k, \omega). \quad (6.8)$$

Theoretically, this can be extracted in a similar manner to the way JILA group measured the contact using the power-law dependence in the tail of the spectral function [68]. A correctly predicted power law dependence has been observed previously in a Bragg spectroscopy measurement of the spin-parallel and spin-antiparallel structure factors, where their universal tails are proportional to  $\omega^{-5/2}$  [152]. However for precise measurement of the contact this method is inefficient. In the tail of the dynamic structure factor, the signal is small and susceptible to minor offsets that are difficult to eliminate entirely even after the  $f$ -sum rule normalisation. It is therefore difficult to determine where the universal limit in the high-frequency tail actually begins. Thus, the amplitude coefficients we get from fitting to high-frequency tails are noisy and can vary widely with the inclusion and exclusion of data points.

A more robust method to obtain the contact is through the Tan relation that uses the spin anti-parallel structure factor, shown previously in equation 2.37. The static structure factor is calculated through the use of equation 6.7 and this calculated value is a combination of its spin-parallel and spin anti-parallel components  $S(k) = S_{\uparrow\uparrow}(k) + S_{\uparrow\downarrow}(k)$ . Because the Bragg beams are far detuned from both states ( $\Delta\omega_{\uparrow} \approx \Delta\omega_{\downarrow}$ ) it can be assumed the spin-parallel component of the static structure factor is  $S_{\uparrow\uparrow}(k) \approx 1$  [152]. Physically this implies that the short range correlations between particles of the same spin state are negligible and are dominated by the auto-correlation term. Therefore, the contact can be found with the use of the structure factor Tan relation given in

equation 2.37 which is modified to give

$$\frac{\mathcal{I}}{Nk_F^{\text{HO}}} = \frac{4k}{k_F^{\text{HO}}} \left( \frac{S(k) - 1}{1 - 4/(\pi ak)} \right), \quad (6.9)$$

which at unitarity where  $a \rightarrow \infty$  simplifies to

$$\frac{\mathcal{I}}{Nk_F^{\text{HO}}} = \frac{4k}{k_F^{\text{HO}}} (S(k) - 1). \quad (6.10)$$

One of the advantages of carrying out the contact measurement in this manner is that the entire spectrum is employed, including the lower energy points like the pair and atomic resonances, which in turn have a high signal-to-noise ratio. Also the integration of the dynamic structure factor means that small fluctuations in the signal contribute very little to the overall result.

Figure 6.3 shows the new measurements of the trap-averaged contact versus bulk temperature along with some older experimental data from our group and curves derived from several different strong coupling theories. The blue circles represent the new data points coming from the structure factors shown in figure 6.2. The vertical error bars take into account the errors in the dynamic structure factor as well as shot to shot variations in  $k_F^{\text{HO}}$  arising from its dependence on the atom number. The horizontal error bars also come from atom number fluctuations, because that affects  $T_F^{\text{HO}}$ , as well as the residual error in the absolute temperature of the cloud coming from the thermometry fitting.

Linking these recent measurements (blue circles in Figure 6.3) together with the contact measurement for a cold cloud (red square in Figure 6.3), the new data points lie around the mark compared to the theory curves. As the temperature increases in the range  $0.15 \lesssim T/T_F \lesssim 0.20$ , the contact appears to drop quickly from around  $\mathcal{I}/Nk_F \approx 3$  to around  $\mathcal{I}/Nk_F \approx 2.1$ . However as the temperature goes to above  $T_C^{\text{HO}}$ , the contact appears to flatten off around  $\mathcal{I}/Nk_F \approx 1.9$  for the two data points that we have. The theory curve that appears to agree best with our data around  $T_C^{\text{HO}}$ , is the double dot-dashed line from Zwerger's group [60] which also shows the similar signs of critical behaviour, whereas at colder temperatures our data is similar to the dot-dashed curve from the Swinburne theory group [57].

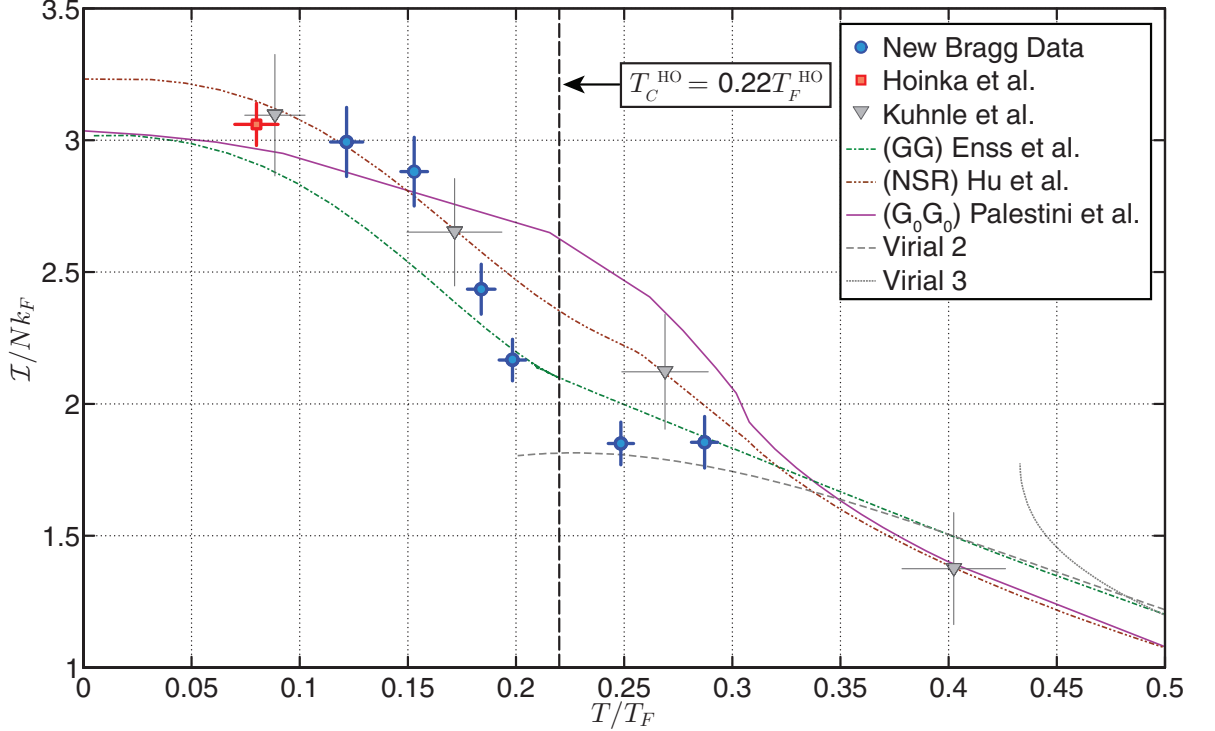


Figure 6.3: Trap-averaged contact versus bulk temperature. The new data obtained for this publication are the blue filled circles. The red square is a low temperature precision measurement from [63]. The grey triangles are data from [35]. The double dot-dashed, dot-dashed and solid curves are calculated from several different strong-coupling theories from publications [57, 58, 60], respectively. The long-dashed and short-dashed curve are the 2nd and 3rd order virial expansion [57]. The vertical black dashed line represents the critical temperature  $T_C^{\text{HO}} = 0.22T_F^{\text{HO}}$ .

## 6.5 Homogeneous contact

This chapter so far has focussed on trap-averaged measurements of the contact, but a natural question one might ask is what happens when the local technique presented in chapter 5 is extended to measure the local contact? Indeed, the data collected and presented so far in this chapter was initially intended for this exact purpose. The idea was to measure the homogeneous density-density response for each value of  $\omega$  in an entire Bragg spectrum using equation 5.6. In doing this, we could then calculate the homogeneous static structure factor, and therefore the homogeneous contact for the range of relative temperatures that the cloud spans. Shown in figure 6.4(a) are our

measurements of the homogeneous contact and these are compared to the homogeneous contact measurements made at JILA [73] in figure 6.4(b). Both of these figures are plotted on the same scale.

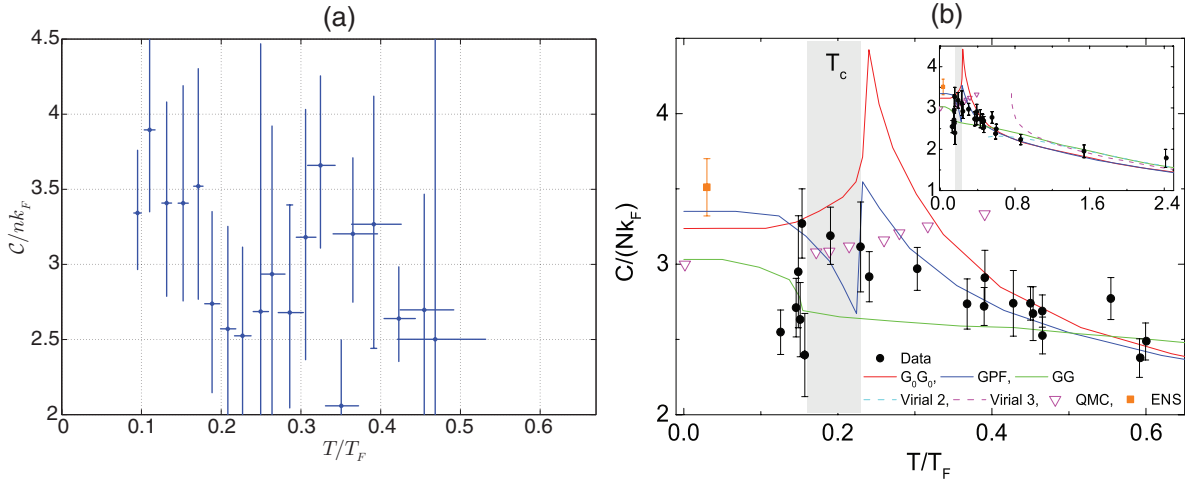


Figure 6.4: (a) Preliminary data for homogeneous contact versus local temperature. (b) Contact measurements on a nearly homogeneous Fermi gas at unitarity versus local temperature taken straight out of [73]. The black circles are the data points measured in [73]. The shaded area represents the uncertainty in the superfluid phase transition (as it was understood at the time of publication [132]). The red, blue and green solid curves are calculated from several different strong-coupling theories from publications [57, 58, 132], respectively. The pink triangles are from a quantum Monte Carlo simulation [62], and the single orange square is the contact calculated from an equation of state measurement along the BCS-BEC crossover [72]. Inset in (b) is the same measurement on a larger  $T/T_F$  scale. The light blue dashed line is the 2nd order virial expansion and the pink dashed line is the 3rd order virial expansion. Reprinted figures with permission from Y. Sagi, T. E. Drake, R. Paudel, and D. S. Jin, “Measurement of the homogeneous contact of a unitary Fermi gas,” *Physical Review Letters* **109**(22), 220402 (2012). Copyright 2015 by the American Physical Society (doi: 10.1103/PhysRevLett.109.220402).

For each cloud, local line spectra,  $\tilde{\chi}''(k, \omega, z)$ , are measured where the slices are binned such that the change in the line density  $\tilde{n}(z)$  is similar for all slices (average bin size is  $\sim 12$  pixels). The homogeneous spectra,  $\chi''(k, \omega, \mu, T)$ , are then calculated using equation 5.6 to obtain a total of five spectra per cloud. The homogeneous dynamic,  $S(k, \omega, \mu, T)$ , and static structure factors,  $S(k, \mu, T)$ , can then be calculated, and know-

ing the local Fermi wavevector at the centre of the slice we evaluate the homogeneous contact  $\mathcal{C}/nk_F$ , which at unitarity is given as

$$\frac{\mathcal{C}(\mu, T)}{nk_F} = \frac{4k}{k_F} (S(k, \mu, T) - 1). \quad (6.11)$$

This procedure is repeated another three times on the same cloud but with varying line density bins across the cloud in order to build up more data points. The local  $T/T_F$  is measured for each data point at the centre of the slice as well. From here, the homogeneous contact data from the six different clouds are then combined and averaged along the temperature scale in steps of  $T = 0.02T_F$  in an attempt to average down the errors, resulting in what is shown in figure 6.4(a). The vertical error bars are determined by the error in  $S(k, \mu, T)$  as well as the variation of density within the slice which affects  $k/k_F$ . By the same token, this variation within the slice affects  $T/T_F$  and hence, the horizontal error bars, which also account for the fit residuals when determining  $T$ .

Comparing our data shown in figure 6.4(a) with the data shown in figure 6.4(b) we can see that our data points lie in a similar range compared to the previous measurement and calculations. However the error bars are considerably larger and therefore we cannot provide meaningful new insights into the behaviour of the homogeneous contact near the superfluid transition at this stage. The reason that large errors arise using this method is because successful calculation of the homogeneous contact requires that the homogeneous structure factors have reasonably small error bars, and this proved to be difficult for multiple reasons. The first is that the homogeneous response can only be measured using the images from state  $|1\rangle$  which has a short time of flight. By the time the state  $|2\rangle$  image is taken, the local information has spread out due to heating and collisions. Therefore no state  $|2\rangle$  correction apart from for the bulk response could be applied. The second reason is that the line profiles,  $n_\omega(x)$ , for a  $\sim 12$  pixel slice have less signal than a line profile from the entire cloud (usually integrated across  $\sim 120$  pixels), meaning the centre-of-mass of these line profiles obtained from the slices also had less signal-to-noise than the bulk measurements. The third reason is that within a Bragg spectrum, there are always regions that have a very low signal (like the early Bragg frequencies and the high-frequency tail), as seen in the bulk measurements.

While applying the derivative in equation 5.6 to obtain the homogeneous response at  $\omega = \omega_r/2$  worked well as shown in chapter 5, this was more of a qualitative procedure in terms of measuring how the response behaved around the critical temperature. Also this measurement was only applied to one Bragg frequency (which has a large signal) which allowed for many shots to be taken and thereby increasing the signal-to-noise ratio. Within the low-signal regions, the centre-of-mass displacement we must resolve accurately could be as low as 5% of a pixel with even smaller errors and that sort of resolution is unrealistic in our system. Given that all of these factors decreased the signal-to-noise ratio, the application of the derivative in equation 5.6 to this data yielded noisy results.

This affected the rest of the measurement as all of these data points were required in the  $f$ -sum rule normalisation, which then increased the error bar of the static structure factor to the point where it could not tell us anything meaningful. Considering the homogeneous contact has already been measured in [73] as shown in figure 6.4(b), our measurements would have to be far more precise to provide a meaningful step forward in our understanding. This problem could possibly be overcome by collecting more data points, however it would take an exorbitant amount of hours of data collecting to get the error bars down to a point where they are useful. On the bright side, the data from this measurement does appear to align approximately with the results shown in figure 6.4(b) within the errors, confirming the principle for other variables.

## 6.6 Summary

Through the use of the structure factor Tan relation, the temperature dependence of the trap-averaged contact parameter has been measured in the unitary Fermi gas. Integrating the dynamic structure factor over all Bragg frequencies is an efficient method of obtaining the static structure factor with relatively low noise. The accuracy of these measurements provides a new benchmark for the contact parameter with error bars small enough to start to discern between previous experimental measurements and theoretical calculations. A measurement of the homogeneous contact was also performed using these clouds. While our data appeared to lie around the mark compared to the

other measurement, the large errors meant that we could not make a meaningful contribution on this topic, but it did prove that the technique that we used for extracting homogeneous dynamic variables in chapter 5 could be applied to extract homogeneous structure factors and hence, the contact.

# Chapter 7

## Conclusion and Outlook

### 7.1 Conclusion

This thesis shows several results that have come about by measuring the dynamic response of unitary Fermi gases at various absolute temperatures. The experimental method of Bragg spectroscopy at high momentum, a technique that has seen prominent use in our laboratory in the past, has gained an extra feather in its metaphorical cap with the ability to measure the homogeneous density-density response function. In a similar way to how the homogeneous atomic density can be extracted from the one-dimensional column density [82], the local density approximation can be applied to a density perturbation due to Bragg scattering. In fact theoretically, the local density approximation can be applied in this manner to any variable, including dynamic variables like RF spectral function and the spin-spin response.

In chapter 5, we used this technique to measure the local Bragg response at the pairing resonance and observed a sudden increase in the response as the local temperature of the cloud decreases below around  $0.18T_F$ . This provided a stark signature of the build up of pairs of opposite spin fermions in the system with zero total momentum. This is a signature for pair-condensation and it appears at a temperature of around  $T = 0.18_{-0.02}^{+0.03}T_F$ , which is well aligned with the superfluid phase transition temperature of  $T = 0.167T_C$  [80].

In chapter 6, we went back to focussing on trap-averaged measurements. The background for this result was that a precision measurement of Tan’s contact parameter was performed in our laboratory a few years ago on a cold ( $T = 0.08T_F^{\text{HO}}$ ) unitary Fermi gas [63]. The error bar in this measurement was small enough to provide meaningful comparison with theory. The atom number calibration for this measurement is shown in chapter 3. Having established how to extract the trap-averaged contact precisely, in chapter 6 we proceeded to perform the same measurement on six different temperature clouds in order to measure the temperature dependence of the contact. This utilised the ability to normalise Bragg spectra using the  $f$ -sum rule for particle conservation to obtain the static structure factor, which can then be used to calculate the contact using the structure factor Tan relation [48]. These new data points shed further light on the temperature dependence of the trap-averaged contact [57, 58, 60].

## 7.2 Outlook

As described in section 6.5, our attempt to measure the local contact by combining the methods shown in both chapters 5 and 6 did not yield the results we were hoping for, as the final error was quite large. Instead, an alternative approach could be used to measure the homogeneous contact by probing the cloud in the centre. The centre of the trapped gas is nearly homogeneous because the atomic density has little variation around this point. Indeed, the measurement of the homogeneous contact that was performed at JILA using RF spectroscopy made a similar assumption [73], backed up by measurements of the momentum distribution of the cloud after its wings were optically pumped with on-resonant donut shaped beams. In our case, we could modify the Bragg beams so they are focussed down to a small waist size at the centre of the atom cloud and the consequential centre-of-mass displacement at the centre can be measured with respect to a cloud exposed to a Bragg pulse at  $\omega = 0$ , or even against the unperturbed wings of the cloud to avoid noise due to fluctuations in the initial cloud position. This eliminates the need to apply any derivatives as the response only arises from atoms near the cloud centre, and thus should be nearly homogeneous. The time of flight for this measurement can be longer to maximise the signal as we will not have to worry about divergent scattering along the  $z$ -direction, as we know exactly

where the atoms have scattered from. As I write this, preliminary measurements are being performed in our laboratory using low momentum Bragg spectroscopy to probe the homogeneous response as has just been described, and this technique has been performing very well. Therefore we believe this should work just as well, if not better for high momentum Bragg spectroscopy, as a larger momentum transfer means a greater signal. By implementing this it should be possible to make precise measurements of the temperature dependence of the homogeneous contact that will serve as a valuable benchmark against which different theoretical techniques can be assessed. We also hope to reveal the expected critical behaviour of the contact near  $T_C$  [55].

# Bibliography

- [1] M. G. Lingham, K. Fenech, S. Hoinka, and C. J. Vale, “Local observation of pair condensation in a Fermi gas at unitarity,” *Physical Review Letters* **112**(10), 100404 (2014).
- [2] M. H. Anderson, J. R. Ensher, M. R. Matthews, C. E. Wieman, and E. A. Cornell, “Observation of Bose-Einstein condensation in a dilute atomic vapour,” *Science* **269**(5221), 198–201 (1995).
- [3] K. B. Davis, M. O. Mewes, M. R. Andrews, N. J. Vandruten, D. S. Durfee, D. M. Kurn, and W. Ketterle, “Bose-Einstein condensation in a gas of sodium atoms,” *Physical Review Letters* **75**(22), 3969–3973 (1995).
- [4] B. DeMarco and D. S. Jin, “Onset of Fermi degeneracy in a trapped atomic gas,” *Science* **285**(5434), 1703–1706 (1999).
- [5] A. G. Truscott, K. E. Strecker, W. I. McAlexander, G. B. Partridge, and R. G. Hulet, “Observation of Fermi pressure in a gas of trapped atoms,” *Science* **291**(5513), 2570–2572 (2001).
- [6] H. Feshbach, “A unified theory of nuclear reactions. II,” *Annals of Physics* **19**(2), 287–313 (1962).
- [7] S. Inouye, M. R. Andrews, J. Stenger, H. J. Miesner, D. M. Stamper-Kurn, and W. Ketterle, “Observation of Feshbach resonances in a Bose-Einstein condensate,” *Nature* **392**(6672), 151–154 (1998).

- [8] J. L. Roberts, N. R. Claussen, J. P. Burke, C. H. Greene, E. A. Cornell, and C. E. Wieman, “Resonant magnetic field control of elastic scattering in cold  $^{85}\text{Rb}$ ,” *Physical Review Letters* **81**(23), 5109–5112 (1998).
- [9] J. Stenger, S. Inouye, M. R. Andrews, H. J. Miesner, D. M. Stamper-Kurn, and W. Ketterle, “Strongly enhanced inelastic collisions in a Bose-Einstein condensate near Feshbach resonances,” *Physical Review Letters* **82**(12), 2422–2425 (1999).
- [10] S. Jochim, M. Bartenstein, A. Altmeyer, G. Hendl, C. Chin, J. H. Denschlag, and R. Grimm, “Pure gas of optically trapped molecules created from fermionic atoms,” *Physical Review Letters* **91**(24), 240402 (2003).
- [11] J. Cubizolles, T. Bourdel, S. J. J. M. F. Kokkelmans, G. V. Shlyapnikov, and C. Salomon, “Production of long-lived ultracold  $\text{Li}_2$  molecules from a Fermi gas,” *Physical Review Letters* **91**(24), 240401 (2003).
- [12] D. S. Petrov, C. Salomon, and G. V. Shlyapnikov, “Weakly bound dimers of fermionic atoms,” *Physical Review Letters* **93**(9), 090404 (2004).
- [13] L. N. Cooper, “Bound electron pairs in a degenerate Fermi gas,” *Physical Review* **104**(4), 1189–1190 (1956).
- [14] J. Bardeen, L. N. Cooper, and J. R. Schrieffer, “Theory of superconductivity,” *Physical Review* **108**(5), 1175–1204 (1957).
- [15] H. Hu, P. D. Drummond, and X. J. Liu, “Universal thermodynamics of strongly interacting Fermi gases,” *Nature Physics* **3**(7), 469–472 (2007).
- [16] M. Greiner, C. A. Regal, and D. S. Jin, “Emergence of a molecular Bose-Einstein condensate from a Fermi gas,” *Nature* **426**(6966), 537–540 (2003).
- [17] S. Jochim, M. Bartenstein, A. Altmeyer, G. Hendl, S. Riedl, C. Chin, J. H. Denschlag, and R. Grimm, “Bose-Einstein condensation of molecules,” *Science* **302**(5653), 2101–2103 (2003).
- [18] C. A. Regal, M. Greiner, and D. S. Jin, “Observation of resonance condensation of fermionic atom pairs,” *Physical Review Letters* **92**(4), 040403 (2004).

- [19] M. W. Zwierlein, J. R. Abo-Shaeer, A. Schirotzek, C. H. Schunck, and W. Ketterle, “Vortices and superfluidity in a strongly interacting Fermi gas,” *Nature* **435**(7045), 1047–1051 (2005).
- [20] C. Chin, M. Bartenstein, A. Altmeyer, S. Riedl, S. Jochim, J. H. Denschlag, and R. Grimm, “Observation of the pairing gap in a strongly interacting Fermi gas,” *Science* **305**(5687), 1128–1130 (2004).
- [21] C. H. Schunck, Y. Shin, A. Schirotzek, M. W. Zwierlein, and W. Ketterle, “Pairing without superfluidity: The ground state of an imbalanced Fermi mixture,” *Science* **316**(5826), 867–870 (2007).
- [22] Y. Shin, C. H. Schunck, A. Schirotzek, and W. Ketterle, “Tomographic RF spectroscopy of a trapped Fermi gas at unitarity,” *Physical Review Letters* **99**(9), 090403 (2007).
- [23] C. H. Schunck, Y. I. Shin, A. Schirotzek, and W. Ketterle, “Determination of the fermion pair size in a resonantly interacting superfluid,” *Nature* **454**(7205), 739–743 (2008).
- [24] L. Vanhove, “Correlations in space and time and Born approximation scattering in systems of interacting particles,” *Physical Review* **95**(1), 249–262 (1954).
- [25] P. C. Hohenberg and P. M. Platzman, “High-energy neutron scattering from liquid  $\text{He}^4$ ,” *Physical Review* **152**(1), 198–200 (1966).
- [26] R. Cowley and A. Woods, “Inelastic scattering of thermal neutrons from liquid helium,” *Canadian Journal of Physics* **49**(2), 177–200 (1971).
- [27] P. Martel, E. C. Svensson, A. D. B. Woods, V. F. Sears, and R. A. Cowley, “Neutron scattering from superfluid helium at large momentum transfers,” *Journal of Low Temperature Physics* **23**(3-4), 285–301 (1976).
- [28] T. R. Sosnick, W. M. Snow, and P. E. Sokol, “Deep-inelastic neutron scattering from liquid  $^4\text{He}$ ,” *Physical Review B* **41**(16), 11185–11202 (1990).
- [29] A. Griffin, *Excitations in a Bose-condensed Liquid*, Cambridge University Press (1993).

## Bibliography

---

- [30] V. F. Sears, E. C. Svensson, P. Martel, and A. D. B. Woods, “Neutron-scattering determination of the momentum distribution and the condensate fraction in liquid  $^4\text{He}$ ,” *Physical Review Letters* **49**(4), 279–282 (1982).
- [31] W. M. Snow, Y. Wang, and P. E. Sokol, “Density and temperature dependence of the condensate fraction in liquid  $^4\text{He}$ ,” *EPL (Europhysics Letters)* **19**(5), 403 (1992).
- [32] J. Stenger, S. Inouye, A. P. Chikkatur, D. M. Stamper-Kurn, D. E. Pritchard, and W. Ketterle, “Bragg spectroscopy of a Bose-Einstein condensate,” *Physical Review Letters* **82**(23), 4569–4573 (1999).
- [33] R. Combescot, S. Giorgini, and S. Stringari, “Molecular signatures in the structure factor of an interacting Fermi gas,” *Europhysics Letters* **75**(5), 695–701 (2006).
- [34] G. Veeravalli, E. Kuhnle, P. Dyke, and C. J. Vale, “Bragg spectroscopy of a strongly interacting Fermi gas,” *Physical Review Letters* **101**(25), 250403 (2008).
- [35] E. D. Kuhnle, S. Hoinka, P. Dyke, H. Hu, P. Hannaford, and C. J. Vale, “Temperature dependence of the universal contact parameter in a unitary Fermi gas,” *Physical Review Letters* **106**(17), 170402 (2011).
- [36] H. Heiselberg, “Fermi systems with long scattering lengths,” *Physical Review A* **63**(4), 043606 (2001).
- [37] T. L. Ho, “Universal thermodynamics of degenerate quantum gases in the unitarity limit,” *Physical Review Letters* **92**(9), 090402 (2004).
- [38] S. Tan, *Energetics of a strongly correlated Fermi gas*, arXiv:0505200 (2005).
- [39] S. Tan, “Energetics of a strongly correlated Fermi gas,” *Annals of Physics* **323**(12), 2952–2970 (2008).
- [40] S. Tan, “Large momentum part of a strongly correlated Fermi gas,” *Annals of Physics* **323**(12), 2971–2986 (2008).
- [41] S. Tan, “Generalized virial theorem and pressure relation for a strongly correlated Fermi gas,” *Annals of Physics* **323**(12), 2987–2990 (2008).

- [42] E. Braaten and L. Platter, “Exact relations for a strongly interacting Fermi gas from the operator product expansion,” *Physical Review Letters* **100**(20), 205301 (2008).
- [43] S. Z. Zhang and A. J. Leggett, “Universal properties of the ultracold Fermi gas,” *Physical Review A* **79**(2), 023601 (2009).
- [44] R. Combescot, F. Alzetto, and X. Leyronas, “Particle distribution tail and related energy formula,” *Physical Review A* **79**(5), 053640 (2009).
- [45] E. Taylor and M. Randeria, “Viscosity of strongly interacting quantum fluids: Spectral functions and sum rules,” *Physical Review A* **81**(5), 053610 (2010).
- [46] D. T. Son and E. G. Thompson, “Short-distance and short-time structure of a unitary Fermi gas,” *Physical Review A* **81**(6), 063634 (2010).
- [47] E. Braaten, D. Kang, and L. Platter, “Short-time operator product expansion for RF spectroscopy of a strongly interacting Fermi gas,” *Physical Review Letters* **104**(22), 223004 (2010).
- [48] H. Hu, X. J. Liu, and P. D. Drummond, “Static structure factor of a strongly correlated Fermi gas at large momenta,” *Europhysics Letters* **91**(2), 20005 (2010).
- [49] M. Iskin, “Isothermal-sweep theorems for ultracold quantum gases in a canonical ensemble,” *Physical Review A* **83**(3), 033613 (2011).
- [50] Y. Nishida, “Probing strongly interacting atomic gases with energetic atoms,” *Physical Review A* **85**(5), 053643 (2012).
- [51] F. Werner and Y. Castin, “General relations for quantum gases in two and three dimensions: Two-component fermions,” *Physical Review A* **86**(1), 013626 (2012).
- [52] F. Werner and Y. Castin, “General relations for quantum gases in two and three dimensions. II. Bosons and mixtures,” *Physical Review A* **86**(5), 053633 (2012).
- [53] E. Braaten, *Universal relations for fermions with large scattering length*, The BCS-BEC crossover and the unitary Fermi gas, Springer (2012).

- [54] M. DelloStritto and T. N. De Silva, “Tan’s universal contact and collective oscillations of strongly interacting Fermi gases,” *Physics Letters A* **376**(34), 2298–2305 (2012).
- [55] Y. Y. Chen, Y. Z. Jiang, X. W. Guan, and Q. Zhou, “Critical behaviours of contact near phase transitions,” *Nature Communications* **5**, 5140 (2014).
- [56] P. Nozières and S. Schmitt-Rink, “Bose condensation in an attractive fermion gas - from weak to strong coupling superconductivity,” *Journal of Low Temperature Physics* **59**(3-4), 195–211 (1985).
- [57] H. Hu, X. J. Liu, and P. D. Drummond, “Universal contact of strongly interacting fermions at finite temperatures,” *New Journal of Physics* **13**, 035007 (2011).
- [58] F. Palestini, A. Perali, P. Pieri, and G. C. Strinati, “Temperature and coupling dependence of the universal contact intensity for an ultracold Fermi gas,” *Physical Review A* **82**(2), 021605 (2010).
- [59] R. Haussmann, M. Punk, and W. Zwerger, “Spectral functions and RF response of ultracold fermionic atoms,” *Physical Review A* **80**(6), 063612 (2009).
- [60] T. Enss, R. Haussmann, and W. Zwerger, “Viscosity and scale invariance in the unitary Fermi gas,” *Annals of Physics* **326**(3), 770–796 (2011).
- [61] S. Gandolfi, K. E. Schmidt, and J. Carlson, “BEC-BCS crossover and universal relations in unitary Fermi gases,” *Physical Review A* **83**(4), 041601 (2011).
- [62] J. E. Drut, T. A. Lähde, and T. Ten, “Momentum distribution and contact of the unitary Fermi gas,” *Physical Review Letters* **106**(20), 205302 (2011).
- [63] S. Hoinka, M. Lingham, K. Fenech, H. Hu, C. J. Vale, J. E. Drut, and S. Gandolfi, “Precise determination of the structure factor and contact in a unitary Fermi gas,” *Physical Review Letters* **110**(5), 055305 (2013).
- [64] G. B. Partridge, K. E. Strecker, R. I. Kamar, M. W. Jack, and R. G. Hulet, “Molecular probe of pairing in the BEC-BCS crossover,” *Physical Review Letters* **95**(2), 020404 (2005).

- [65] F. Werner, L. Tarruell, and Y. Castin, “Number of closed-channel molecules in the BEC-BCS crossover,” *European Physical Journal B* **68**(3), 401–415 (2009).
- [66] Y. Li and S. Stringari, “Universal contact and collective excitations of a strongly interacting Fermi gas,” *Physical Review A* **84**(2), 023628 (2011).
- [67] A. Altmeyer, S. Riedl, C. Kohstall, M. J. Wright, R. Geursen, M. Bartenstein, C. Chin, J. H. Denschlag, and R. Grimm, “Precision measurements of collective oscillations in the BEC-BCS crossover,” *Physical Review Letters* **98**(4), 040401 (2007).
- [68] J. T. Stewart, J. P. Gaebler, T. E. Drake, and D. S. Jin, “Verification of universal relations in a strongly interacting Fermi gas,” *Physical Review Letters* **104**(23), 235301 (2010).
- [69] J. T. Stewart, J. P. Gaebler, and D. S. Jin, “Using photoemission spectroscopy to probe a strongly interacting Fermi gas,” *Nature* **454**(7205), 744–747 (2008).
- [70] G. E. Astrakharchik, J. Boronat, E. Krotscheck, and T. Lichtenegger, “Dynamic structure function of a cold Fermi gas at unitarity,” *Journal of Physics: Conference Series* **529**(1), 012009 (2014).
- [71] E. D. Kuhnle, H. Hu, X. J. Liu, P. Dyke, M. Mark, P. D. Drummond, P. Hanford, and C. J. Vale, “Universal behavior of pair correlations in a strongly interacting Fermi gas,” *Physical Review Letters* **105**(7), 070402 (2010).
- [72] N. Navon, S. Nascimbene, F. Chevy, and C. Salomon, “The equation of state of a low-temperature Fermi gas with tunable interactions,” *Science* **328**(5979), 729–732 (2010).
- [73] Y. Sagi, T. E. Drake, R. Paudel, and D. S. Jin, “Measurement of the homogeneous contact of a unitary Fermi gas,” *Physical Review Letters* **109**(22), 220402 (2012).
- [74] J. E. Thomas, J. Kinast, and A. Turlapov, “Virial theorem and universality in a unitary Fermi gas,” *Physical Review Letters* **95**(12), 120402 (2005).

- [75] J. T. Stewart, J. P. Gaebler, C. A. Regal, and D. S. Jin, “Potential energy of a  $^{40}\text{K}$  Fermi gas in the BCS-BEC crossover,” *Physical Review Letters* **97**(22), 220406 (2006).
- [76] L. Luo, B. Clancy, J. Joseph, J. Kinast, and J. E. Thomas, “Measurement of the entropy and critical temperature of a strongly interacting Fermi gas,” *Physical Review Letters* **98**(8), 080402 (2007).
- [77] T.-L. Ho and E. J. Mueller, “High temperature expansion applied to fermions near Feshbach resonance,” *Physical Review Letters* **92**(16), 160404 (2004).
- [78] X.-J. Liu, H. Hu, and P. D. Drummond, “Virial expansion for a strongly correlated Fermi gas,” *Physical Review Letters* **102**(16), 160401 (2009).
- [79] V. Ngampruetikorn, M. M. Parish, and J. Levinsen, “High-temperature limit of the resonant Fermi gas,” *Physical Review A* **91**(1), 013606 (2015).
- [80] M. J. H. Ku, A. T. Sommer, L. W. Cheuk, and M. W. Zwierlein, “Revealing the superfluid lambda transition in the universal thermodynamics of a unitary Fermi gas,” *Science* **335**(6068), 563–567 (2012).
- [81] Y. Shin, M. W. Zwierlein, C. H. Schunck, A. Schirotzek, and W. Ketterle, “Observation of phase separation in a strongly interacting imbalanced Fermi gas,” *Physical Review Letters* **97**(3), 030401 (2006).
- [82] T. L. Ho and Q. Zhou, “Obtaining the phase diagram and thermodynamic quantities of bulk systems from the densities of trapped gases,” *Nature Physics* **6**(2), 131–134 (2010).
- [83] S. Nascimbene, N. Navon, K. J. Jiang, F. Chevy, and C. Salomon, “Exploring the thermodynamics of a universal Fermi gas,” *Nature* **463**(7284), 1057–1060 (2010).
- [84] K. Van Houcke, F. Werner, E. Kozik, N. Prokof’ev, B. Svistunov, M. J. H. Ku, A. T. Sommer, L. W. Cheuk, A. Schirotzek, and M. W. Zwierlein, “Feynman diagrams versus Fermi-gas Feynman emulator,” *Nature Physics* **8**(5), 366–370 (2012).

- [85] M. Bartenstein, A. Altmeyer, S. Riedl, S. Jochim, C. Chin, J. H. Denschlag, and R. Grimm, “Collective excitations of a degenerate gas at the BEC-BCS crossover,” *Physical Review Letters* **92**(20), 203201 (2004).
- [86] M. W. Zwierlein, C. A. Stan, C. H. Schunck, S. M. F. Raupach, A. J. Kerman, and W. Ketterle, “Condensation of pairs of fermionic atoms near a Feshbach resonance,” *Physical Review Letters* **92**(12), 120403 (2004).
- [87] T. Bourdel, L. Khaykovich, J. Cubizolles, J. Zhang, F. Chevy, M. Teichmann, L. Tarruell, S. J. J. M. F. Kokkelmans, and C. Salomon, “Experimental study of the BEC-BCS crossover region in  $^6\text{Li}$ ,” *Physical Review Letters* **93**(5), 050401 (2004).
- [88] M. G. Ries, A. N. Wenz, G. Zürn, L. Bayha, I. Boettcher, D. Kedar, P. A. Murthy, M. Neidig, T. Lompe, and S. Jochim, “Observation of pair condensation in the quasi-2D BEC-BCS crossover,” *Physical Review Letters* **114**(23), 230401 (2015).
- [89] S. Matyjaśkiewicz, M. H. Szymańska, and K. Góral, “Probing fermionic condensates by fast-sweep projection onto Feshbach molecules,” *Physical Review Letters* **101**(15), 150410 (2008).
- [90] W. Ketterle and M. W. Zwierlein, “Making, probing and understanding ultracold Fermi gases,” in *Proceedings-International school of physics Enrico Fermi*, **164**, 95, IOS Press; Ohmsha; 1999 (2007).
- [91] E. Braaten and H. W. Hammer, “Universality in few-body systems with large scattering length,” *Physics Reports-Review Section of Physics Letters* **428**(5-6), 259–390 (2006).
- [92] L. Salasnich, “Ideal quantum gases in d-dimensional space and power-law potentials,” *Journal of Mathematical Physics* **41**(12), 8016–8024 (2000).
- [93] C. J. Pethick and H. Smith, *Bose-Einstein condensation in dilute gases*, Cambridge University Press (2002).
- [94] L. Landau and E. Lifshitz, *Quantum mechanics, vol. III*, Butterworth-Heinemann (1997).

## Bibliography

---

- [95] J. J. Sakurai and J. Napolitano, *Modern quantum physics*, Addison-Wesley publishing Inc., ninth edition, Reading (1985).
- [96] J. Dalibard, “Collisional dynamics of ultra-cold atomic gases,” in *Proceedings of the International School of Physics-Enrico Fermi*, **321** (1999).
- [97] J. S. Townsend, *A modern approach to quantum mechanics*, University Science Books (2000).
- [98] S. Giorgini, L. P. Pitaevskii, and S. Stringari, “Theory of ultracold atomic Fermi gases,” *Reviews of Modern Physics* **80**(4), 1215–1274 (2008).
- [99] R. Krems, B. Friedrich, and W. C. Stwalley, *Cold molecules: theory, experiment, applications*, CRC press (2009).
- [100] H. Feshbach, “A unified theory of nuclear reactions,” *Annals of Physics* **5**(4), 357–390 (1958).
- [101] U. Fano, “Effects of configuration interaction on intensities and phase shifts,” *Physical Review* **124**(6), 1866–1878 (1961).
- [102] T. Köhler, K. Góral, and P. S. Julienne, “Production of cold molecules via magnetically tunable Feshbach resonances,” *Reviews of Modern Physics* **78**(4), 1311–1361 (2006).
- [103] M. Inguscio, W. Ketterle, and C. Salomon, *Ultracold Fermi Gases*, vol. 164, IOS Press (2008).
- [104] E. Tiesinga, B. J. Verhaar, and H. T. C. Stoof, “Threshold and resonance phenomena in ultracold ground-state collisions,” *Physical Review A* **47**(5), 4114–4122 (1993).
- [105] M. Bartenstein, A. Altmeyer, S. Riedl, S. Jochim, C. Chin, J. H. Denschlag, and R. Grimm, “Crossover from a molecular Bose-Einstein condensate to a degenerate Fermi gas,” *Physical Review Letters* **92**(12), 120401 (2004).

- [106] J. Kinast, S. L. Hemmer, M. E. Gehm, A. Turlapov, and J. E. Thomas, “Evidence for superfluidity in a resonantly interacting Fermi gas,” *Physical Review Letters* **92**(15), 150402 (2004).
- [107] G. Zürn, T. Lompe, A. N. Wenz, S. Jochim, P. S. Julienne, and J. M. Hutson, “Precise characterization of  $^6\text{Li}$  Feshbach resonances using trap-sideband-resolved RF spectroscopy of weakly bound molecules,” *Physical Review Letters* **110**(13), 135301 (2013).
- [108] A. J. Moerdijk, B. J. Verhaar, and A. Axelsson, “Resonances in ultracold collisions of  $^6\text{Li}$ ,  $^7\text{Li}$ , and  $^{23}\text{Na}$ ,” *Physical Review A* **51**(6), 4852–4861 (1995).
- [109] P. O. Fedichev, M. W. Reynolds, and G. V. Shlyapnikov, “Three-body recombination of ultracold atoms to a weakly bound  $s$  level,” *Physical Review Letters* **77**(14), 2921–2924 (1996).
- [110] I. Bloch, J. Dalibard, and W. Zwerger, “Many-body physics with ultracold gases,” *Reviews of Modern Physics* **80**(3), 885–964 (2008).
- [111] W. Zwerger, *The BCS-BEC crossover and the unitary Fermi gas*, vol. 836, Springer Science and Business Media (2011).
- [112] C. A. R. Sá de Melo, M. Randeria, and J. R. Engelbrecht, “Crossover from BCS to Bose superconductivity: Transition temperature and time-dependent Ginzburg-Landau theory,” *Physical Review Letters* **71**(19), 3202–3205 (1993).
- [113] A. Leggett, *Modern trends in the theory of condensed matter*, Springer-Verlag Berlin (1980).
- [114] A. Schirotzek, Y.-i. Shin, C. H. Schunck, and W. Ketterle, “Determination of the superfluid gap in atomic Fermi gases by quasiparticle spectroscopy,” *Physical Review Letters* **101**(14), 140403 (2008).
- [115] P. Makotyn, C. E. Klauss, D. L. Goldberger, E. A. Cornell, and D. S. Jin, “Universal dynamics of a degenerate unitary Bose gas,” *Nat Phys* **10**(2), 116–119 (2014).

- [116] M. Randeria and E. Taylor, “Crossover from Bardeen-Cooper-Schrieffer to Bose-Einstein condensation and the unitary Fermi gas,” *Annual Review of Condensed Matter Physics* **5**(1), 209–232 (2014).
- [117] J. Steinhauer, R. Ozeri, N. Katz, and N. Davidson, “Excitation spectrum of a Bose-Einstein condensate,” *Physical Review Letters* **88**(12), 120407 (2002).
- [118] R. Combescot, M. Y. Kagan, and S. Stringari, “Collective mode of homogeneous superfluid Fermi gases in the BEC-BCS crossover,” *Physical Review A* **74**(4), 042717 (2006).
- [119] J. Fuchs, *Molecular Bose-Einstein condensates and p-wave Feshbach molecules of  ${}^6\text{Li}_2$* , PhD thesis, Swinburne University of Technology (2009).
- [120] G. Veeravalli, *Bragg spectroscopy of a strongly interacting Fermi gas*, PhD thesis, Swinburne University of Technology (2009).
- [121] P. Dyke, *Quasi two-dimensional  ${}^6\text{Li}$  Fermi gas*, PhD thesis, Swinburne University of Technology (2010).
- [122] E. Kuhnle, *Studies of universality in strongly interacting  ${}^6\text{Li}$  Fermi gases with Bragg spectroscopy*, PhD thesis, Swinburne University of Technology (2011).
- [123] S. Hoinka, *Precision Bragg spectroscopy of the density and spin response of a strongly interacting Fermi gas*, PhD thesis, Swinburne University of Technology (2014).
- [124] M. E. Gehm, *Properties of  ${}^6\text{Li}$* , Jetlab, Jetlab (2003).
- [125] N. F. Ramsey, *Molecular beams*, Clarendon (1969).
- [126] R. Grimm, M. Weidemüller, and Y. B. Ovchinnikov, “Optical dipole traps for neutral atoms,” *Advances in atomic, molecular, and optical physics* **42**, 95–170 (2000).
- [127] G. Reinaudi, T. Lahaye, Z. Wang, and D. Guery-Odelin, “Strong saturation absorption imaging of dense clouds of ultracold atoms,” *Optics Letters* **32**(21), 3143–3145 (2007).

- [128] J. M. Kinast, *Thermodynamics and superfluidity of a strongly interacting Fermi gas*, PhD thesis, Duke University (2006).
- [129] X.-J. Liu, H. Hu, and P. D. Drummond, “Exact few-body results for strongly correlated quantum gases in two dimensions,” *Physical Review B* **82**(5), 054524 (2010).
- [130] K. Fenech, P. Dyke, T. Peppler, M. G. Lingham, S. Hoinka, H. Hu, and C. J. Vale, “Universal thermodynamics of an attractive 2D Fermi gas,” (2015).
- [131] R. Haussmann, “Properties of a Fermi liquid at the superfluid transition in the crossover region between BCS superconductivity and Bose-Einstein condensation,” *Physical Review B* **49**(18), 12975–12983 (1994).
- [132] R. Haussmann, W. Rantner, S. Cerrito, and W. Zwerger, “Thermodynamics of the BCS-BEC crossover,” *Physical Review A* **75**(2), 023610 (2007).
- [133] A. Bulgac, J. E. Drut, and P. Magierski, “Spin 1/2 fermions in the unitary regime: A superfluid of a new type,” *Physical Review Letters* **96**(9), 090404 (2006).
- [134] O. Goulko and M. Wingate, “Thermodynamics of balanced and slightly spin-imbalanced Fermi gases at unitarity,” *Physical Review A* **82**(5), 053621 (2010).
- [135] M. Horikoshi, S. Nakajima, M. Ueda, and T. Mukaiyama, “Measurement of universal thermodynamic functions for a unitary Fermi gas,” *Science* **327**(5964), 442–445 (2010).
- [136] P. J. Martin, B. G. Oldaker, A. H. Miklich, and D. E. Pritchard, “Bragg scattering of atoms from a standing light-wave,” *Physical Review Letters* **60**(6), 515–518 (1988).
- [137] M. Kozuma, L. Deng, E. W. Hagley, J. Wen, R. Lutwak, K. Helmerson, S. L. Rolston, and W. D. Phillips, “Coherent splitting of Bose-Einstein condensed atoms with optically induced Bragg diffraction,” *Physical Review Letters* **82**(5), 871–875 (1999).
- [138] P. Nozières and D. Pines, *Theory of quantum liquids*, Westview Press (1999).

- [139] F. Schwabl, *Advanced quantum mechanics*, Springer Science and Business Media (2005).
- [140] A. Brunello, F. Dalfovo, L. Pitaevskii, S. Stringari, and F. Zambelli, “Momentum transferred to a trapped Bose-Einstein condensate by stimulated light scattering,” *Physical Review A* **64**(6), 063614 (2001).
- [141] P. B. Blakie, R. J. Ballagh, and C. W. Gardiner, “Theory of coherent Bragg spectroscopy of a trapped Bose-Einstein condensate,” *Physical Review A* **65**(3), 033602 (2002).
- [142] P. Törmä, *Spectroscopies — Theory*, 199–250, IMPERIAL COLLEGE PRESS (2014).
- [143] H. A. Kramers, *La diffusion de la lumiere par les atomes*, vol. 2, Atti Congr. Fisica Como (1927).
- [144] R. de Kronig, “On the theory of dispersion of X-rays,” *JOSA* **12**(6), 547–556 (1926).
- [145] S. Sachdev, *Quantum Phase Transitions*, Cambridge University Press (2011).
- [146] P. W. Anderson, “Random-phase approximation in the theory of superconductivity,” *Physical Review* **112**(6), 1900–1916 (1958).
- [147] A. Minguzzi, G. Ferrari, and Y. Castin, “Dynamic structure factor of a superfluid Fermi gas,” *The European Physical Journal D-Atomic, Molecular, Optical and Plasma Physics* **17**(1), 49–55 (2001).
- [148] Y. Ohashi and A. Griffin, “Superfluid transition temperature in a trapped gas of Fermi atoms with a Feshbach resonance,” *Physical Review A* **67**(3), 033603 (2003).
- [149] Y. Ohashi and A. Griffin, “Single-particle excitations in a trapped gas of Fermi atoms in the BCS-BEC crossover region.,” *Physical Review A* **72**(6), 013601 (2005).

## Bibliography

---

- [150] Y. Ohashi and A. Griffin, “Single-particle excitations in a trapped gas of Fermi atoms in the BCS-BEC crossover region. II. Broad Feshbach resonance,” *Physical Review A* **72**(6), 063606 (2005).
- [151] F. Zambelli, L. Pitaevskii, D. M. Stamper-Kurn, and S. Stringari, “Dynamic structure factor and momentum distribution of a trapped Bose gas,” *Physical Review A* **61**(6), 063608 (2000).
- [152] S. Hoinka, M. Lingham, M. Delehay, and C. J. Vale, “Dynamic spin response of a strongly interacting Fermi gas,” *Physical Review Letters* **109**(5), 050403 (2012).
- [153] H. Hu and X.-J. Liu, “Universal dynamic structure factor of a strongly correlated Fermi gas,” *Physical Review A* **85**(2), 023612 (2012).

# List of publications

P. Dyke, E. D. Kuhnle, S. Whitlock, H. Hu, M. Mark, S. Hoinka, M. Lingham, P. Hannaford, and C. J. Vale, “Crossover from 2D to 3D in a weakly interacting Fermi gas,” *Physical Review Letters* **106**, 105304 (2011).

Received 5 November 2010; published 11 March 2011.

S. Hoinka, M. Lingham, M. Delehay, and C. J. Vale, “Dynamic spin response of a strongly interacting Fermi gas,” *Physical Review Letters* **109**, 050403 (2012).

Received 15 March 2012; published 1 August 2012.

S. Hoinka, M. Lingham, K. Fenech, H. Hu, C. J. Vale, J. E. Drut, and S. Gandolfi, “Precise determination of the structure factor and contact in a unitary Fermi gas,” *Physical Review Letters* **110**, 055305 (2013)

Received 13 September 2012; published 30 January 2013.

M. G. Lingham, K. Fenech, S. Hoinka, and C. J. Vale, “Local observation of pair condensation in a Fermi gas at unitarity,” *Physical Review Letters* **112**, 100404 (2014).

Received 18 November 2013; published 13 March 2014.

# Appendix - Copyright Statements

I warrant that I have obtained, where necessary, permission from the copyright owners to use any third party copyright material reproduced in the thesis (such as artwork, images, unpublished documents), or to use any of my own published work (such as journal articles) in which the copyright is held by another party (such as publisher, co-author).

Figure 2.5: Reprinted figures with permission from R. Combescot, M. Y. Kagan, and S. Stringari, “Collective mode of homogeneous superfluid Fermi gases in the BEC-BCS crossover,” *Physical Review A* **74** 042717 (2006). Copyright 2015 by the American Physical Society

Figure 3.12: Reprinted by permission from Macmillan Publishers Ltd: Nature Physics, advanced online publication, (28 09 2015).

Figure 4.5: Reprinted figures with permission from S. Hoinka, M. Lingham, K. Fenech, H. Hu, C. J. Vale, J. E. Drut, and S. Gandolfi, “Precise determination of the structure factor and contact in a unitary Fermi gas,” *Physical Review Letters* **110** 055305 (2013). Copyright 2015 by the American Physical Society

Figure 6.4(b): Reprinted figures with permission from Y. Sagi, T. E. Drake, R. Paudel, and D. S. Jin, “Measurement of the homogeneous contact of a unitary Fermi gas,” *Physical Review Letters* **109** 220402 (2012). Copyright 2015 by the American Physical Society